

## ABSTRACT

PUROHIT, YOJNA. Atomistic and First Principles Studies of Pb Segregation to Al Grain Boundaries and its Influence on Thermal Stability and Mechanical Behavior. (Under the direction of Prof. Donald W. Brenner).

Nanostructured materials have received much interest because they exhibit different properties compared to coarse-grained polycrystals of the same material. Many enhancements in the properties of nanocrystalline materials due to fine grain size are lost if grain growth occurs. Enrichment of the grain boundaries (segregation) with solute atoms with limited solubilities has been shown to diminish or even reverse the free energy available for grain growth by forming metastable structures. Al-Pb is an immiscible alloy system with a positive energy of segregation and therefore is a potential candidate for segregation-induced grain boundary stabilization.

To investigate the segregation-induced stability of grain boundaries in Al-Pb nanoalloys, atomic modeling was used to characterize the structure and energy of substitutional Pb defects in bulk Al, and in an Al bi- and nano-crystal. Monte Carlo simulations using a modified embedded atom method (MEAM) potential fit to first principles results predict the formation of Pb clusters in bulk Al, in agreement with prior experiments. In the case of the bicrystal and nanocrystalline structure, the simulations predict segregation of Pb impurities towards Al grain boundaries prior to cluster formation depending on the Pb content and the number of grain boundaries. Analysis of the relative enthalpies for Pb defects suggests that

Pb impurities can help stabilize nanocrystalline Al against grain growth. Subsequent calculations of the energies of Pb clusters embedded in an Al matrix, in a cuboctahedral configuration, using the same potential, predict a cross-over cluster size of approximately 2.8 nm below which Pb prefers to segregate to grain boundaries compared to forming clusters in the Al matrix.

To study the stabilization of Al grain boundaries caused by segregation of Pb impurities, grain boundary energy as a function of Pb content was investigated for two high symmetry  $\Sigma 5 \{210\}$  and  $\Sigma 5 \{310\}$  Al tilt grain boundaries. Calculations for grain boundary energies were performed using atomistic MEAM and Density Functional Theory calculations. Results from both of these methods showed a reduction in grain boundary energy with an increase in Pb content.

To further explore the boundary stabilization caused by segregated Pb atoms over the entire tilt angle, a dependence of the energies of  $\langle 100 \rangle$  symmetrical Al tilt boundaries, with and without Pb substitution, on misorientation angles was investigated using a multiscale disclination-structural unit model (DSUM). The DSUM combines an atomistic structural unit model with a mesoscopic disclination based description of grain boundaries. The agreement between grain boundary energy calculations using the multiscale DSUM and the atomistic calculations is reasonably good, with our MEAM+DSUM (model combining MEAM with DSUM) results agreeing with the atomistic MEAM calculation, and our GLUE+DSUM (model combining GLUE interatomic potential with DSUM) results agreeing with the

atomistic GLUE calculation at intermediate angles within about  $0.08 \text{ J/m}^2$  and  $0.06 \text{ J/m}^2$ , respectively. The predictions given by the MEAM+DSUM and the GLUE+DSUM for an intermediate grain boundary containing Pb at  $22.6^\circ$ , along with matching the full atomistic MEAM and GLUE result also matched the first principles result reasonably well. The multiscale DSUM predicts a strong dependence of the grain stabilization energy on tilt angle.

Although there exist several experimental/theoretical studies on the mechanical behavior of single component nano-crystalline materials, studies on the effect of a second component on the mechanical behavior of nanocrystalline materials are very limited. In this dissertation the effect of Pb on the mechanical behavior of pure Al using molecular dynamics (MD) simulations was investigated. MD simulations were carried out for uniaxial tensile straining of bicrystalline aluminum (Al) and aluminum-lead (Al-Pb) alloys. A softening owing to the presence of Pb on the Al grain boundaries, in agreement with, but less than that found experimentally, was observed. The thickening and disordering of the grain boundaries was believed to be contributing to this softening.

Atomistic and First Principles Studies of Pb Segregation to Al Grain  
Boundaries and its Influence on Thermal Stability  
and Mechanical Behavior

by  
Yojna Purohit

A dissertation submitted to the Graduate Faculty of  
North Carolina State University  
in partial fulfillment of the  
requirements for the Degree of  
Doctor of Philosophy

Materials Science and Engineering

Raleigh, North Carolina

2008

APPROVED BY:

-----  
Prof. Ronald O. Scattergood

-----  
Prof. Carl C. Koch

-----  
Prof. John M. Mackenzie  
(Minor Representative)

-----  
Prof. Donald W. Brenner  
(Chair of Advisory Committee)

## **DEDICATION**

*To My Husband Nish.*

## **BIOGRAPHY**

Yojna Purohit was born on October 28<sup>th</sup> 1975 in the northern state of Uttar Pradesh, India. She received her Bachelor of Engineering in Metallurgical Engineering from Raipur Engineering College, Raipur, India, in June 1998. Later she enrolled at the Indian Institute of Technology (IIT), Kanpur, India for her Master of Technology in Materials and Metallurgical Engineering in July 1998. For her master's thesis, she worked on "A Preliminary Investigation on the Correlation of Microstructural Parameters with Texture in Ni-10% Co Alloy" in the research group supervised by Prof. Sandeep Sangal. She finished her master's degree in May 2000. Following this, She got job in Syntel Software's, Mumbai, India, but decided to work as a research assistant in IIT-Kanpur. She then joined the research group supervised by Prof. Donald W. Brenner at North Carolina State University in August 2003 for her doctoral studies.

## **ACKNOWLEDGEMENTS**

I would like to express my sincere gratefulness to my advisor Prof. Donald W. Brenner for his guidance, encouragement, suggestion and discussion. I am also thankful to Prof. Ronald O. Scattergood for his support and guidance to this research.

I would also like to thank Prof. Carl C. Koch and Prof. John M. Mackenzie for agreeing to serve on my PhD thesis committee.

I would like to acknowledge National Science Foundation for financial support. In addition, I would like to acknowledge my coworkers, D. L. Irving, Lipeng Sun and C. W. Padgett, for their help. I am also thankful to Ms. Edna Deas for her help in administrative matters.

Finally, I would like to thank my husband, parents and other family members for their support and encouragement.

# TABLE OF CONTENTS

<b>LIST OF TABLES .....</b>	<b>x</b>
<b>LIST OF FIGURES .....</b>	<b>xiv</b>
<b>CHAPTER 1 – INTRODUCTION .....</b>	<b>1</b>
1.1 INTRODUCTION .....	1
1.1.1 PROPERTIES OF NANOSTRUCTURED MATERIALS .....	7
1.1.1.1 STRENGTH AND HARDNESS .....	7
1.1.1.2 DUCTILITY .....	9
1.1.1.3 ELASTIC PROPERTIES.....	10
1.1.1.4 DIFFUSIVITY .....	11
1.1.1.5 THERMAL STABILITY OF NANOSTRUCTURED MATERIALS.....	12
1.1.2 COMPUTER MODELING .....	13
1.1.3 NANOALLOYS .....	15
1.1.3.1 Al-Pb ALLOY SYSTEM.....	18
1.2 THESIS OBJECTIVES .....	23
1.3 THESIS ORGANIZATION.....	23
REFERENCES .....	25
<b>CHAPTER 2 – FUNDAMENTALS OF ATOMISTIC SIMULATIONS.....</b>	<b>31</b>

2.1 INTRODUCTION .....	31
2.2 ATOMISTIC SIMULATIONS.....	31
2.2.1 THERMODYNAMIC ENSEMBLES .....	32
2.3 METROPOLIS MONTE CARLO ALGORITHM.....	34
2.4 MOLECULAR DYNAMICS .....	39
2.4.1 INTEGRATORS.....	41
2.4.1.1 VELOCITY VERLET ALGORITHM .....	41
2.4.1.2 PREDICTOR-CORRECTOR ALGORITHM .....	42
2.5 THERMOSTATS .....	45
2.5.1 HOOVER THERMOSTAT .....	46
2.6 PERIODIC BOUNDARY CONDITIONS .....	47
REFERENCES .....	49
<b>CHAPTER 3 – INTERATOMIC POTENTIAL FOR Al-Pb ALLOY .....</b>	<b>52</b>
3.1 INTRODUCTION .....	52
3.2 MEAM FORMALISM .....	54
3.2.1 SCREENING PROCEDURE .....	59
3.3 Al-Pb ALLOY MEAM POTENTIAL .....	61
3.4 DFT CALCULATIONS .....	65
REFERENCES .....	67

**CHAPTER 4 – MODELING OF THE STRUCTURES FORMED BY  
SUBSTITUTIONAL Pb IMPURITY IN Al AND ITS EFFECT ON MECHANICAL  
BEHAVIOR.....70**

4.1 INTRODUCTION ..... 70

4.2 METHODOLOGY ..... 71

4.3 RESULTS AND DISCUSSIONS..... 74

4.3.1 BULK Al-Pb ALLOY..... 74

4.3.2 BICRYSTALLINE Al-Pb ALLOY ..... 76

4.3.3 NANOCRYSTALLINE Al-Pb ALLOY..... 80

4.4 STABILIZATION ENERGIES ..... 81

4.5 EFFECT OF Pb ON MECHANICAL BEHAVIOR OF Al..... 84

4.5.1 INTRODUCTION ..... 84

4.5.2 METHODOLOGY ..... 85

4.5.3 RESULTS AND DISCUSSION ..... 86

REFERENCES ..... 91

**CHAPTER 5 – PREDICTION OF ENERGIES OF TWO HIGH SYMMETRY  $\Sigma$  5  
<100> TILT GRAIN BOUNDARIES IN Al-Pb ALLOYS USING ATOMISTIC  
MEAM AND FIRST PRINCIPLES DENSITY FUNCTIONAL CALCULATIONS93**

5.1 INTRODUCTION ..... 93

5.2 METHODOLOGY ..... 96

5.3 MEAM RESULTS..... 99

5.4 FIRST PRINCIPLES RESULTS .....	101
REFERENCES .....	105

**CHAPTER 6 – PREDICTION OF A MINIMUM Pb CLUSTER SIZE BELOW WHICH Pb PREFERS TO SEGREGATE TO Al GRAIN BOUNDARIES**

<b>COMPARED TO FORMING CLUSTERS IN BULK Al.....</b>	<b>106</b>
6.1 INTRODUCTION .....	106
6.2 METHODOLOGY .....	108
6.3 RESULTS AND DISCUSSION.....	115
REFERENCES .....	121

**CHAPTER 7 – PREDICTION OF ENERGIES OF <100> TILT GRAIN BOUNDARIES IN Al-Pb ALLOYS USING THE DISCLINATION STRUCTURAL UNITS MODEL .....**

<b>.....</b>	<b>122</b>
7.1 INTRODUCTION .....	122
7.2 METHODOLOGY .....	124
7.3 RESULTS AND DISCUSSION.....	129
REFERENCES .....	134

**CHAPTER 8 – SUMMARY AND SUGGESTIONS FOR THE FUTURE WORK**

<b>136</b>	<b>136</b>
8.1 SUMMARY .....	136
8.2 SUGGESTIONS FOR THE FUTURE WORK.....	141

REFERENCES .....142

## LIST OF TABLES

### CHAPTER 2 - FUNDAMENTALS OF ATOMISTIC SIMULATIONS

Table 2.1 Coefficient values for a second order Nordsieck-Gear predictor-corrector  
Method .....45

### CHAPTER 3 - INTERATOMIC POTENTIAL FOR Al-Pb ALLOY

Table 3.1 Parameters for the MEAM potential of Al and Pb. The units of the sublimation energy  $E_c$ , and the equilibrium nearest-neighbor distance  $r_e$ , are the eV and  $\text{\AA}^0$  respectively .....61

Table 3.2 Parameters for the MEAM potential for the Al-Pb alloy. The units of the sublimation energy  $E_c$ , and the equilibrium nearest-neighbor distance  $r_e$ , are the eV and  $\text{\AA}^0$  respectively .....63

Table 3.3 Angular screening parameters for the Al-Pb alloy MEAM potential.  $C_{\max}$  values are 2.80 for all the combinations.....64

Table 3.4 Comparison of the properties of two hypothetical Al-Pb alloys given by first principles DFT calculations and the MEAM potential .....67

**CHAPTER 4 - MODELING OF THE STRUCTURES FORMED BY  
SUBSTITUTIONAL Pb IMPURITY IN Al AND ITS EFFECT ON MECHANICAL  
BEHAVIOR**

Table 4.1 Atomic segregation energies and hydrostatic stresses for atoms around the  $\Sigma 5$  {210} Al grain boundary. The segregation energies and hydrostatic stresses are in units of eV/atom and GPa, respectively. -ve Tensile stress, +ve Compressive stress .....78

Table 4.2 Enthalpies of several Al-Pb structures .....83

Table 4.3 Relative enthalpies of several bicrystalline Al-Pb structures. Relative enthalpy of 1 Pb in bulk Al = 1.622 eV/atom .....84

**CHAPTER 5 - PREDICTION OF ENERGIES OF TWO HIGH SYMMETRY  $\Sigma 5$   
<100> TILT GRAIN BOUNDARIES IN Al-Pb ALLOYS USING ATOMISTIC MEAM  
AND FIRST PRINCIPLES DENSITY FUNCTIONAL CALCULATIONS**

Table 5.1 Calculated grain boundary energies in J/m<sup>2</sup>. The EAM energies are taken from ref. [21] and the experimental energies are from ref. [22] .....105

**CHAPTER 6 - PREDICTION OF A MINIMUM Pb CLUSTER SIZE BELOW WHICH Pb PREFERS TO SEGREGATE TO Al GRAIN BOUNDARIES COMPARED TO FORMING CLUSTERS IN BULK Al**

Table 6.1 Details showing calculations of energy term  $E_2$  (In Eq. (4) above).....116

Table 6.2 Details showing calculations of energy term  $E_1$  (In Eq. (4) above). MN refers to magic numbers of Pb atoms.....117

Table 6.3 Details showing calculations of energy term  $\Delta E$  (In Eq. (4) above). MN refers to magic numbers of Pb atoms.....118

**CHAPTER 7 - PREDICTION OF ENERGIES OF <100> TILT GRAIN BOUNDARIES IN Al-Pb ALLOYS USING DISCLINATION STRUCTURAL UNITS MODEL**

Table 7.1 Geometric parameters of the preferred boundaries and the elastic constants used in the calculations .....127

Table 7.2 List of intermediate interfaces studied for <100> tilt Al boundaries [17].....129

Table 7.3 Calculated energies ( $\text{J/m}^2$ ) for an intermediate grain boundary in the Al and Al-Pb system. The experimental energies are from ref. [18].....133

## LIST OF FIGURES

### CHAPTER 1 - INTRODUCTION

Fig. 1.1 Two-dimensional model of a nanostructured material. The atoms in the centers of the crystals are indicated in black. The ones in the boundary core regions are represented as open circles [1] .....6

Fig. 1.2 Schematic representation of the variation of yield stress as a function of grain size from nanocrystalline to microcrystalline regimes [19].....8

Fig. 1.3 Young's modulus as a function of porosity for nanocrystalline Pd and Cu [32] .11

Fig. 1.4 Z-contrast image of in situ consolidated Al-1.0%Pb showing the Al grain boundaries covered with Pb atoms. The brighter region represents Pb phase and darker region represents Al phase [60] .....20

### CHAPTER 2 - FUNDAMENTALS OF ATOMISTIC SIMULATIONS

Fig. 2.1 Schematic of Metropolis Monte Carlo Algorithm.....38

Fig. 2.2 A general flow chart for molecular dynamics simulation .....40

Fig. 2.3 Illustration of periodic boundary conditions .....49

**CHAPTER 3 - INTERATOMIC POTENTIAL FOR Al-Pb ALLOY**

Fig. 3.1 Potential screening of atoms i and k by atom j [13] .....60

**CHAPTER 4 - MODELING OF THE STRUCTURES FORMED BY  
SUBSTITUTIONAL Pb IMPURITY IN Al AND ITS EFFECT ON MECHANICAL  
BEHAVIOR**

Fig. 4.1 Illustration of the Al bicrystalline geometry. (a) Entire Al bicrystal containing two complementary  $\Sigma 5 \langle 100 \rangle \{210\}$  tilt grain boundaries. Bulk atoms are shown in blue and other colors represent GB atoms. (b) A Schematic of the  $\Sigma 5 \langle 100 \rangle \{210\}$  tilt grain boundary. The open and closed circles represent atoms on the  $\{100\}$  and  $\{200\}$  planes, respectively .....72

Fig. 4.2 (a) Johnson-Mehl nucleation and grain growth process. (b) A polycrystalline nanostructure with an average grain size of 5 nm. Atoms are colored by centrosymmetry parameter [15]. Blue represents bulk fcc atoms and other colors represent grain boundary atoms .....73

Fig. 4.3 Illustrations of the initial and simulated configurations for the bulk Al-Pb solid solution. Al and Pb atoms are shown in blue and red, respectively. (a) Initial configuration. (b) Final configuration after  $1.9 \times 10^6$  MC moves .....75

Fig. 4.4 Size distribution for Pb nanoclusters in bulk Al-Pb solid solution.....76

Fig. 4.5 Initial configuration for an Al bicrystal, where one percent of the Al atoms are replaced with Pb atoms .....77

Fig. 4.6 Illustration of the final configuration after  $2 \times 10^6$  MC moves for the system with 1 atomic percent Pb impurities. Al and Pb atoms are shown in blue and red, respectively. (a) Entire system. (b) Close-up view .....77

Fig. 4.7 Illustration of the final configuration after  $5.5 \times 10^6$  MC moves for the system with 5 atomic percent Pb impurities. Al and Pb atoms are shown in blue and red, respectively. (a) Entire system. (b) Close-up view .....79

Fig. 4.8 Illustrations of the final configuration (after  $2 \times 10^6$  MC moves) for the nanocrystalline Al-Pb alloy. Al is shown in blue, and Pb and grain boundary atoms are shown in red and green, respectively .....80

Fig. 4.9 Pb cluster distribution in nanocrystalline Al-Pb alloy.....81

Fig. 4.10 Stress-strain curves for pure Al and Al-Pb alloys with 1 and 8 atomic percent Pb on Al grain boundaries.....87

Fig. 4.11 Deformation structures for pure Al at 60, 61 and 62 ps .....88

Fig. 4.12 Deformation structures for 1 atomic percent Pb doped Al at 56, 57, 58 and 59 ps.....89

Fig. 4.13 Deformation structures for 8 atomic percent Pb doped Al at 58, 59, 60 and 61 ps.....90

**CHAPTER 5 - PREDICTION OF ENERGIES OF TWO HIGH SYMMETRY  $\Sigma 5$   $\langle 100 \rangle$  TILT GRAIN BOUNDARIES IN Al-Pb ALLOYS USING ATOMISTIC MEAM AND FIRST PRINCIPLES DENSITY FUNCTIONAL CALCULATIONS**

Fig. 5.1 (a) Illustration of an Al bicrystalline geometry containing two  $\Sigma 5 \langle 100 \rangle \{210\}$  tilt grain boundaries. Bulk and GB atoms are shown in silver and white, respectively. (b) Schematic of the  $\Sigma 5 \langle 100 \rangle \{210\}$  tilt grain boundaries. The open and closed circles represent atoms on the  $\{100\}$  and  $\{200\}$  planes, respectively .....98

Fig. 5.2 (a) Illustration of an Al bicrystalline geometry containing two  $\Sigma 5 \langle 100 \rangle \{310\}$

tilt grain boundaries. Bulk and GB atoms are shown in silver and white, respectively. (b) Schematic of the  $\Sigma 5 \langle 100 \rangle \{310\}$  tilt grain boundaries. The open and closed circles represent atoms on the  $\{100\}$  and  $\{200\}$  planes, respectively .....99

Fig. 5. 3 Grain boundary energy as a function of the percentage of the coincident sites occupied by Pb atoms - ( $\Sigma 5 \{210\}$  grain boundary).....100

Fig. 5.4 Grain boundary energy as a function of the percentage of the coincident sites occupied by Pb atoms - ( $\Sigma 5 \{310\}$  grain boundary).....100

Fig. 5.5 Illustrations of the  $\Sigma 5 \{210\}$  structure (top views) and the  $\Sigma 5 \{310\}$  structure (bottom views) without (left views) and with Pb (right views). Al (Grey), Pb (Black)..104

**CHAPTER 6 - PREDICTION OF A MINIMUM Pb CLUSTER SIZE BELOW WHICH Pb PREFERS TO SEGREGATE TO Al GRAIN BOUNDARIES COMPARED TO FORMING CLUSTERS IN BULK Al**

Fig. 6.1 (a) A simulation cell, showing a cuboctahedral shaped Pb cluster (red) embedded in Al matrix (blue). (b) Schematic of cuboctahedral shape viewed along a  $\langle 110 \rangle$  type direction .....109

Fig. 6.2 Illustration of thermodynamic energy model .....110

Fig. 6.3 Schematic of a  $\Sigma 5 \langle 100 \rangle \{210\}$  undoped Al tilt boundary. The silver and black represent atoms on the  $\{100\}$  and  $\{200\}$  planes, respectively .....113

Fig. 6.4 (a) Bicrystalline reference configuration number 1, that contains two Pb doped  $\Sigma 5 \langle 100 \rangle \{210\}$  Al tilt boundaries. (b) Schematic of reference configuration number 1. Al and Pb atoms are shown in silver and black respectively .....113

Fig. 6.5 (a) Bicrystalline reference configuration number 2, that contains two Pb doped  $\Sigma 5 \langle 100 \rangle \{210\}$  Al tilt boundaries. (b) Schematic of reference configuration number 2. Al and Pb atoms are shown in silver and black respectively .....114

Fig. 6.6 (a) Bicrystalline reference configuration number 3, that contains two Pb doped  $\Sigma 5 \langle 100 \rangle \{210\}$  Al tilt boundaries. (b) Schematic of reference configuration number 3. Al and Pb atoms are shown in silver and black respectively .....114

Fig. 6.7 Variation of  $E_2$  with  $mPb$  for the three reference structures.....116

Fig. 6.8 Variation of  $E_1$  with  $nPb$  for cuboctahedral shape Pb clusters .....117

Fig. 6.9  $\Delta E$  (eV/Pb atom) vs.  $nPb$  with respect to reference structure number 1 .....119

Fig. 6.10  $\Delta E$  (eV/Pb atom) vs.  $nPb$  with respect to reference structure number 2 .....120

Fig. 6.11  $\Delta E$  (eV/Pb atom) vs.  $nPb$  with respect to reference structure number 3 .....120

**CHAPTER 7 - PREDICTION OF ENERGIES OF <100> TILT GRAIN  
BOUNDARIES IN Al-Pb ALLOYS USING DISCLINATION STRUCTURAL UNITS  
MODEL**

Fig. 7.1 Disclination structural unit model representation of a grain boundary consisting  
of B and C structural units [9].....126

Fig. 7.2 Dependence of grain boundary energy on angle for <100> symmetrical  
tilt-grain boundaries in Pb doped Al as calculated by atomistic MEAM and multiscale  
MEAM+DSUM model .....130

Fig. 7.3 Dependence of grain boundary energy on angle for <100> symmetrical  
tilt-grain boundaries in Pb doped Al as calculated by atomistic GLUE and multiscale  
GLUE+DSUM model .....132

Fig. 7.4 Dependence of grain boundary energy on angle for <100> symmetrical tilt-grain  
boundaries in Pb doped Al as calculated by atomistic MEAM and GLUE potentials ....132

# CHAPTER 1

## INTRODUCTION

### 1.1 INTRODUCTION

Preparing materials with novel structural features and/or properties is the main driving force behind the progress that has been made in the area of Materials Science. In the case of the nanostructured materials, the generation of solids with new atomic structures and properties is attempted by utilizing and manipulating the atomic arrangements involving defects such as grain boundaries, interphase boundaries or dislocations at the nanometer scale. Gleiter and coworkers [1], who synthesized ultrafine-grained materials by the in situ consolidation of nanoscale atomic clusters in 1980s, pioneered the progress that the last decade has seen in the area of nanostructured materials. The ultrasmall size ( $< 100$  nm) of the grains in these nanostructured materials can result in dramatically different properties from conventional grain-size ( $> 1$   $\mu\text{m}$ ) polycrystalline or single crystal materials of the same chemical composition. This is the stimulus for the tremendous appeal of these materials that have been identified as essential structural components for building the next generation of micro and nano-technological devices (MEMS and NEMS). For example nanometals and/or nanocomposites (in the form of miniature sensors and actuators) along with required microelectronics can be employed in fabricating smart systems for sensing and controlling a

variety of functions in automobile, aerospace, marine and civil structures, and food and medical industries.

In coarse-grained metals, plastic deformation results from the nucleation of dislocations from Frank-Read sources and their motion through the crystal. A dislocation is a line lattice defect that was first introduced to explain the discrepancy between the observed and theoretical shear strength of metals. There are two basic types of dislocation movement, glide (or conservative motion) in which the dislocation moves in the surface which contains both its line and Burgers vector, and climb (or non conservative motion) in which the dislocation moves out of the glide surface normal to the Burgers vector. Glide of many dislocations results in slip, which is the most common manifestation of plastic deformation in crystalline solids. It can be understood as sliding or successive displacement of one plane of atoms over another on so-called slip planes.

The ability of a crystalline material to plastically deform largely depends on the ability for a dislocation to move within a material. Therefore, impeding the movement of dislocations results in the strengthening of the materials. There are a number of ways to impede dislocation movement, which include;

- Control of grain size - Grain boundaries provide obstacles to dislocation motion. As the orientation of the crystals on either side of a grain boundary is different and random, a dislocation moving on a common slip plane in one crystal can rarely move on to a similar slip plane in the adjacent crystal. Hence dislocations are stopped by a grain boundary and pile up against it. The smaller the grain size, the more frequent the pile up of dislocations.

Hall [2] and Petch [3] proposed the following equation for the yield stress of a polycrystalline material  $\sigma_y$  as a function of average grain size  $d$

$$\sigma_y = \sigma_i + kd^{\frac{1}{2}} \quad (1)$$

where  $\sigma_i$  is the yield stress for a crystal of the same material where there are no grain boundaries and,  $k$  is a material-dependent constant. According to this relationship, the yield strength is inversely related to the square root of the grain size. Hence decreasing the grain size aids in the development of high strength materials of the same composition.

- Strain hardening - Strain hardening (also called work-hardening) is the process of making a metal harder and stronger through plastic deformation. When a metal is plastically deformed, dislocations move and additional dislocations are generated. The more the dislocations within a material, the more they interact and become pinned or tangled. This

results in a decrease in the mobility of the dislocations and a strengthening of the material.

However these mechanisms can't be extrapolated to the materials with the grain size in nano regime. In nanostructured solids a large fraction of atoms ~up to 50% (as discussed below) are boundary atoms; thus intercrystalline deformation mechanisms based on grain boundary processes are expected to become relevant, as opposed to intracrystalline mechanisms based on dislocation activity. At the smallest grain sizes, dislocation sources such as Frank-Read source inside grains cannot easily exist because of size and image force limitations; only dislocations emitted from a boundary can eventually travel across the grain. From these arguments a change in plasticity mechanism is expected with decreasing grain size from a dislocation-dominated to a boundary-dominated mechanism such as grain boundary sliding.

Nanostructured materials can be conveniently divided in to three categories [4-5]:

- Materials with reduced dimensions in the form of (isolated, substrate-supported or embedded) nanometer-sized particles, thin wires or thin films. This type of microstructure is important, for example, for materials with catalytic applications.
- Materials in which the nanometer-sized microstructure is limited to a thin (nanometer-sized) surface region of a bulk material. Properties such as corrosion resistance, hardness

and wear resistance can be enhanced by creating a nanometer-sized microstructure in thin surface regions.

- Bulk solids with a nanometer-scale microstructure in which the chemical composition, the atomic arrangement and/or the size of the building blocks (e.g. crystallites or atomic/molecular groups) forming the solid vary on a length scale of a few nanometers throughout the bulk.

Two classes of the latter category, one with a homogenous and other with heterogeneous microstructures, may be distinguished. In the first class, the atomic structure and/or the chemical composition varies in space continuously throughout the solid on an atomic scale. Glasses and supersaturated solid solution are examples of this type. In the second class, the materials are assembled of nanometer-sized building blocks, mostly crystallites as illustrated in Fig. 1.1. These building blocks may differ in their atomic structure, their crystallographic orientation and/or their chemical composition. The heterogeneous structures are crucial for many of the properties of these materials. The focus of this dissertation is on this second class of materials.

Unlike coarse-grained materials, nanostructured materials consist of a large volume fraction of defects such as grain boundaries, interphase boundaries, triple junctions, quadruple junctions, and (strained) crystal lattice regions. Fig. 1.1 illustrates the structure of a two dimensional nanocrystalline material where the boundary core regions (open circles) are

characterized by a reduced atomic density and interatomic spacings deviating from those in the perfect lattice [1]. The fraction of these intercrystalline regions increases as the grain size decreases. A nanocrystalline material may be regarded as a composite consisting of crystalline and intercrystalline (grain boundaries, triple junctions) components. The portion of the intercrystalline components in polycrystalline materials is so small that its effect on observed properties is negligible whereas in nanocrystalline materials, not only do grain boundaries play an important role, but also triple lines and quadruple nodes can contribute significantly to deformation.

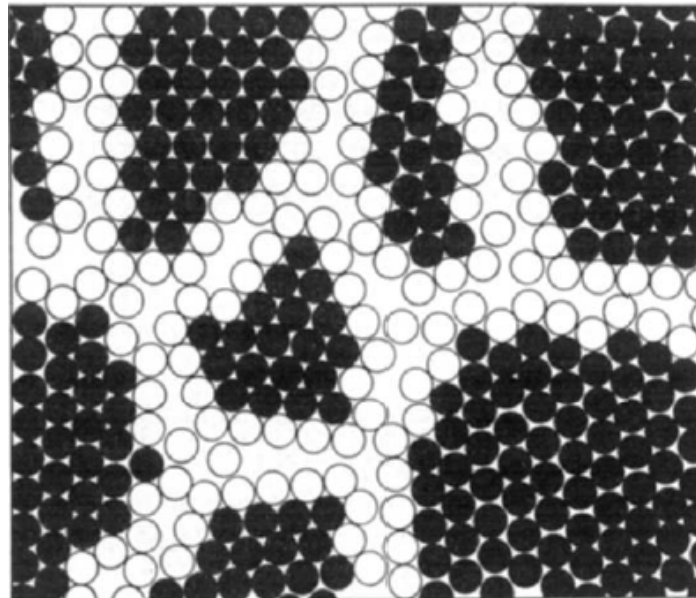


Fig. 1.1 Two-dimensional model of a nanostructured material. The atoms in the centers of the crystals are indicated in black. The ones in the boundary core regions are represented as open circles [1].

## **1.1.1 PROPERTIES OF NANOSTRUCTURED MATERIALS**

Nanostructured materials have received much interest because they exhibit different properties compared to coarse-grained polycrystals of the same material [5-11]. Some of the properties of nanocrystalline (nc) materials are summarized below.

### **1.1.1.1 STRENGTH AND HARDNESS**

The Hall-Petch equation [2,3] predicts very high values for the hardness/strength for the grain sizes less than 20 nm. As the grains become smaller, the effect of dislocation blocking increases, thereby strengthening the material. However, the experimental data fall well below these Hall-Petch extrapolations to the nano regime. In addition there appears to be a threshold grain size where materials begin to get softer with decreasing grain size, leading to “inverse Hall-Petch” behavior [12-18]. A cessation or reversal of the Hall-Petch hardening therefore limits the maximal hardness and strength that can be obtained in nanocrystalline metals by further refining of the grain size. Fig. 1.2 shows the variation of yield stress as a function of grain size, where strengthening occurs with grain refinement to a critical grain size of  $\sim 10$  nm, below which softening takes place. A number of models for the inverse Hall-Petch behavior have been proposed, but there is no consensus regarding their validity within the research community.

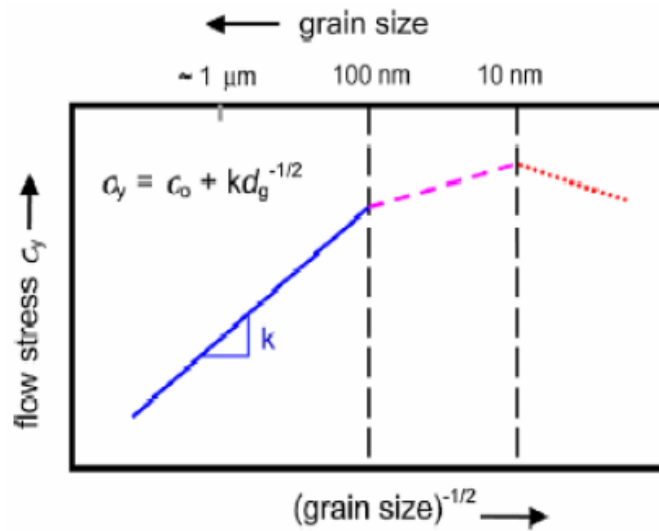


Fig. 1.2 Schematic representation of the variation of yield stress as a function of grain size from nanocrystalline to microcrystalline regimes [19].

These models include [20]:

- Enhanced Coble creep - Chokshi et al. [12] proposed that the inverse Hall-Petch behavior is caused by enhanced Coble creep, i.e. creep due to diffusion in the grain boundaries. Coble creep scales with the grain size ( $d$ ) as  $d^3$ , and estimates of the creep rate of nanocrystalline metals indicate that this could be the explanation of the inverse Hall-Petch behavior. Direct measurements of the creep rate have, however, ruled out this explanation [21-22].

- Suppression of dislocation pileups - Once the grain size drops below the equilibrium distance between dislocations in a pileup, pileups are no longer possible, and the Hall-Petch relation should cease to be valid [22-23].
- Porosity and flaws - Processing artifacts (pores, incomplete particulate bonding) have a negative effect on the strength and are the main reasons for the inverse Hall-Petch behavior observed in earlier studies. Improved processing techniques [24] have allowed production of nanocrystalline samples with densities above 98%; these have shown no inverse Hall-Petch behavior in copper at grain sizes down to approximately 10-15 nm [25]. Chen et al. have found Hall-Petch hardening in pure nanocrystalline Cu at grain sizes as small as 10 nm [26].

### **1.1.1.2 DUCTILITY**

Previously most of the work on the mechanical properties of nanocrystalline metals tended to concentrate on determining strength as a function of grain size. But accompanying the enhanced strength of nanocrystalline metals is a disappointing lack of ductility [27]. Many studies therefore have focused on devising methods to increase ductility and fracture toughness of these materials. Koch [28], after reviewing the available experimental data, identified three possible reasons for the limited ductilities observed in nano materials. They

are (1) artifacts from the processing, (2) force instability in tension and (3) crack nucleation or propagation instability. The development of artifact free materials using modern processing techniques has contributed significantly to an increase in strength as well as ductilities for these materials. Available literature suggests that having a bimodal grain size distribution results in high strength as well as good ductility in nanocrystalline materials [29-30].

### **1.1.1.3 ELASTIC PROPERTIES**

Though to a lesser extent than their plastic properties, the elastic properties of nanocrystalline metals have also been studied. Early studies [1,31] of the elastic behavior of nanocrystalline metals indicated that their elastic moduli are likely to be only a fraction of the coarse-grain values. The presence of residual porosity and incomplete particulate bonding were the reasons for the low value of elastic moduli. Sanders et al [32] investigated the effect of porosity on the Young's modulus of Pd and Cu, which is shown in Fig. 1.3. The figure shows that the extrapolation of Young's modulus to zero porosity yields modulus values in good agreement with the usual values.

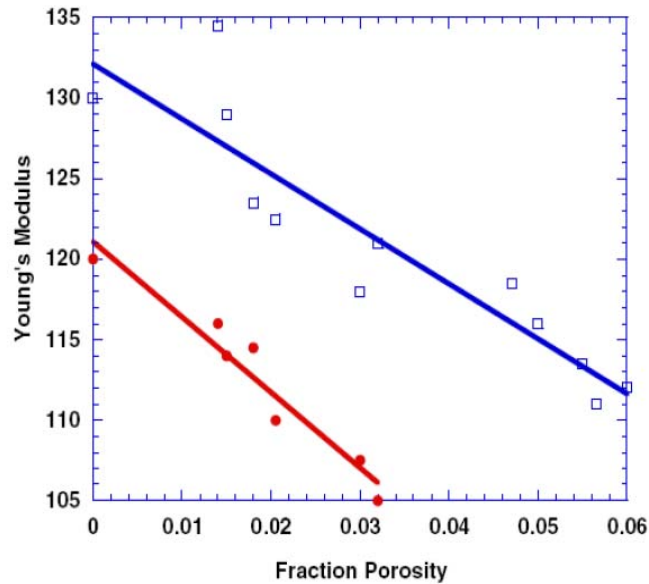


Fig. 1.3 Young's modulus as a function of porosity for nanocrystalline Pd and Cu [32].

#### 1.1.1.4 DIFFUSIVITY

The numerous interfaces in nanocrystalline materials provide a high density of short circuit diffusion paths. Thus, nanocrystalline materials are expected to exhibit an enhanced self diffusivity in comparison to single crystals or conventional polycrystals with the same chemical composition. This idea was confirmed by self diffusion measurements in nanocrystalline copper [33-35]. The nanocrystalline materials may be utilized technologically in areas where solids with high diffusivities are needed.

### **1.1.1.5 THERMAL STABILITY OF NANOSTRUCTURED MATERIALS**

The unique properties of nanostructured materials, when compared to their coarse grained counterparts, are attributed to the presence of a high volume fraction of internal interfaces. A large amount of energy stored in these interfaces (grain boundaries) provides a large driving force for grain growth and grain growth has been observed in nanocrystalline Pd and Cu at temperatures as low as room temperature [36-37]. Many enhancements in the properties of nanocrystalline materials due to the ultra-fine grain size are lost if grain growth occurs during application. Knowledge concerning methods for stabilizing the microstructure of nanocrystalline materials exposed to high temperatures is therefore highly desirable.

Two strategies have been employed to stabilize the structures against grain growth. The first relies on impurities at the grain boundaries to slow down the kinetics of grain growth through the process of solute drag [38-42]. The solute drag effect is based on the decrease of grain boundary mobility and free energy when solute segregates to the grain boundary. The second method, with which we are concerned here, involves changing the thermodynamics of grain growth in a way that results in the creation of a nanocrystalline metastable state. Theoretically and experimentally, it was shown that grain boundaries in nanomaterials have increased solubilities for solute atoms [43-44]. The enrichment of the grain boundaries with solute atoms of limited solubilities has shown to diminish or even reverse the free energy available for grain growth.

Weissmüller and co-workers [44–46] suggested that it is possible for nanocrystalline metallic alloys to be metastable, i.e. no tendency for grain growth, if  $E_{GB}$  (specific grain boundary energy) can be reduced to zero or below. Ignoring entropic effects, the variance of the  $E_{GB}$  with  $E_{seg}$  (enthalpy of segregation) is given by

$$E_{GB} = E_{GB(0)} - \{X_{solute}\}E_{seg}$$

where  $E_{GB(0)}$  is the specific excess free energy of a pure solvent and  $\{X_{solute}\}$  is the specific dopant coverage on the grain boundary. If  $E_{GB} \leq 0$ , due to a large and positive  $E_{seg}$  and /or  $\{X_{solute}\}$ , the total Gibbs free energy of a nanocrystal would be equal to or below that of the single crystal solid solution and the driving force for the grain growth is eliminated. In alloy systems of Pd-Zr [47] and Y-Fe [45], both of which have a high enthalpy of segregation, grain growth was suppressed upon increasing the solute concentration.

### 1.1.2 COMPUTER MODELING

Molecular dynamics (MD) calculations of inelastic deformation in nanocrystalline FCC metals have shown that once the grain size is reduced below approximately 10 nm, the deformation is dominated by grain boundary processes, such as atomic migration or grain boundary sliding. Schiøtz *et al.* [48] simulated the deformation of nanocrystalline copper, in the grain sizes ranging from 3.3 to 6.6 nm. These simulations showed material softening for

small grain sizes, in agreement with some experimental measurements. The simulations confirm that plastic deformation in the inverse Hall-Petch region occurs mainly by grain boundary sliding, with a minimal influence of dislocation motion on the deformation.

For grain sizes above approximately 10 nm, the deformation of nanocrystalline metals is a result of both atomic scale grain boundary processes and dislocation activity within the grains. Recently, there has been some debate in the literature regarding the existence of full dislocations in nanocrystalline grains during the deformation process. In a polycrystalline material, the size of Frank-Read sources cannot exceed the grain size. Because the stress needed for their operation is inversely proportional to the size of the source, this deformation mechanism can operate only down to a grain size of typically about 1  $\mu\text{m}$ . For a smaller grain size, mobile dislocations must be nucleated from other sources, such as the grain boundaries or grain junctions.

Van Swygenhoven using molecular dynamics simulations showed that at nanoscale a fundamentally different dislocation generation mechanism involving partials is operative. In nanocrystalline pure nickel and copper with a grain size of approximately 12 nm they showed that the leading (first) partial dislocation could be emitted from a grain boundary [49-50]. Through detailed analysis of the grain boundary structure [49,51-52] the nucleation of the first partial dislocation in nanocrystalline metals was shown to be assisted by local atomic shuffling within the interface and stress-assisted free volume migration. They have argued that the nucleation of the initial partial dislocation and the atomic rearrangement at the grain

boundary associated with its emission sufficiently lowers the grain boundary energy such that the emission of the trailing partial dislocation is not always needed to further relax the system [53].

MD simulations by Yamakov *et al.* [54-56] showed that the trailing partial dislocation may be emitted from grain boundary interfaces in aluminum. They suggested that the stacking fault width, and hence the intrinsic stacking fault energy, as defined by the distance between two partial dislocations is the central quantity that defines the transition from full to partial dislocation emission as grain size approaches the critical size for the onset of inverse Hall-Petch behavior.

More recent work by Van Swygenhoven and coworkers [53,57] has argued that interpreting the crossover between deformation regimes in terms of only the intrinsic stacking fault energy is insufficient. They emphasized that the entire generalized stacking fault curve [58] must be taken into consideration and proposed that the ratio of the unstable and intrinsic stacking fault energies is more appropriate to describe the observed dislocation activity in nanocrystalline samples.

### **1.1.3 NANOALLOYS**

The growing interest in nanostructured solids has mostly been focused on pure metals. Pure metals are suited as simple model systems for studying the properties related to the high

density of interfaces in nanostructured solids in terms of interface atomic structure. Nanocrystalline alloys represent an additional group of nanostructured solids. Because in these solids the density of topological defects is comparable to the density of alloy atoms, they promise to exhibit exciting new physical effects. At present there are two issues that are of particular importance. The first is the effect of an alloying component on the mechanical behavior of a nanocrystalline material and the second is the effect of the alloying component on grain boundaries on boundary stability.

The effects of Pb on the mechanical properties of nanocrystalline Al are uncertain based on several experimental results as discussed in more detail below [59-60]. In one case hardening was observed [59], while in the other there was a dramatic softening effect [60]. The latter investigators suggested that the Pb segregation to grain boundaries observed using *Z*-contrast high-resolution transmission electron microscopy (HRTEM) was the cause of the softening. Seonhee Jang [61] carried out molecular dynamics simulations for uniaxial tensile straining of two-dimensional columnar microstructures of aluminum (Al) and aluminum-lead (Al-Pb) alloys. A softening effect in agreement with, but less than that found experimentally was observed in her simulations.

Millett *et al.* [62] have used MD simulations to determine the stabilizing effect of a dopant atom in the vicinity of a Cu  $\Sigma 7$  symmetrical tilt grain boundary (STGB). Because this was a parametric study, relatively simple pair-additive Lennard-Jones interactions were used to model the interatomic forces. Although much less accurate for describing material properties

than many-body potential such as the embedded-atom method, they have the advantage that the properties of the impurities can be varied continuously in a straightforward manner. Impurity atom(s) of various characteristics and concentration were added to the near vicinity of the grain boundary to determine the structural and energetic effects.

They conclude that cohesive energy of a dopant atom does not have much effect on  $E_{GB}$  (specific grain boundary energy) upon segregation. On the other hand, the size of the dopant atom as compared to the host atoms is much more influential in affecting  $E_{GB}$ . Dopant atoms of both greater and smaller size compared to the surrounding Cu atoms caused a decrease in  $E_{GB}$  when they were brought closer to the grain boundary; however, the larger dopants were more effective in decreasing the energy.

It was also shown that the grain boundary energy could be reduced to zero, which has been theoretically proposed as necessary for achieving a metastable state for nanocrystals. The solute concentration in the grain boundary was gradually raised for each of the different dopant/host atomic size mismatches to determine if the  $E_{GB}$  can be reduced to zero or below. For each of the dopant atom sizes, this was achieved for a certain solute concentration, which increased with decreasing dopant/host atomic size mismatch.

Simulations that are similar in spirit to those done by Millett *et al.* and Seonhee Jang discussed above have been carried out in this thesis.

### 1.1.3.1 Al-Pb ALLOY SYSTEM

Immiscible alloy systems have been of great interest owing to their metastable structure formation in non-equilibrium processes and technological merits associated with them. It has been revealed that alloys could be synthesized in such systems with highly non-equilibrium processing methods such as melt spinning and ball milling [63-64]. Al-Pb is a typical immiscible binary alloy and a system on which some important alloys such as bearing alloys and solder materials are based.

Using melt spinning and ball milling, Sheng *et al.* produced Al-Pb nanocomposites with up to 30 wt. percent Pb [59]. In the solid state Pb is immiscible in Al, and therefore this nanocrystalline alloy could in principle be stabilized against grain growth. Based on several diffraction and microscopy techniques, it was concluded that the Pb forms faceted clusters in this alloy with sizes typically 5-30 nm prior to annealing. Formation of these clusters is consistent with a variety of other experimental studies that have characterized the structure, relationship to the lattice, and the melting properties of Pb clusters in Al [65-66]. Sheng *et al.* also reported a 50% increase in microhardness from the pure nanocrystalline Al to an alloy with 5 wt. % Pb. The microhardness was then found to decrease with increasing Pb content to roughly the pure nanocrystalline Al value. The authors speculate that up to the maximum in hardness with respect to Pb content the Pb particles impede dislocation motion. At larger Pb contents, the softer Pb particles compared to the Al soften the material, leading to the decrease in hardness.

In a recent experimental study by Rajulapati *et al.*, it was reported that the addition of up to one atomic percent Pb to nano-crystalline aluminum prepared by non-equilibrium high-energy ball milling results in a dramatic drop in microhardness from 925 MPa for the pure nanocrystalline Al to 555 MPa for the alloy [60]. As in prior studies, including the Sheng *et al.* study, Pb nanoparticles were observed in High Resolution Transmission Electron Microscopy (TEM) images. In addition, Z-contrast TEM images indicated that Pb atoms covered the grain boundaries in this system (Fig. 1.4). The authors suggest that the decrease in microhardness is due to the presence of these dispersed lead atoms, which alter the threshold for dislocation emission from the grain boundaries. Differences in processing conditions may explain the apparent discrepancies between the microhardness results of Rajulapati *et al.* and Sheng *et al.* Other than the Rajulapati *et al.* results, all other imaging studies have focused exclusively on the properties of incongruent Pb clusters in Al (including those formed across grain boundaries) and have not explored the possible segregation of Pb impurities towards Al grain boundaries. Establishing the validity of this segregation, and characterizing any associated grain boundary energy, is important in determining whether this system should show segregation induced thermal stability. In addition, predicting a minimum cluster size below which Pb prefers to segregate to grain boundaries compared to forming clusters both in the bulk and along the grain boundaries is also important in characterizing any associated formation of clusters in these systems.

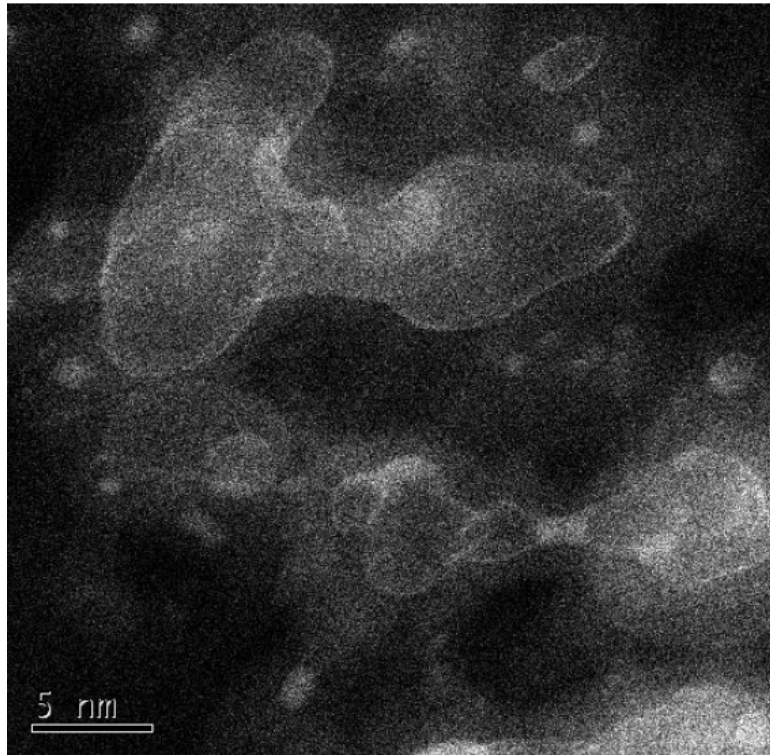


Fig. 1.4 Z-contrast image of in situ consolidated Al-1.0%Pb showing the Al grain boundaries covered with Pb atoms. The brighter region represents Pb phase and darker region represents Al phase [60].

Motivated by the Rajulapati *et al.* results and the issue of segregation-induced stability of grain boundaries in Al-Pb nanoalloys, we have used Monte Carlo simulations and analytic calculations to explore the segregation of Pb impurities to grain boundaries in an Al bicrystal and a three-dimensional nanocrystalline Al microstructure. The simulations, which use a modified-embedded atom method potential fit to first principles results, predict clustering of Pb within an ideal bulk Al lattice. In the case of the bicrystal and nanocrystalline structure,

the simulations predict segregation of Pb impurities towards the Al grain boundaries prior to cluster formation depending on the Pb content and the number of grain boundaries. In addition, for the nanocrystalline structure the Pb impurities also segregate toward triple junctions. Analysis of the local stress shows that the Pb atoms tend to initially segregate to lattice sites along the grain boundary that would otherwise be under hydrostatic tension, consistent with the larger effective size of Pb atoms compared to Al. After these sites are filled, the simulations predict the formation of individual Pb clusters across the grain boundaries. Hence the simulations support the conclusions of Rajulapati *et al.* These simulations, and subsequent calculations of the energies of Pb clusters in an Al matrix with the same potential function, predict a preference for the segregation of Pb atoms to grain boundaries compared to the formation of embedded Pb clusters with diameters less than about 2.8 nm. More importantly, analysis of the relative enthalpies for various substitutional Pb defects suggests that Pb impurities can help stabilize nanocrystalline Al against grain growth.

The stabilizing effect of Pb impurities on the energies of Al grain boundaries was investigated for two high symmetry  $\Sigma 5 \{210\}$  and  $\Sigma 5 \{310\}$  symmetrical tilt grain boundaries. This was done following the work by Millett *et al.* who studied the energy of a  $\Sigma 7$  grain boundary in Cu by adding impurity atoms of various characteristics and concentrations to the grain boundary [62]. Though it was a parametric study, it helped provide insights into the types and concentrations of solute atoms capable of substantially reducing grain boundary energy. We calculated energies of the above two-grain boundaries

as a function of the percentage of the coincident sites along the plane of atoms at the two-grain boundaries occupied by Pb atoms. They both showed a reduction in grain boundary energies with increasing Pb content. Stabilization was also confirmed by first principles calculations of the grain boundary energies of the above two boundaries.

Next, a dependence of the energies of  $\langle 100 \rangle$  symmetrical Al tilt boundaries over a complete range of misorientation angles with and without Pb substitution on the Al grain boundaries was investigated. A disclination-structural units model (DSUM) of grain boundaries that combines the structural units model [67-70] with the disclination [71-73] based description of grain boundaries was used for this purpose. The approach used energies from an atomistic potential for a few Pb doped key structures as input into the DSUM model [74-77]. The reliability of the DSUM was evaluated by calculating energies of a number of intermediate grain boundaries atomistically, using both the MEAM [78-82] and a 'Glue' type [83-84] interatomic potential and comparing these to predictions from the DSUM. The DSUM predicted a strong dependence of the grain stabilization energy on tilt angle.

The effects of Pb on the mechanical behavior of Al, based on several experimental studies as discussed above are uncertain [59-60]. Therefore, the aim in this dissertation is also to study the effect of Pb on the mechanical behavior in particular strength of Al. The MD simulations and a Glue-type interatomic potential were used to deform an Al bicrystal containing two  $\Sigma 5$   $\{210\}$  tilt boundaries, in uniaxial tension, with and without Pb substitution on the grain boundaries. Initial results showing the effect of Pb on the strength of Al are presented.

## **1.2 THESIS OBJECTIVES**

There are five main objectives to this dissertation:

1. To characterize cluster formation and the segregation of Pb impurities to grain boundaries in an Al bicrystal and a three-dimensional Al nanocrystal using Monte Carlo simulations.
2. To obtain a crossover cluster size below which Pb prefers to segregate to grain boundaries compared to forming clusters in bulk Al.
3. To investigate segregation-induced stability of grain boundaries in Al-Pb nanoalloys using atomistic MEAM and first principles calculations.
4. To establish the applicability of the disclination structural units model for alloys.
5. To study the effect of Pb on the mechanical behavior of Al using MD simulations.

## **1.3 THESIS ORGANIZATION**

In Chapter 2 the theory of atomistic simulations as relevant to this thesis is presented. It gives a brief overview of atomistic simulations, including temperature control methods. It outlines the fundamentals of the Monte Carlo and molecular dynamics method that were used for carrying out actual simulations.

Chapter 3 describes the two interatomic potentials - 1. The Modified Embedded Atom Method, and 2. The 'Glue' type potential that were used for modeling the structures and grain boundary energies of Al-Pb alloys.

In Chapter 4 the results of two types of simulations and calculations are reported. First are the structures predicted by the Monte Carlo simulations for a bulk Al-Pb alloy, an Al-Pb bicrystalline structure containing two  $\Sigma 5 \{210\}$  grain boundaries, and a nanocrystalline Al-Pb alloy. Calculations that predict relative enthalpies at 0K for several structures associated with the bicrystalline Al-Pb alloy are also presented. Second are the results of the effect of Pb on the mechanical behavior of Al. The molecular dynamics simulations in uniaxial tension were used to study deformation behavior in bicrystalline aluminum and aluminum-lead alloys.

In Chapter 5 the results of the calculations that show a stabilizing effect of Pb impurities on the energies of Al grain boundaries as a function of Pb content are presented. The calculations for the grain boundary energies were carried out using the atomistic MEAM and the first principles methods.

In Chapter 6, using a simple thermodynamic model, efforts have been made to predict a cross over cluster size below which Pb prefers to segregate to the grain boundaries compared to forming clusters in bulk Al.

In Chapter 7 the results of the application of a multiscale disclination structural units model (DSUM) for calculating energies of  $\langle 100 \rangle$  Al tilt grain boundaries over a complete range of misorientation angles with and without Pb atoms on the Al grain boundaries are presented.

Chapter 8 summarizes the outcomes of the present work and gives suggestions for the future work.

## REFERENCES

1. H. Gleiter, *Prog. Mater. Sci.*, 33 (1989) 223.
2. E. O. Hall, *Proc. Roy. Soc. London*, B64 (1951) 474.
3. N. J. Petch, *J. Iron Steel Inst.*, 174 (1953) 25.
4. H. Gleiter, *Nanostruct. Mater.*, 6 (1995) 3.
5. H. Gleiter, *Acta mater.*, 48 (2000) 1.
6. C. Suryanarayana, *Internat. Mater. Rev.*, 40 (1995) 41.
7. R. W. Siegel, *Materials Science and Technology—A Comprehensive Treatment*, Vol. 26: *Processing of Metals and Alloys*, ed. R.W. Cahn (Weinheim, Germany: VCH, 1991), pp. 583–614.
8. C. Suryanarayana et al., editors, *Processing and Properties of Nanocrystalline Materials* (Warrendale, PA: TMS, 1996).
9. R. S. Mishra et al., editors., *Ultrafine Grained Materials* (Warrendale, PA: TMS, 2000).
10. C. Suryanarayana, C. C. Koch, *Hyperfine Interactions*, 130 (2000) 5.

11. C. Suryanarayana, JOM, 54, 9 (2002) 24-27.
12. A. H. Chokshi, A. Rosen, J. Karch, H. Gleiter, Scripta Metall., 23 (1989) 1679.
13. G. E. Fougere, J. R. Weertman, R. W. Siegel, S. Kim, Scripta Metall. Mater. 26 (1992) 1879.
14. T. R. Malow, C. C. Koch, P. Q. Miraglia, and K. L. Murty, Mater. Sci. Eng. A, 252 (1998) 36.
15. T. Yamasaki, P. Schloßmacher, K. Ehrlich, Y. Ogino, Nanostruct. Mater. 10 (1998) 375.
16. C. Schuh, T. G. Nieh, T. Yamasaki, Scripta Mater., 46 (2002) 735.
17. C. Schuh, T. G. Nieh, H. Iwasaki, Acta Mater., 51 (2003) 431.
18. D. H. Jeong, U. Erb, K. T. Aust, G. Palumbo, Scripta Mater., 48 (2003) 1067.
19. K. S. Kumar, H. Van Swygenhoven, S. Suresh, Acta Mater., 51 (2003) 5743.
20. J. Schiøt, T. Vegge, F. D. Di Tolla, K. W. Jacobsen, Web-Article, Simulations of Mechanics and Structure of Nanomaterials – From Nanoscale to Coarser Scales.
21. G. W. Nieman, J. R. Weertman, R. W. Siegel, Scripta Metall. Mater. 24 (1990) 145.
22. T. G. Nieh, J. Wadsworth, Scripta Metall. Mater. 25 (1991) 955.
23. C. S. Pande, R. A. Masumura, R.W. Armstrong, Nanostruct. Mater. 2 (1993) 323.
24. P. G. Sanders, G. E. Fougere, L. J. Thompson, J. A. Eastman, J. R. Weertman, Nanostruct. Mater., 8 (1997) 243.
25. P. G. Sanders, C. J. Youngdahl, J. R. Weertman, Mater. Sci. Eng. A, 234-236 (1997) 77.
26. J. Chen, L. Lu, K. Lu, Scripta Mater., 54 (2006) 1913.
27. C. C. Koch, D. G. Morris, K. Lu and A. Inoue, MRS Bulletin, 24 (2) (1998) 54.
28. C. C. Koch, Journal of metastable and nanocrystalline materials, 18 (2003) 9.

29. Y. M. Wang, M. W. Chen, F. H. Zhou, E. Ma, *Nature*, 419 (2002) 912.
30. X. Zhang, H. Wang, R. O. Scattergood, J. Narayan, C. C. Koch, A.V. Sergueeva, A. K. Mukherjee, *Acta Mater.*, 50 (2002) 4823.
31. G. W. Nieman, J. R. Weertman, R. W. Siegel, *J. Mater. Res.*, 6 (1991) 1012.
32. P. G. Sanders, J. A. Eastman, J. R. Weertman, *Acta Mater.*, 45 (1997) 4019.
33. R. Birringer, H. Hahn, H. Hofler, J. Karch, H. Gleiter, *Defect and Diffusion Forum* 59 (1988) 17.
34. J. Horvath, R. Birringer, H. Gleiter, *Solid State Comm.* 62 (1987) 391.
35. J. Horvath, DIMETA-88, International Conference on Diffusion in Metals and Alloys, Balatonfiired, Hungary, September 5-9, 1988.
36. V. Y. Gertsman, R. Birringer, *Scripta Metall Mater.*, 30 (1994) 577.
37. J. Weissmüller, J. Loffler, M. Kleber, *Nanostruct. Mater.*, 6 (1995) 105.
38. V. Randle, (ed.), in *The Role of the Coincidence Site Lattice in Grain Boundary Engineering*, The Institute of Materials, Leeds, ISBN 1861250061, 1996.
39. P. Knauth, A. Charai, P. Gas, *Scripta Metall. Mater.*, 28 (1993) 325.
40. K. Boylan, D. Ostrander, U. Erb, G. Palumbo, K. T. Aust, *Scripta Metall. Mater.*, 25 (1991) 2711.
41. A. M. El-Sherik, K. Boylan, U. Erb, G. Palumbo, K. T. Aust, *Mat. Res. Soc. Symp. Proc.*, 238 (1992) 727.
42. R. J. Perez, B. Huang, A. A. Sharif, E. J. Lavernia, in *Synthesis and Processing of Nanocrystalline Powder*, p273, TMS, Warrendale, PA, 1996.
43. J. Weissmüller, *Nanostuct. Mater.*, 3 (1993) 261.

44. J. Weissmüller, "Nanocrystalline Materials – An Overview," in: synthesis and processing of Nanocrystalline Powder (D.L.Bourell,ed), pp. 3-19,TMS, Warrendale, PA (1996).
45. J. Weissmüller, W. K. Krauss, T. Haubold, R. Birringer, H. Gleiter, Nanostruct. Mater., 1 (1992) 439.
46. J. Weissmüller, J Mater. Res., 9 (1994) 4.
47. CE. Krill, R. Klein, S. Janes, R. Birringer, Mater. Sci. Forum, 179-181 (1995) 443.
48. J. Schiøtz, F. D. Di Tolla, K. W. Jacobsen, Nature 391 (1998) 561
49. H. Van Swygenhoven, M. Spaczer, A. Caro, D. Farkas, Phy. Rev. B, 60 (1999) 22.
50. H. Van Swygenhoven, A. Caro, D. Farkas, Mater. Sci. Eng. A, 309-310, (2001) 440.
51. H. Van Swygenhoven, P. M. Derlet, A. Hasnaoui, Phy. Rev. B, 66 (2002) 024101.
52. P. M. Derlet, H. Van Swygenhoven, A. Hasnaoui, Philo. Mag., 83 (2003) 3569.
53. H. Van Swygenhoven, P. M. Derlet, A. G. Froseth, Nature Materials, 3 (2004) 399.
54. V. Yamakov, D. Wolf, M. Salazar, S. R. Phillpot, H. Gleiter, Acta Mater., 49 (2001) 2713.
55. V. Yamakov, D. Wolf, S. R. Phillpot, H. Gleiter, Acta Mater., 50 (2002) 5005.
56. V. Yamakov, D. Wolf, S. R. Phillpot, H. Gleiter, Acta Mater., 51 (2003) 4135.
57. A. G. Froseth, P. M. Derlet, H. Van Swygenhoven, Acta Mater., 52 (2004) 5863.
58. J. A. Zimmerman, H. Gao, F. F. Abraham, Modell. Simul. Mater. Sci. Eng., 8 (2000) 103.
59. H.W. Sheng, F. Zhou, Z.Q. Hu and K. Lu, J. Mater. Res., 13 (1998) 308.
60. K.V. Rajulapati, R.O. Scattergood, K.L. Murty, G. Duscher, C.C. Koch, Scripta Mat. 55 (2006) 155.

61. S. Jang, Molecular Dynamics Simulations of Plastic Deformation in Nanocrystalline Metal and Alloy, (2007) PhD Thesis.
62. P. C. Millett, R. P. Selvam, S. Bansal, A. Saxena, *Acta Mater.*, 53 (2005) 3671.
63. C. C. Koch, O. B. Cavin, C. G. McKamey, J. O. Scarbrough, *Appl. Phys. Lett.*, 43 (1983) 1017.
64. R. B. Schwarz, R. R. Petrich, C. K. Saw, *J. Non-Cryst. Solids*, 76 (1985) 281.
65. E. Johnson, H. H. Andersen, U. Dahmen, *Microscopy Research and Technique*, 64 (2004) 356.
66. L. H. Zhang, E. Johnson, U. Dahmen, *Acta Mater.* 53 (2005) 3635.
67. A. P. Sutton, V. Vitek, *Philosophical Transactions of the Royal Society of London A*, 309 (1983) 1.
68. A. P. Sutton, V. Vitek, *Philosophical Transactions of the Royal Society of London A*, 309 (1983) 37.
69. A. P. Sutton, V. Vitek, *Philosophical Transactions of the Royal Society of London A*, 309 (1983) 55.
70. G. J. Wang, A. P. Sutton, V. Vitek, *Acta Metall.*, 32 (1984) 1093.
71. J. C. M. Li, *Surf. Sci.*, 31 (1972) 12.
72. K. K. Shih, J. C. M. Li, *Surf. Sci.*, 50 (1975) 109.
73. A. E. Romanov, *Mater. Sci. Eng. A*, 164 (1993) 58.
74. V. Y. Gertsman, A. A. Nazarov, A. E. Romanov, R. Z. Valiev, V. I. Vladimirov, *Philo. Mag. A*, 59 (1989) 1113.

75. R. Z. Valiyev, V. I. Vladimirov, V. Y. Gertsman, A. A. Nazarov, A. Y. Romanov, *Physics of Metals and Metallography*, 69 (1990) 30.
76. A. A. Nazarov, O. A. Shenderova, D. W. Brenner, *Mater. Sci. Eng. A*, 281 (2000) 148.
77. D. V. Bachurin, R. T. Murzaev, A. A. Nazarov, *Fizika Metallov i Metallovedenie*, 96 (2000) 11.
78. M. I. Bakes, *Phys. Rev. Lett.*, 59 (1987) 2666.
79. M. I. Baskes, I. S. Nelson, A. F. Wright, *Phys. Rev. B*, 40 (1989) 6085.
80. M. I. Baskes, *Phys. Rev. B*, 62 (1992) 2727.
81. M. I. Baskes, R. A. Johnson, *Modell. Simul. Mater. Sci. Eng.*, 2 (1994) 147.
82. M. I. Baskes, *Mater. Sci. Eng. A*, 261 (1999) 165.
83. F. Ercolessi, M. Parrinello, E. Tosatti, *Philo. Mag.*, 58(1) (1988) 213.
84. A. Landa, P. Wynblatt, D. J. Siegel, J. B. Adams, O. N. Mryasov, X.-Y. Liu, *Acta mater*, 48 (2000) 1753.

## **CHAPTER 2**

### **FUNDAMENTALS OF ATOMISTIC SIMULATIONS**

#### **2.1 INTRODUCTION**

In this chapter the theory of atomistic simulations as related to this thesis is presented. First a general overview of atomistic simulations, which includes a brief description of thermodynamic ensembles, is presented. It is followed by a description of the atomistic methods and algorithms that were used in the present work. Section 2.3 and Section 2.4 outlines the fundamentals of the Monte Carlo and molecular dynamics methods, respectively. A description of the temperature control methods and periodic boundary conditions used in this work are given in Sections 2.5 and 2.6, respectively. All of the above background will help give a clearer understanding of the following chapters.

#### **2.2 ATOMISTIC SIMULATIONS**

Atomistic simulations model materials at the level of atoms. It refers to a group of computational methods such as molecular mechanics [1-2], dynamics [3-6] and Monte Carlo [6-10] algorithms that can be used to model the interactions, configurations and properties of a system of atoms. In this framework, each atom is represented as a point mass in space that interacts with other atoms of the system through an interatomic potential [11-19]. The

interatomic potential provides a model for the potential energy of a system of atoms. The accuracy of property prediction relies on the proper choice of potential function. Commonly, the total potential energy of the system is written solely as a function of the positions of the atomic nuclei. This simplification avoids having to specifically account for the motion and interaction of the individual electrons. Since interatomic forces are conserved, the force on a given atom,  $F_i$ , is related to the interatomic potential,  $U$ , through the gradient operator. The force on a given atom,  $F_i$  is then obtained from the potential function,  $U$ , using:

$$F_i = -\frac{\partial U(r_N)}{\partial r_i} \quad (1)$$

where  $r_N$  represents the position vectors for the system of  $N$  atoms while  $r_i$  is the atomic position vector for the  $i^{\text{th}}$  atom. Detailed information regarding the interatomic potentials used for calculations in this work is presented in Chapter 3.

### **2.2.1 THERMODYNAMIC ENSEMBLES**

Atomistic simulations are conducted under well-defined thermodynamic conditions. These conditions specify the “ensemble” of the systems [20]. Atomistic simulations are commonly classified into two categories: equilibrium and nonequilibrium. In equilibrium atomistic simulations, the system is completely isolated from its surroundings with a fixed number of atoms, volume and constant total energy. These boundary conditions correspond to the

microcanonical (NVE) ensemble in statistical mechanics. For molecular dynamics, the natural ensemble is the microcanonical ensemble (NVE) because Newton's equations lead naturally to energy conservation. Unfortunately, the microcanonical ensemble does not correspond to the conditions under which most experiments are carried out. To run simulations at other non-NVE statistical ensembles we must introduce a thermostat and/or a barostat in the system. Depending on the equations of motion that describe the system of atoms, these calculations may correspond to the canonical (NVT) and/or the isothermal-isobaric (NPT) ensemble in statistical mechanics. There are several schemes that have been devised to thermostat systems treated with atomistic simulations. A brief description of the thermostating methods used in this work is given in Section 2.5.

The ensemble average of a physical quantity,  $A$ , can be written as:

$$\langle A \rangle = \sum_1^M A_i P_i, \quad M \approx \infty \quad (2)$$

In the above equation,  $A_i$  represents the value of the physical quantity  $A$  associated with each of the  $M$  accessible microstates ( $i = 1 \dots M$ ) of the system and  $P_i$  the probability of the system to be in microstate  $i$  with energy  $E_i$  respectively. The form of  $P_i$  is determined by which macroscopic properties are common to all the systems of the ensemble. For example, if the number of atoms ( $N$ ), volume ( $V$ ) and temperature ( $T$ ) are constant then it can be shown that

$$P_i = \frac{e^{-\beta E_i(NV)}}{Z_{NVT}} \quad (3)$$

where  $E$  is the energy,  $\beta = 1/K_B T$  and  $Z_{NVT}$  is the partition function, i.e.,

$$Z_{NVT} = \sum_i e^{-\beta E_i(NV)} \quad (4)$$

For an exact mean, the total number of microstates  $M$  should approach infinity. Because in reality we can generate only a finite number  $m$  of the total number of  $M \approx \infty$  microstates, we only obtain an estimate for the mean value of the physical quantity  $A$ :

$$\langle A \rangle \approx \sum_1^m A_i P_i \quad (5)$$

The accuracy of the estimate obtained by simulations therefore depends directly on the quality (or the way  $m$  representative conformations are chosen.) of the representative  $m$  conformations.

### 2.3 METROPOLIS MONTE CARLO ALGORITHM

Monte Carlo (MC) simulation is a stochastic approach to performing atomistic simulations that uses repeated random moves to explore the geometry of a molecular system. In a simple

sampling method, the  $m$  conformations are chosen randomly. The immense majority of these conformations has energy very different from the average energy of the system and hence contributes little to the mean. This gave rise to the idea of importance sampling. The idea of importance sampling in Monte Carlo simulations is to choose a representative set of conformations in such a way that the selection is biased towards conformations that are significantly populated at equilibrium. Metropolis Monte Carlo [7] is one such importance sampling method and has been used in the present work.

Monte Carlo simulation methods based on the Metropolis algorithm have been successfully used to study segregation phenomena in various alloy structures [21-23]. They can circumvent slow physical dynamic processes such as diffusion in the alloy systems and therefore makes calculation faster. The simulations using the Metropolis algorithm were performed in the canonical ensemble, where the total number of atoms of each element, volume and the temperature were held constant. Starting from an arbitrary configuration, a new system configuration is accepted or rejected based on the Boltzmann probability distribution function.

For our simulations, each Monte Carlo step consisted of the repetition of the following two moves:

- (1) A small random displacement of 10% of randomly chosen atoms in a system, which allowed for thermal vibrations in atomic positions and contributed to stress relief.

(2) The exchange of atom identities between Pb and Al, which allowed the placement of substitutional Pb atoms into their equilibrium positions.

Each move that lowers the potential energy of a new configuration was accepted. Moves that raise the potential energy were accepted if a random number was smaller than the ratio of Boltzmann factors for the system after and before the move.

A schematic of the algorithm used to construct the Metropolis random walk is given in Fig. 2.1 and is also described below.

**Step 1. Initialize:**

a. Initialize the system configuration with coordinates  $xyz\_old$  and energy  $energy\_old$ .

**Step 2. Atom Move:**

a. Make a change in the configuration to obtain a new configuration 2 with coordinates  $xyz_2$  and energy  $e_2$ .

b. If  $e_2 < energy\_old$ , accept the new configuration with coordinates  $xyz_2$ , and assign  $e_2$  to  $energy\_old$  and  $xyz_2$  to  $xyz\_old$  .)

c. If  $e_2 > energy\_old$ , generate a random number  $R1$ . If  $R1 < \exp((-e_2-energy\_old)/K_B T)$ , then accept the new configuration  $xyz_2$ , and assign  $e_2$  to  $energy\_old$  and  $xyz_2$  to  $xyz\_old$ . If

$R1 > \exp((-e_2 - \text{energy\_old})/K_B T)$ , then revert back to the old energy  $\text{energy\_old}$  and assign  $\text{xyz\_old}$  to  $\text{xyz}_2$ .

**Step 3. Atom identity swap:**

- a. Swap the identity of element Al with Pb.
- b. Calculate energy of this configuration with coordinate  $\text{xyz}_2$  to be  $e_3$ .
- c. If  $e_3 < \text{energy\_old}$ , accept the new configuration with coordinate  $\text{xyz}_2$ , and assign energy  $e_3$  to  $\text{energy\_old}$  and  $\text{xyz}_2$  to  $\text{xyz\_old}$ .
- d. If  $e_3 > \text{energy\_old}$ , generate a random number  $R1$ . If  $R1 < \exp((-e_3 - \text{energy\_old})/K_B T)$ , then accept the new configuration  $\text{xyz}_2$  and assign energy  $e_3$  to  $\text{energy\_old}$  and  $\text{xyz}_2$  to  $\text{xyz\_old}$ . If  $R1 > \exp((-e_3 - \text{energy\_old})/K_B T)$ , then swap back atom identity and revert back to the old energy,  $\text{energy\_old}$ , and old coordinates,  $\text{xyz\_old}$ .

**Step 4:**

- a. Go back to step 2 with  $\text{xyz\_old}$  and  $\text{energy\_old}$ .

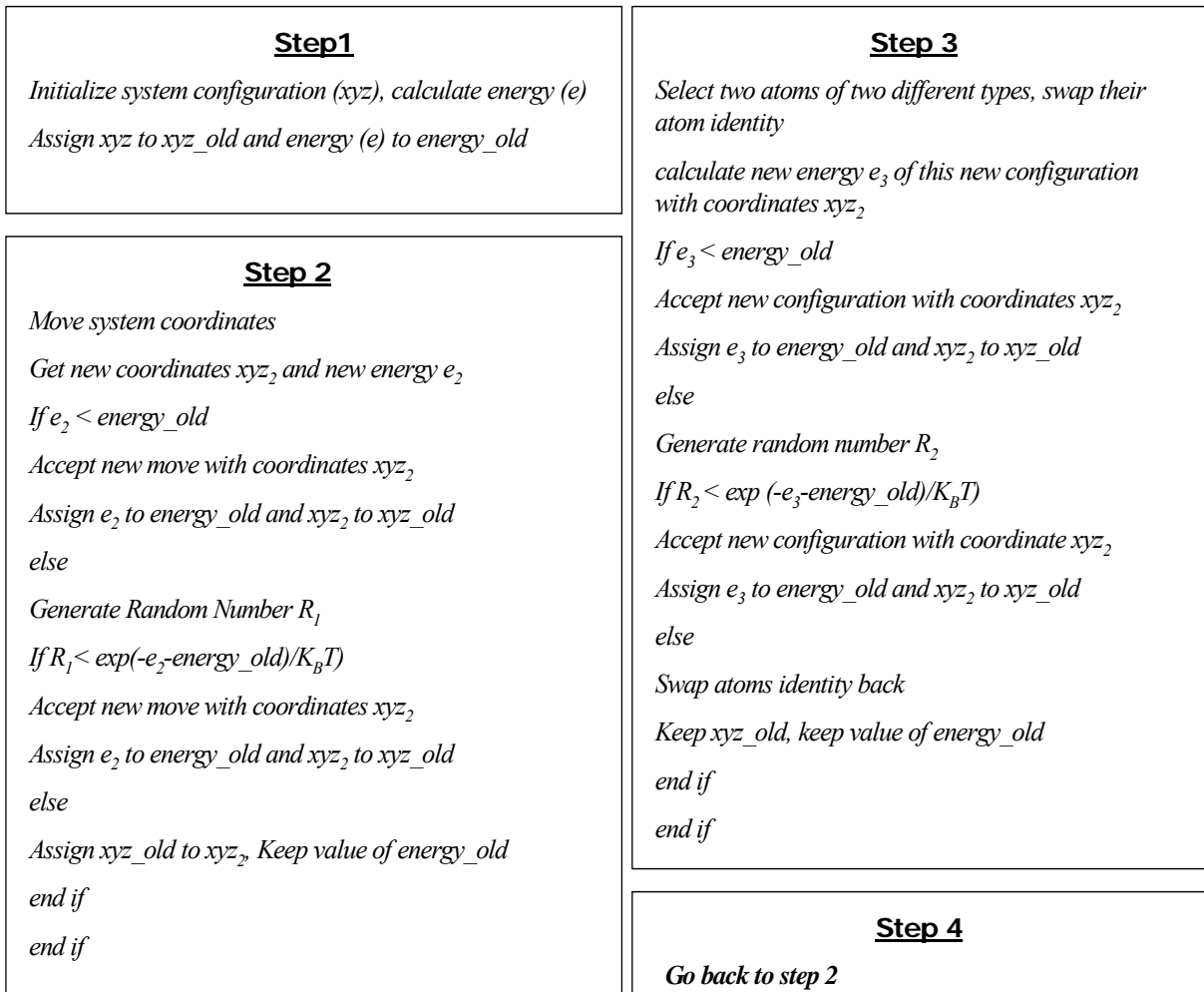


Fig. 2.1 Schematic of Metropolis Monte Carlo Algorithm.

## 2.4 MOLECULAR DYNAMICS

Molecular dynamics (MD) is a computer simulation method to follow the motion of particles with time by numerically integrating classical equations of motion. A general flow chart for a classical MD simulation is shown in Fig. 2.2. When an MD simulation is started for the very first time, one needs to specify the initial arrangement of the atoms in space, their initial momenta and parameters that determine the interatomic potential. The momenta in some cases need to be scaled such that they match an initial input temperature. Atoms in the system interact with each other through an interatomic potential. A neighbor list allows one to dramatically reduce the number of possible interactions one needs to actually consider. A neighbor list is created at the beginning of the simulation. Upon subsequent calls to the neighbor list, the list gets updated automatically. Forces between particles are calculated from the gradient of the energy function. The time integration algorithms allow one to integrate the equation of motion of the interacting particles and follow their trajectory. Knowing the positions and some of their time derivatives at time  $t$  (the exact details depend on the type of algorithm), the integration scheme gives the same quantities at a later time  $t + \delta t$ . For constant temperature (or pressure) simulations, atoms are also required to interact with a thermostat (or barostat). By iterating the above procedure, the time evolution of the system can be followed for long times. After a period of time the system approaches thermodynamic equilibrium and the physical properties of interest can then be calculated.

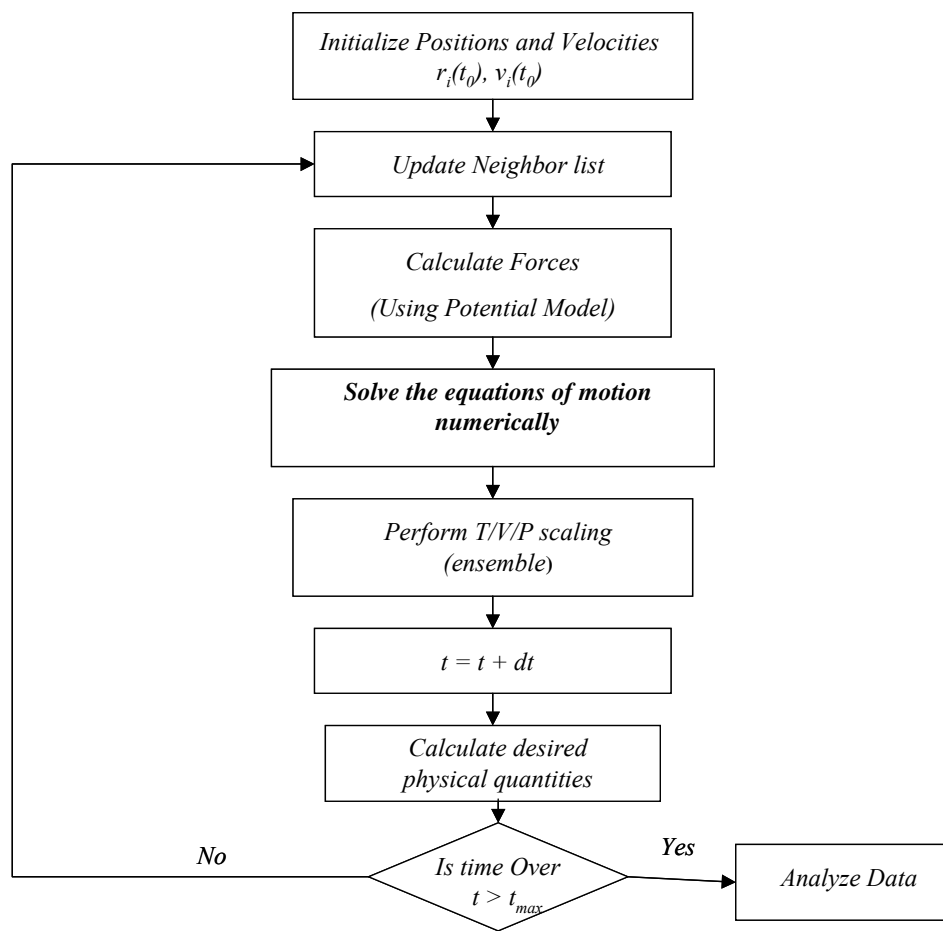


Fig. 2.2 A general flow chart for molecular dynamics simulation.

## 2.4.1 INTEGRATORS

Different methods can be used to solve the classical equations of motion. Two popular integration methods for MD calculations are the velocity Verlet algorithm [24-25] and the predictor-corrector algorithms [26-28]. The MD code with the MEAM potential was implemented with a velocity Verlet integrator and the code with the Glue-type potential was implemented with a predictor-corrector integrator.

### 2.4.1.1 VELOCITY VERLET ALGORITHM

In the velocity Verlet algorithm positions and velocities at time  $t + \delta t$  are obtained from the same quantities  $r(t)$ ,  $v(t)$  at time  $t$  in the following way:

Given  $r(t)$ ,  $v(t)$  and  $f(t)$

**Step 1:** Calculate position at  $t + \delta t$  and velocity at  $t + \delta t/2$

$$r(t + \delta t) = r(t) + v(t)\delta t + \left(\frac{1}{2}\right)\left(\frac{f(t)}{m}\right)\delta t^2 \quad (6)$$

$$v(t + \delta t/2) = v(t) + \left(\frac{1}{2}\right)\left(\frac{f(t)}{m}\right)\delta t \quad (7)$$

**Step 2:** Evaluate force at  $t + \delta t$ ;  $f(t + \delta t)$ .

**Step 3:** Calculate velocity at  $t + \delta t$

$$v(t + \delta t) = v(t + \delta t/2) + \left(\frac{1}{2}\right)\left(\frac{f(t + \delta t)}{m}\right)\delta t \quad (8)$$

Now all quantities for the new step  $t + \delta t$  have been found, go back to step 1. Here,  $\delta t$  is the molecular dynamics time step for the simulation, which is typically on the order of femtoseconds and  $m$  is the particle mass.

This algorithm has many desirable properties because its form is exactly time reversible (which allows the equations of motion to be propagated forward in time without iteration) and symplectic (the volume in phase space is conserved), insuring long simulation time stability and convergence.

#### **2.4.1.2 PREDICTOR-CORRECTOR ALGORITHM**

The predictor-corrector algorithm constitutes another commonly used class of methods to integrate the equations of motion. It consists of three steps:

**Step1:** Predictor - From the positions and their time derivatives, all known at time  $t$ , one “predicts” the same quantities at time  $t + \delta t$  by means of a Taylor expansion.

$$\begin{aligned}
 r^P(t + \delta t) &= r(t) + \delta t v(t) + 1/2 \delta t^2 a(t) + 1/6 \delta t^3 b(t) + \dots \\
 v^P(t + \delta t) &= v(t) + \delta t a(t) + 1/2 \delta t^2 b(t) + \dots \\
 a^P(t + \delta t) &= a(t) + \delta t b(t) + \dots \\
 b^P(t + \delta t) &= \dots
 \end{aligned}
 \tag{9}$$

The  $p$  superscript refers to predicted values. The variables are

$r$  = position

$v$  = velocity  $\left(\frac{dr}{dt}\right)$

$a$  = acceleration  $\left(\frac{d^2r}{dt^2}\right)$

$b$  = Third derivative of position with respect to time  $\left(\frac{d^3r}{dt^3}\right)$

**Step 2:** Force evaluation - The force is computed at time  $t + \delta t$  taking the gradient of the potential at the predicted positions. The resulting acceleration value called corrected acceleration at time  $t + \delta t$ ;  $a^c(t + \delta t) = \frac{F}{m}$  will be in general different from the “predicted

acceleration”  $a^P(t + \delta t)$ . The difference between the two constitutes an error (which represents the discrepancy between Taylor-series second derivative and the acceleration calculated explicitly from force).

$$\Delta a(t + \delta t) = a^C(t + \delta t) - a^P(t + \delta t) \quad (10)$$

**Step 3: Corrector** - This error is used to “correct” positions and their derivatives. All the corrections are proportional to the error, with the coefficient of proportionality ( $c_0, c_1, c_2, \dots$ ) determined to maximize the stability and accuracy of the algorithm.

$$\begin{aligned} r^C(t + \delta t) &= r^P(t + \delta t) + c_0 \Delta a(t + \delta t) \\ v^C(t + \delta t) &= v^P(t + \delta t) + c_1 \Delta a(t + \delta t) \\ a^C(t + \delta t) &= a^P(t + \delta t) + c_2 \Delta a(t + \delta t) \\ b^C(t + \delta t) &= \dots \end{aligned} \quad (11)$$

The positions, velocities etc. are now a better approximation to the true solutions of the equations of motion. The values of proportionality constants for the Nordsieck-Gear [27-28] second order predictor- corrector (using the first three derivatives of position) are given in Table 2.1.

Table 2.1 Coefficient values for a second order Nordsieck-Gear predictor-corrector method.

$C_0 = 1/6$	$C_1 = 5/6$	$C_2 = 1$	$C_3 = 1/3$
-------------	-------------	-----------	-------------

The predictor-corrector algorithm can achieve a higher degree of energy conservation than the velocity Verlet algorithm with a longer time step. However, velocity Verlet algorithms are easier to implement than predictor corrector algorithms.

## 2.5 THERMOSTATS

Appropriate temperature control methods must be incorporated into simulations that maintain constant temperature. The temperature is defined by the ensemble average of the kinetic energies of all particles as:

$$\left\langle \frac{1}{2}mv^2 \right\rangle = \frac{K_B T}{2} \quad (12)$$

Therefore it is impossible to fix  $T$  exactly at a set point. Two techniques for temperature control are commonly used: (i) Direct velocity rescaling and (ii) The extended system method. Direct velocity rescaling involves resetting the velocities of the particles at each time step so that the total kinetic energy of the system remains strictly constant. This approach is

simple and straightforward to code and was used in our Monte Carlo simulations. They suffer the drawback that they are not time-reversible or deterministic, properties that become important in some advanced MD techniques.

In the extended system method, the system is allowed to interact with the surrounding environment through some thermal constraints. The system may be coupled to a heat bath to ensure that the average system temperature is maintained close to the requested temperature. When this is done the equations of motion are modified and the system no longer samples the microcanonical ensemble. Instead trajectories in the canonical (NVT) ensemble, (or something close to it) are generated. Many different methods exist to specify the interaction between the atomic system and the environment. The Nose-Hoover thermostat is one such method and has been used in our MD simulations.

### **2.5.1 HOOVER THERMOSTAT**

The Hoover (NH) thermostat is an ‘extended’ system thermostat that incorporates an external temperature reservoir into the system. The equations of motion for the system are augmented by a ‘frictional’ coefficient,  $\xi$ , which couples the system dynamics to the reservoir. Hoover [29] extended the analysis of Nose [30] (who proposed first such equations for the NVT ensemble) and developed the following equations for the NVT ensemble.

$$\begin{aligned}\dot{r}_i &= \frac{p_i}{m} \\ \dot{p}_i &= F_i - \xi p_i \\ \dot{\xi} &= \frac{1}{Q} \left( \sum_{i=1}^N \frac{p_i^2}{m_i} - (f+1)K_B T \right)\end{aligned}\tag{13}$$

where  $f$  is the degrees of freedom of the physical system (e.g. 3N),  $T$  is the desired temperature and  $Q$  is the ‘fictitious’ mass of the additional degree of freedom (reservoir). The choice of  $Q$  is critical in the implementation of this thermostat. The thermodynamic ‘friction’ constant dynamically alters the velocities of the individual atoms such that the temperature of the system is adjusted towards the desired temperature. The Nose-Hoover thermostat is more complicated than other methods. However, it is also the best and, therefore, most used thermostat today for NVT simulations.

## 2.6 PERIODIC BOUNDARY CONDITIONS

Atomistic simulations generate information at the microscopic level. The conversion of microscopic information to macroscopic observables such as pressure, energy, heat capacities, etc., requires statistical mechanics. The main idea behind using atomistic simulation is to describe system’s macroscopic behavior in terms of microscopic information and to obtain information that is not easily obtained from experiments. But, despite the rapid advancement of computer power, simulating systems with more than a few million atoms at

one time is still expensive. Simulations are therefore limited to systems with tens of thousand of atoms on personal computers and about a billion atoms on super computers. To model a macroscopic system in terms of a finite simulation system of  $N$  particles, the concept of periodic boundary conditions [3] is often employed. They are useful for simulating a part of a bulk system with no surfaces present and they have been used in all of our simulations.

Fig. 2.3 illustrates the concept of periodic boundary conditions. The primary cell is outlined with solid lines and it represents an actual system one is interested in simulating. The primary simulated box is replicated throughout space to form an infinite lattice. Every atom in the simulation box therefore has an exact duplicate (or image) in each of the surrounding “image” cells. A result is that whenever an atom leaves the simulation cell, it is replaced by another atom with exactly the same velocity, entering from the opposite cell face. Therefore, the number of atoms in the cell is conserved. Note that atoms that lie near the borders of the primary computational cell interact with neighbor atoms across the periodic boundary. While periodic boundary conditions remove the effects of free surfaces, they impart image constraints on the system that must be taken into consideration when simulating defect behavior with long-range interactions.

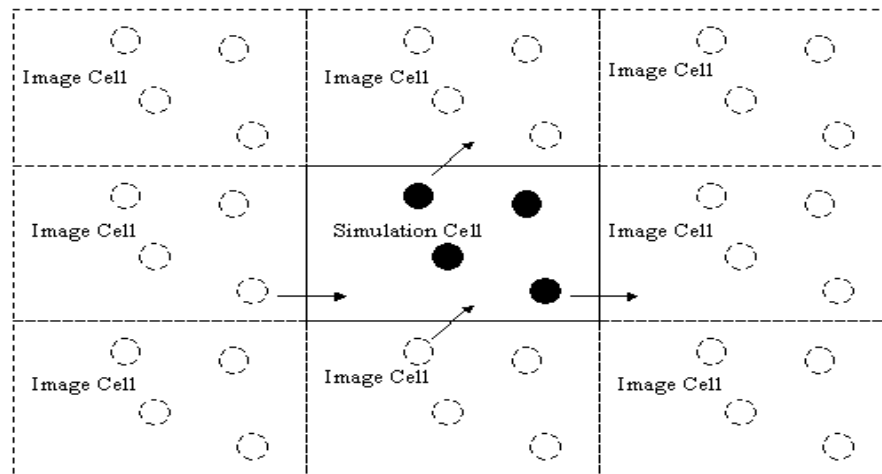


Fig. 2.3 Illustration of periodic boundary conditions.

## REFERENCES

1. U. Burkert, N. L. Allinger, *Molecular Mechanics*, (1982).
2. J. R. Shewchuk, *An introduction to the conjugate gradient method without the agonizing pain*, (1994), Carnegie Mellon University.
3. M. P. Allen, D. J. Tildesley, *Computer Simulations of Liquids*, (1987), Clarendon Press, Oxford.
4. J. M. Haile, *Molecular Dynamics Simulation: Elementary Methods*, (1992), Wiley, New York.
5. D. C. Rapaport, *The Art of Molecular Dynamics Simulation*, (2004), 2nd ed. Cambridge University Press.

6. D. Frenkel, B. Smith, *Understanding Molecular Simulations: From Algorithms to Applications*, (1996), Academic Press.
7. N. Metropolis, A. W. Rosenbluth, M. N. Rosenbluth, A. H. Teller and E. Teller, *J. Chem. Phys.*, 21 (1953) 1087.
8. K. Binder, editor, *Monte Carlo Methods in Statistical Physics*, (1986), second edition, Springer-Verlag.
9. K. Binder, editor, *Applications of the Monte Carlo Method in Statistical Physics*, (1984), Springer-Verlag.
10. K. Binder, editor, *The Monte Carlo Method in Condensed Matter Physics*, (1992) Springer-Verlag.
11. S. Foiles, M. Baskes, M. Daw, *Phys. Rev. B*, 33 (1986) 7983.
12. M. Finnis, J. Sinclair, *Philos. Mag. A*, 50 (1984) 49.
13. K. Jacobsen, J. Norskov, M. Puska, *Phys. Rev. B*, 35 (1987) 7423.
14. F. Ercolessi, J. Adams, *Europhys. Lett.*, 26(8) (1994) 583.
15. F. Ducastelle, *Computer simulations in material science*, (1991), Kluwer, Dordrecht.
16. A. Sutton, *Electronic Structure of Materials*, (1993), Clarendon Press, Oxford.
17. A. E. Carlsson, (1990). Beyond pair potentials in elemental transition metals and semiconductors. *Solid State Physics*, 43, Academic Press, New York, 1-91.
18. M. I. Baskes, *Phys. Rev. B*, 62 (1992) 2727.
19. M. I. Baskes, *Mater. Chem. Phys.*, 50 (1997) 152.
20. W. Greiner, L. Neise, H. Stocker, (1995). *Thermodynamics and Statistical Mechanics*, Springer-Verlag, New York.

21. P. Deurinck, C. Creemers, Surf. Sci., 441 (1999) 493.
22. S. M. Foiles, Phys. Rev. B, 32 (1985) 7685.
23. X. Y. Liu, P. P. Ohotnicky, J. B. Adams, C. L. Rohrer, R. W. Hyland, Surf. Sci., 373 (1997) 357.
24. L. Verlet, Phys. Rev. 159 (1967) 98.
25. W. C. Swope, H. C. Anderson, P. H. Berens, K. R. Wilson, J. Chem. Phys. 76 (1982) 637.
26. S. C. Chapra, R. P. Canale, Numerical Methods for Engineers, (1988), McGraw-Hill, New York.
27. C. W. Gear, Numerical initial value problems in ordinary differential equations, (1971), Prentice-Hall, Englewood Cliffs, NJ.
28. A. Nordsieck, Math Comp., 20 (1962) 13.
29. S. Nose, Molecular Physics, 52 (1984) 255.
30. W. G. Hoover, Phys. Rev. A, 31 (1985) 1695.

## CHAPTER 3

### INTERATOMIC POTENTIAL FOR Al-Pb ALLOY

#### 3.1 INTRODUCTION

A modified embedded atom method interatomic potential designed for Al-Pb alloys was used in this work. Among various semiempirical atomic potentials, the embedded-atom method (EAM) proposed by Daw *et al.* [1-3] has been very successful in various applications [4]. However, the EAM potential has limitations in describing alloys and compounds because it cannot deal with elements that have directional bonding characteristics. Baskes proposed the modified EAM (MEAM) that includes angular contributions of electron density to describe the directionality of bonding [5-9].

These potentials are derived as an approximation to the local density functional theory. They are analogous to effective-medium [10] theory in that every atom in the EAM and the MEAM formalism is viewed as an embedded impurity in the bulk of other atoms and therefore renders a good description of many-body atomic interactions in the system. Compared to the EAM, the local background electron density around the  $i^{th}$  atom in the MEAM, which incorporates many body effects, is augmented by an angularly dependent term. This allows MEAM potentials to describe not only face-centered-cubic (fcc) elements but also hexagonal-close-packed (hcp), bodycentered - cubic (bcc), and diamond cubic

elements that exhibit the directionality of atomic bonding. The directional bonding permits a better representation of the inhomogeneous environment around an atom when its surrounding neighbors are from different species. This enables the MEAM potential to be highly applicable to alloy systems. Moreover, the determination of the pair interactions involves principally a reference structure and the universal equation of state, which precludes any further parameterization of the potential as required for EAM potentials.

The MC simulations and the atomistic calculations to predict the structures and the segregation-induced stability of grain boundaries in Al-Pb nanoalloys, as discussed in chapters 4 and 5, were carried out using the MEAM potential. The MEAM potential was developed following the procedure given by Baskes and coworkers, with its parameters fit to the results of first principles DFT calculations. Calculations given in chapter 6 and 7 pertaining to a cluster-to-segregation cross over size determination and the DSUM model were also performed using the MEAM potential.

In Chapter 7 a Glue-type potential [11] along with the MEAM potential for the Al-Pb alloy is used to further establish the validity of the DSUM results. The empirical many-body force scheme, named the Glue model, was developed by Ercolessi in 1988. Like the EAM it was able to overcome the many well-known difficulties associated with the use of two-body forces for the description of metallic systems [11]. The Glue potential for the Al-Pb systems used in this thesis was developed by Landa *et al.* [12]. It was constructed using the “force matching” method. The potential was fitted to experimental data, physical quantities derived

from ab initio linear muffin-tin orbitals calculations and a massive quantum mechanical database of atomic forces generated using ultrasoft pseudopotentials in conjunction with ab initio molecular statics simulations.

The Glue-type interatomic potential is computationally simple and therefore faster when compared to the MEAM potential. That prompted us to further use it for carrying out simulations pertaining to tensile deformation of Al-Pb alloys (Chapter-4). The Glue potential gave reasonable values for the stacking fault energy of Al.

### 3.2 MEAM FORMALISM

The total energy  $E$  of a system of single type of atoms in the MEAM can be written as:

$$E_{Tot} = \sum_i \left( F_i(\bar{\rho}_i) + \frac{1}{2} \sum_{j(\neq i)} \phi_{ij}(R_{ij}) \right) \quad (1)$$

where the sums are over the atoms  $i$  and  $j$ . In the above equation,  $\bar{\rho}_i$  is the background electron density at the center of atom  $i$  obtained by the superposition of electronic densities from its surrounding atoms. The essential difference between the EAM and the MEAM is in the way  $\bar{\rho}_i$  is computed. The function  $F_i$  is the embedding function which is the energy

required to embed the atom  $i$  into the background electron density,  $\bar{\rho}_i$ , at site  $i$  and  $\phi_{ij}(R_{ij})$  is the pair interaction between atoms  $i$  and  $j$  whose separation is given by  $R_{ij}$

Within the EAM, the background electron density is calculated using a linear superposition of the densities from the neighboring atoms, i.e.,

$$\bar{\rho}_i(R_{ij}) = \sum_{j(\neq i)} \rho_j^a(R_{ij}) \quad (2)$$

where  $\rho_j^a$  is the contribution to the density from atom  $j$  at a distance  $R_{ij}$  from site  $i$ .

The embedding energy in the MEAM is given as follows:

$$F_i(\bar{\rho}_i) = AE_c \left( \frac{\bar{\rho}_i}{\bar{\rho}^0} \right) \ln \left( \frac{\bar{\rho}_i}{\bar{\rho}^0} \right) \quad (3)$$

where  $A$  is an adjustable parameter,  $E_c$  is the sublimation energy, and  $\bar{\rho}^0$  is the background electron density for a reference structure. Normally, the equilibrium structure is taken as the reference structure for elements.

In the EAM the background electron density is a simple sum of radially dependent contributions from the other atoms. In the MEAM the electron density is composed of a

spherically symmetric partial electron density  $\rho_i^{(0)}$  (which is equivalent to  $\bar{\rho}_i(R_{ij})$  in the EAM), plus angular contribution  $\rho_i^{(1)}$ ,  $\rho_i^{(2)}$ ,  $\rho_i^{(3)}$ . These partial electron densities have the following forms:

$$\rho_i^{(0)} = \sum_{j(\neq i)} \rho_j^{a(0)}(R_{ij}) \quad (4a)$$

$$(\rho_i^{(1)})^2 = \sum_{\alpha} \left\{ \sum_{j(\neq i)} \frac{R_{ij}^{\alpha}}{R_{ij}} \rho_j^{a(1)}(R_{ij}) \right\}^2 \quad (4b)$$

$$(\rho_i^{(2)})^2 = \sum_{\alpha\beta} \left\{ \sum_{j(\neq i)} \frac{R_{ij}^{\alpha} R_{ij}^{\beta}}{R_{ij}^2} \rho_j^{a(2)}(R_{ij}) \right\}^2 - \frac{1}{3} \left\{ \sum_{j(\neq i)} \rho_j^{a(2)}(R_{ij}) \right\}^2 \quad (4c)$$

$$(\rho_i^{(3)})^2 = \sum_{\alpha\beta\gamma} \left\{ \sum_{j(\neq i)} \frac{R_{ij}^{\alpha} R_{ij}^{\beta} R_{ij}^{\gamma}}{R_{ij}^3} \rho_j^{a(3)}(R_{ij}) \right\}^2 - \frac{3}{5} \sum_{\alpha} \left\{ \sum_{j(\neq i)} \frac{R_{ij}^{\alpha}}{R_{ij}} \rho_j^{a(3)}(R_{ij}) \right\}^2 \quad (4d)$$

Here,  $x_{ij}^{\alpha} = \frac{R_{ij}^{\alpha}}{R_{ij}}$ , and  $R_{ij}^{\alpha}$  is the  $\alpha$  component ( $\alpha = x, y$  or  $z$ ) of the distance vector between atom  $j$  and  $i$ . The quantity  $\rho_j^{a(h)}$  ( $h=0, 1, 2,$  and  $3$ ) represents atomic electron densities from atom  $j$  at a distance  $R_{ij}$  from site  $i$  and is given by:

$$\rho_j^{a(h)}(R) = e^{-\beta(h) \left( \frac{R}{r_c} - 1 \right)} \quad (5)$$

where  $\beta^{(h)}$  are adjustable parameters and  $r_e$  is the nearest neighbor distance in the equilibrium reference structure.

In the MEAM, these partial contributions can be combined to give the total background electron density in several ways. In this work, we use the following scheme (see other schemes in Ref. [13]) to combine the partial electron densities and compute the background electron density:

$$\bar{\rho}_i = \rho_i^{(0)} G(\Gamma) \quad (6)$$

where  $G(\Gamma) = \frac{2}{1 + e^{-\Gamma}}$ ,  $\Gamma = \sum_{h=1}^3 t_i^{(h)} \left( \frac{\rho_i^{(h)}}{\rho_i^{(0)}} \right)^2$  and  $t_i^{(h)}$  are adjustable parameters.

In the MEAM a specific form is given to the embedding function, but not to the pair interaction. Instead a reference structure where individual atoms are on the exact lattice points is defined and the total energy per atom of the reference structure is estimated from the zero temperature universal equation of state by Rose *et al.* [14]. Then the value of the pair interaction is evaluated from the known values of the total energy per atom as

$$\Phi(R_{ij}) = \frac{2}{Z} [E^u(R_{ij}) - F(\bar{\rho}^0(R_{ij}))] \quad (7)$$

where  $Z$  is the number of nearest neighbors in the bulk reference structure and  $E^u(R_{ij})$  is the energy per atom of the reference structure as a function of nearest-neighbor distance  $R_{ij}$ .

The function  $E^u(R_{ij})$  is determined using the following universal equation of state of Rose *et al.* [14].

$$E^u(R_{ij}) = -E_c(1 + a^*)e^{-a^*} \quad (8a)$$

$$a^* = \alpha(R_{ij}/r_e - 1) \quad (8b)$$

$$\alpha = \sqrt{\frac{9\Omega B}{E_c}} \quad (8c)$$

where  $E_c$ ,  $r_e$ ,  $\Omega$  and  $B$  are the sublimation energy, nearest-neighbor distance, atomic volume, and bulk modulus for the equilibrium reference structure, respectively.

$\bar{\rho}^0(R_{ij})$  in Eq. (7) is the background electron density for the reference structure.

For fcc metals,

$$\bar{\rho}^0(R_{ij}) = Z\rho^{a(0)}(R_{ij}) \quad (9)$$

### 3.2.1 SCREENING PROCEDURE

In the MEAM calculations presented in this work, only first nearest neighbor interactions were considered. This was done using the many body screening function proposed by Baskes [13]. According to this method the screening function,  $S_{ik}$ , that quantifies the screening between two atoms  $i$  and  $k$  due to other atoms  $j$  in the system can be written as

$$S_{ik} = \prod_{j(\neq i,k)} S_{ijk} \quad (10)$$

where  $S_{ijk}$  is calculated using a simple geometric construction illustrated in the Fig. 3.1.

$$S_{ijk} = f_c \left( \frac{C - C_{\min}}{C_{\max} - C_{\min}} \right) \quad (11)$$

where  $f_c(x)$  is a function of the material dependent parameters  $C_{\min}$  and  $C_{\max}$ . The parameter  $C$  is determined using the following equation

$$C = \frac{2(X_{ij} + X_{jk}) - (X_{ij} - X_{jk})^2 - 1}{1 - (X_{ij} - X_{jk})^2} \quad (12)$$

where  $X_{ij} = \left(\frac{r_{ij}}{r_{ik}}\right)^2$  and  $X_{jk} = \left(\frac{r_{jk}}{r_{ik}}\right)^2$ ;  $r_{ij}$ ,  $r_{jk}$ , and  $r_{ik}$  are the distances between the corresponding atoms,  $C_{\min}$  and  $C_{\max}$  are the limiting values of  $C$  as seen in the ellipses in Fig. 3.1. Atoms bounded by  $C_{\max} = 2.8$  do not screen atoms  $i$  and  $k$  while those bounded by  $C_{\min}$  (inside the full (dashed) curve for  $C_{\min} = 0.8$  (2.0)) screens atoms  $i$  and  $k$  completely.

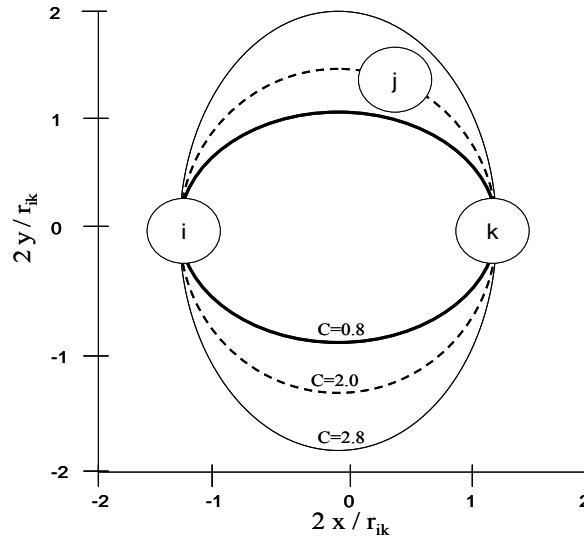


Fig. 3.1 Potential screening of atoms  $i$  and  $k$  by atom  $j$  [13].

The smooth cutoff function  $f_c(x)$  in Eq. (11) assumes the following form.

$$\text{If } x \geq 1, f_c(x) = 1$$

$$\text{If } 0 < x < 1, f_c(x) = [1 - (1-x)^4]^2 \quad (13)$$

$$\text{If } 0 < x < 1, f_c(x) = 0$$

We multiply the atomic electron density and the pair potentials by the screening function  $S_{ik}$ ; hence  $S_{ik} = 1$  represents an unscreened interaction while  $S_{ik} = 0$  represents a completely screened interaction. In addition, a radial cut-off function is also applied to reduce calculation time. The cut-off radius used for the energy calculation is 4.0 Å.

### 3.3 Al-Pb ALLOY MEAM POTENTIAL

To construct an Al-Pb alloy MEAM potential, parameters for pure Al and Pb were taken from Lee et al. [15] and are given in Table 3.1. These parameters provide an excellent fit to the bulk and surface properties of these elements.

Table 3.1 Parameters for the MEAM potential of Al and Pb. The units of the sublimation energy  $E_c$ , and the equilibrium nearest-neighbor distance  $r_e$ , are the eV and Å<sup>0</sup> respectively.

	$E_c$	$r_e$	$\alpha$	$A$	$\beta(0)$	$\beta(1)$	$\beta(2)$	$\beta(3)$	$t(0)$	$t(1)$	$t(2)$	$t(3)$
Al	3.36	2.86	4.69	1.16	3.20	2.6	6.0	2.6	1.0	3.05	0.51	7.75
Pb	2.04	3.5	6.38	1.01	5.42	2.2	6.0	2.2	1.0	3.10	3.91	1.25

To describe an alloy system, the pair interaction between different elements needs to be determined. For this, a similar technique that is used to determine the pair interaction for pure elements can be applied to a binary alloy system. Therefore, the main work in describing alloy systems using the MEAM is to estimate the potential parameters for the universal equation of state for the alloy reference structure. Due to the immiscibility of Pb in Al, experimental data to which MEAM parameters can be fitted are extremely limited. Therefore parameters for the Al-Pb MEAM cross terms were fitted to the results of first principles density functional theory (DFT) calculations [16-17] on a hypothetical Al-Pb alloy with a NaCl (B1) structure. Details of the DFT calculations for calculating the lattice constant, the cohesive energy and the elastic constants for Al-Pb, B1, reference structure are given in Section 3.4.

For the B1 (NaCl) reference structure, where each Al atom has only Pb atoms as neighbors and vice versa, the total energy per atom is given by [7]:

$$E_{ij}^u(R) = \frac{1}{2} \left[ F_i(Z_{ij} \rho_j^{a(0)}(R)/Z_i) + F_j(Z_{ij} \rho_i^{a(0)}(R)/Z_j) + Z_{ij} \phi_{ij}(R) \right] \quad (14)$$

where  $Z_{ij}$  is the number of neighbors within the alloy,  $Z_i$  and  $Z_j$  those corresponding to the pure elements.

The pair interaction between Al and Pb can be obtained from the above equation:

$$\phi_{ij}(R) = \frac{1}{Z_{ij}} \left[ 2E_{ij}^u(R) - F_i(Z_{ij}\rho_j^{a(0)}(R)/Z_i) - F_j(Z_{ij}\rho_i^{a(0)}(R)/Z_j) \right] \quad (15)$$

In the above two equations i and j corresponds to Al and Pb, respectively. The embedding functions  $F_{Al}$  and  $F_{Pb}$  were calculated from the expressions (3) given above. To obtain  $E_{AlPb}^u$ , the universal equation of state for the Al-Pb (B1) structure was considered. The parameters  $E_c$ ,  $r_e$  (or  $\Omega$ ),  $\alpha$  for the reference Al-Pb alloy structure (NaCl structure) were evaluated using DFT results (for  $\Delta_{AlPb}$ ,  $a_0(AlPb)$ , B) using following equations:

$$E_c(AlPb) = (E_c(Al) + E_c(Pb))/2 - \Delta_{AlPb} \quad (16a)$$

$$r_e(AlPb) = a_0(AlPb)/2 \quad (16b)$$

$$\alpha(AlPb) = \sqrt{\frac{9\Omega(AlPb)B(AlPb)}{E_c(AlPb)}} \quad (16c)$$

The calculated values are given in Table 3.2.

Table 3.2 Parameters for the MEAM potential for the Al-Pb alloy. The units of the sublimation energy  $E_c$ , and the equilibrium nearest-neighbor distance  $r_e$ , are the eV and Å<sup>0</sup> respectively.

	$E_c$	$r_e$	$\alpha$	$A$	$\beta(0)$	$\beta(1)$	$\beta(2)$	$\beta(3)$	$t(0)$	$t(1)$	$t(2)$	$t(3)$
AlPb	2.39	2.98	5.05	-	-	-	-	-	-	-	-	-

Besides the parameters for the universal equation of state ( $E_c$ ,  $r_e$  (or  $\Omega$ ), and  $\alpha$ , which represents material properties) there are two more model parameters  $c_{\min}$  and  $\rho_{\text{scale}}$  that should be determined to describe alloy systems. The  $c_{\min}$  determines the extent of screening of an atom (j) to the interaction between two neighbor atoms (i and k). For pure elements, the three atoms are all of the same type. However, in the case of alloys, one of the interacting atoms and/or the screening atoms can be of a different type. There can be different combinations such as A-B-A, B-A-B, A-A-B, B-B-A, A-B-B. Different values of  $C_{\min}$  may have to be given to different combinations. Table 3.3 gives the angular screening parameters  $C_{\min}$  for the different combinations of Al-Pb alloy. Here, the middle atom is the “screening” atom and the outer atoms are the “interacting” atoms. The  $C_{\max}$  values are 2.80 for all the combinations.

Table 3.3 Angular screening parameters for the Al-Pb alloy MEAM potential.  $C_{\max}$  values are 2.80 for all the combinations.

	AlAlAl	AlAlPb	AlPbAl	PbAlAl	PbPbAl	PbAlPb	AlPbPb	PbPbPb
$C_{\min}$	0.49	1.0	1.4	1.0	1.0	1.0	1.0	0.81

Another model parameter is the atomic electron density scaling factor  $\rho_{\text{scale}}$ . For an equilibrium reference structure ( $R = r_e$ ), the value of all atomic electron density becomes  $\bar{\rho}^0$ . This is an arbitrary value and does not have any effect on calculations for the pure elements. Any arbitrary value can be given to an element in calculations for pure elements. However, for alloy systems the scaling factor (relative difference) might have a great effect on calculations. Its value for Al and Pb was fitted to be 1.31 and 0.98 respectively. It was fitted to the elastic properties and the cohesive energy offsets for the two crystal structures. Transferability of the alloy parameters was then tested by comparing the physical properties of a second Al-Pb crystal structure, CsCl (B2), with the reference structure, NaCl (B1), as calculated by both the MEAM and first principles DFT. Table 3.4 compares the calculated properties of B1 and B2, and shows satisfactory agreement between the MEAM and the DFT results.

### **3.4 DFT CALCULATIONS**

The Vienna ab-initio [18-20] software package and the accompanying library of ultrasoft pseudopotentials [21-22] were used to calculate lattice constants, bulk moduli, cohesive energies, and elastic stiffness coefficients for face-centered cubic Al and Pb as well as AlPb in the B1 and B2 crystal structures. All calculations were performed using the gradient corrected local density approximation of Perdew and Wang [23] and the plane waves were expanded out to a kinetic energy cutoff of 300 eV. The Monkhorst-Pack [24] method was

used to generate special k-points from a uniform mesh of 35x35x35 for the primitive face-centered cubic and primitive B2 crystal structures while a 31x31x31 mesh was used for the primitive B1 structure. The ultrasoft pseudopotentials explicitly treat 14 and 3 valence electrons for Pb and Al, respectively, and partial occupancies were determined with the tetrahedron method with Blöchl corrections. This method of smearing would result in inaccurate forces in metals but is used because of its ability to provide the most accurate energies of the unoptimized primitive cell. Equilibrium lattice parameters, cohesive energies, and bulk moduli were found by fitting the energy vs. volume data to the Murgahan equation of state (EOS) for small strains of 0.0000,  $\pm 0.0025$ ,  $\pm 0.0050$ , and  $\pm 0.0075$  around an approximate minimum energy lattice parameter. Calculated cohesive energies were taken with reference to the spin-polarized ground state of the isolated atoms. The elastic stiffness coefficients,  $C_{11} - C_{12}$ , were calculated using the above strain around the equilibrium lattice obtained from the fit to the Murgahan EOS through use of the volume conserving orthorhombic strain method of Mehl et al. [25].

Table 3.4 Comparison of the properties of two hypothetical Al-Pb alloys given by first principles DFT calculations and the MEAM potential. The NaCl structure is used to determine the MEAM parameters; the CsCl structure is used to establish the transferability of the MEAM.

	MEAM	DFT
<b>Properties of NaCl (Reference)</b>		
Lattice Constant, $a_0$ ( $\text{\AA}$ )	5.97	5.97
Heat of Mixing, $\Delta_{AlPb}$ , (eV/atom)	0.315	0.315
Bulk Modulus, B (GPa)	40.65	40.66
Elastic Constant, $C_{11}-C_{12}$ , (GPa)	74.91	75.72
<b>Properties of CsCl</b>		
Lattice Constant, $a_0$ ( $\text{\AA}$ )	3.66	3.71
Heat of Mixing, $\Delta_{AlPb}$ , (eV/atom)	0.28	0.275
Bulk Modulus, B (GPa)	53.95	44.57
Elastic Constant, $C_{11}-C_{12}$ , (GPa)	0.42	0.29

## REFERENCES

1. M. S. Daw, M. I. Baskes, Phys. Rev. Lett., 50 (1983) 1285.

2. M. S. Daw, M. I. Baskes, Phys. Rev. B., 29 (1984) 6443.
3. S. M. Foiles, M. I. Baskes, M. S. Daw, Phys. Rev. B., 33 (1986) 7983.
4. M. S. Daw, S. M. Foiles, M. I. Baskes, Materials Science Reports, 9 (1993) 251.
5. M. I. Bakes, Phys. Rev. Lett., 59 (1987) 2666.
6. M. I. Baskes, I. S. Nelson, A. F. Wright, Phys. Rev. B, 40 (1989) 6085.
7. M. I. Baskes, Phys. Rev. B, 62 (1992) 2727.
8. M. I. Baskes, R. A. Johnson, Modell. Simul. Mater. Sci. Eng., 2 (1994) 147.
9. M. I. Baskes, Mater. Sci. Eng. A, 261 (1999) 165.
10. J. K. Norskov, Phys. Rev. B, 26 (1982) 2875.
11. F. Ercolessi, M. Parrinello, E. Tosatti, Philo. Mag., 58(1) (1988) 213.
12. A. Landa, P. Wynblatt, D. J. Siegel, J. B. Adams, O. N. Mryasov, X.-Y. Liu, Acta mater, 48 (2000) 1753.
13. M. I. Baskes, Mater. Chem. Phys., 50 (1997) 152.
14. J. H. Rose, J. R. Smith, F. Guinea, and J. Ferrante, Phys. Rev. B, 29 (1984) 2963.
15. B.-J. Lee, J.-H. Shim, M. I. Baskes, Phys. Rev. B, 68 (2003) 144112.
16. P. Hohenberg, W. Kohn, Phys. Rev., 136 (1964) B864.
17. W. Kohn, L. J. Sham, Phys. Rev., 140 (1965) 1133.
18. G. Kresse, J. Hafner, Phys. Rev. B, 47 (1993) 558
19. G. Kresse, J. Furthmüller, Comput. Mat. Sci., 6 (1996) 15.
20. G. Kresse, J. Furthmüller, Phys. Rev. B, 54 (1996) 11169.
21. D. Vanderbilt, Phys. Rev. B, 41 (1990) 7892.
22. G. Kresse, J. Hafner, J. Phys: Condens. Matt., 6 (1994) 8245.

23. Y. Wang, J. P. Perdew, Phys. Rev. B, 43 (1991) 8911.
24. H. J. Monkhorst, J. D. Pack, Phys. Rev. B, 13 (1976) 5188.
25. M. J. Mehl, J. E. Osburn, D. A. Papaconstantopoulos, B. M. Klein, Phys. Rev. B, 41 (1990) 10311.

## CHAPTER 4

### MODELING OF THE STRUCTURES FORMED BY SUBSTITUTIONAL Pb IMPURITY IN Al AND ITS EFFECT ON MECHANICAL BEHAVIOR

#### 4.1 INTRODUCTION

Motivated by the Rajulapati *et al.* results [1] and the issue of segregation-induced stability of grain boundaries in Al-Pb nanoalloys (Section 1.1.3.1), we have used Monte Carlo simulations and analytic calculations to explore the segregation of Pb impurities to grain boundaries in an Al bicrystal and a three-dimensional nanocrystalline Al microstructure.

The results of two types of simulations and calculations are reported in this chapter. The first are the structures predicted by the Monte Carlo simulations for a bulk Al-Pb alloy, an Al-Pb bicrystalline structure containing two  $\Sigma 5$  {210} grain boundaries, and a nanocrystalline Al-Pb alloy. Interatomic interactions in the Al-Pb alloy system were described using a modified embedded atom method potential with parameters fit to the results of density functional theory calculations (Chapter-3). The simulations show the formation of Pb clusters in bulk Al, as observed experimentally [2-3], which qualitatively establishes the validity of the model. The simulations also show segregation of Pb atoms to grain boundaries in the bicrystal and nanocrystal. To explore the applicability of grain stabilizing metastability theory for Al-Pb alloys, the relative enthalpies at 0K are calculated for several structures associated with the bicrystalline Al-Pb alloy. Included are the structures with half and all of the

coincident sites along the plane of atoms at the two grain boundaries occupied by Pb atoms. Analysis of the relative enthalpies for Pb defects suggests that Pb segregation to grain boundaries in Al can stabilize the structures against grain growth.

The effects of Pb on the mechanical behavior of Al, based on several experimental studies, are uncertain. Therefore, in the second set of simulations efforts have been made to study the effect of Pb on the mechanical behavior, particularly strength of Al. The MD simulations and a Glue-type interatomic potential are used to deform an Al bicrystalline configuration in uniaxial tension, with and without Pb substitution on the grain boundaries. Initial results showing the effect of Pb on the strength of Al are presented.

## **4.2 METHODOLOGY**

All of the three atomic systems, as mentioned above, used periodic boundary conditions in each direction, with lattice sites corresponding to an Al face-centered cubic lattice. The bulk system was comprised of a cube containing 4000 atoms. The Al bi-crystal was generated in the periodic structure as two complementary tilt grain boundaries with  $\Sigma 5 \langle 100 \rangle \{210\}$  configurations (Fig. 4.1a). The system contained 40,000 atoms, with box sizes of 4.50 nm and 9.05 nm in the two directions parallel to the grain boundaries, and 18.11 nm in the direction normal to the grain boundaries. A schematic of atomic sites at the  $\Sigma 5 \{210\}$  tilt grain boundary is shown in Fig. 4.1b. Site 1 is a coincident site and sites 2, 3, 4 are off coincident sites for the grain boundary. There are two atomic planes along the  $\langle 100 \rangle$

direction. The open and closed circles represent atoms distributed on the first and second  $\{100\}$  planes, respectively.

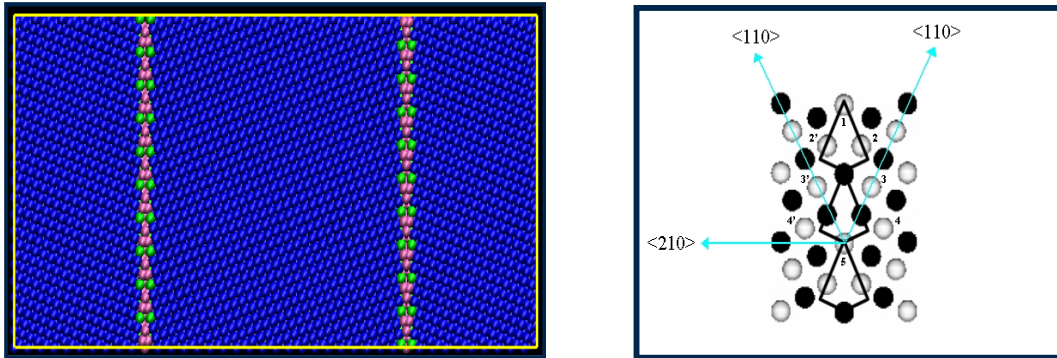


Fig. 4.1 Illustration of the Al bicrystalline geometry. (a) Entire Al bicrystal containing two complementary  $\Sigma 5$   $\langle 100 \rangle$   $\{210\}$  tilt grain boundaries. Bulk atoms are shown in blue and other colors represent GB atoms. (b) A schematic of the  $\Sigma 5$   $\langle 100 \rangle$   $\{210\}$  tilt grain boundary. The open and closed circles represent atoms on the  $\{100\}$  and  $\{200\}$  planes, respectively.

To generate a three-dimensional nanostructure, grain shapes were first generated using a Johnson-Mehl (JM) tessellation algorithm [4]. The algorithm models the grain nucleation and growth processes and produces a distribution of grain shapes and sizes with a log-normal distribution. According to this algorithm, grains nucleate anywhere in the structure, with equal probability for all spatial locations. However, when a nucleation point is chosen that is already occupied by a growing grain, a new nucleation point is chosen. Then grains grow radially at a constant rate. When two grains impinge, growth ceases at the point of contact,

while continuing elsewhere. Fig. 4.2a illustrates these three JM tessellation conditions. Random Euler angles for each grain were then chosen that correspond to rotational angles of the cubic lattice within the grain. Atoms were then populated on the appropriate lattice sites within each grain (Fig. 4.2b). Atoms at the grain boundaries that were closer than 75% of the equilibrium first neighbor distance were removed from the system prior to the Monte Carlo simulations.

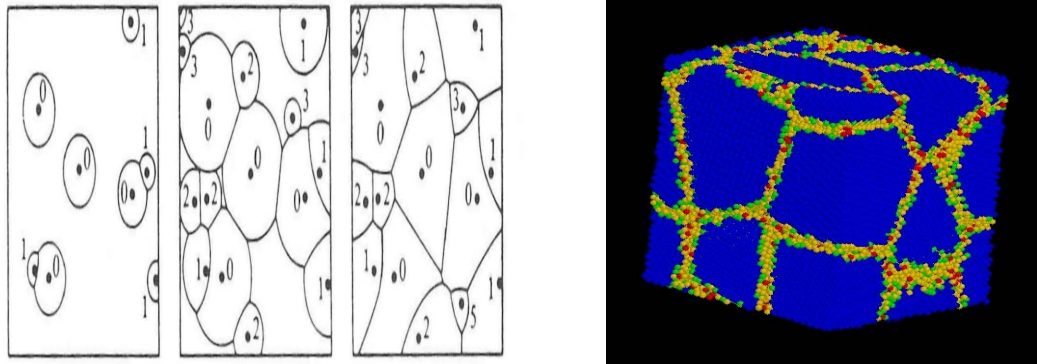


Fig. 4.2 (a) Johnson-Mehl nucleation and grain growth process. (b) A polycrystalline nanostructure with an average grain size of 5 nm. Atoms are colored by centrosymmetry parameter [15]. Blue represents bulk fcc atoms and other colors represent grain boundary atoms.

All of the simulations were carried out using two Monte Carlo events (Section 2.3). The first is a small random displacement of 10% of randomly chosen atoms in a system. The second event is the exchange of atom identities between a single pair of randomly chosen Al and Pb

atoms. The former allows for thermal vibrations and contributes to stress relief. The second allows the placement of substitutional Pb atoms into their equilibrium positions. This procedure does not follow the time evolution of the segregation, but rather is intended to create equilibrium structures. Acceptance or rejection of a given move is determined using the standard Metropolis algorithm [5] in which a move that lowers the potential energy is accepted. Moves that raise the potential energy are accepted if a random number is smaller than the ratio of Boltzmann factors for the system after and before the move. All simulations were carried out at 300K.

## **4.3 RESULTS AND DISCUSSION**

### **4.3.1 BULK Al-Pb ALLOY**

To simulate structures associated with substitutional Pb atoms in an ideal Al crystal, 1% of the Al atoms (40 atoms) in the initial perfect lattice were randomly replaced with Pb atoms (Fig. 4.3a). The Monte Carlo procedure discussed above was then carried out for a total of 1.9 million random displacements and atom identity swapping steps. Illustrated in the right panel of Fig. 4.3 is a snapshot from the system at the end of the simulation where Pb impurities are seen to form clusters in the Al structure. In the figure Al and Pb atoms are shown in blue and red, respectively, and for clarity the Al atoms are made transparent. Al-Pb is an immiscible system with a large positive heat of mixing [6-8]. Therefore the system decreases its energy by forming Pb nanoclusters. A total of five clusters are formed. The two

largest clusters contain 17 and 13 atoms arranged in a close packed structure. The remaining clusters contain 2, 3 and 5 atoms. A histogram distribution showing the size of the Pb clusters for five different time frames clearly illustrates an increase in Pb cluster size with time (Fig. 4.4). These results are consistent with experimental imaging studies referenced above that show a strong tendency for forming Pb clusters in Al-Pb alloys.

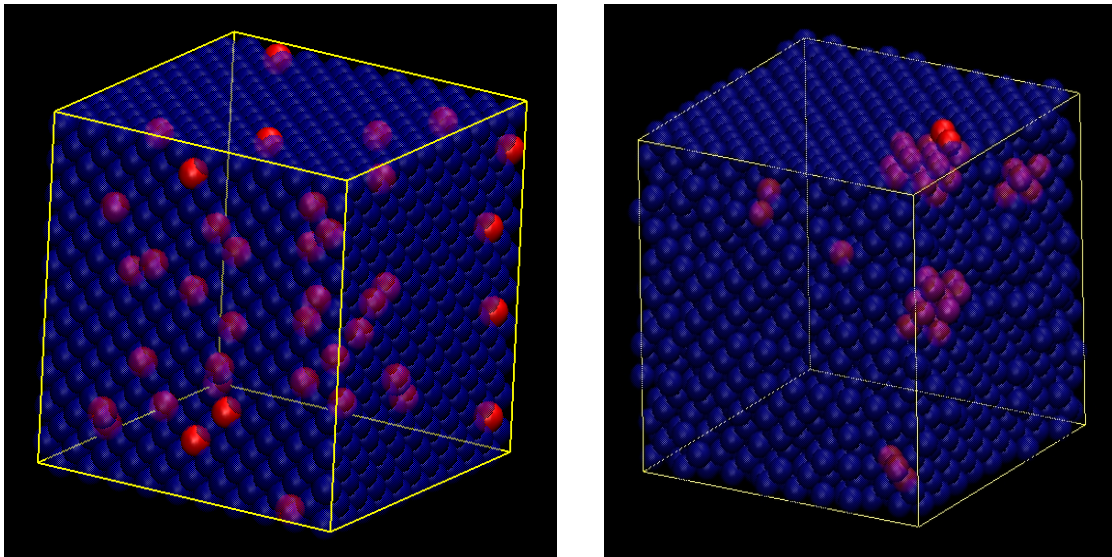


Fig. 4.3 Illustrations of the initial and simulated configurations for the bulk Al-Pb solid solution. Al and Pb atoms are shown in blue and red, respectively. (a) Initial configuration. (b) Final configuration after  $1.9 \times 10^6$  MC moves.

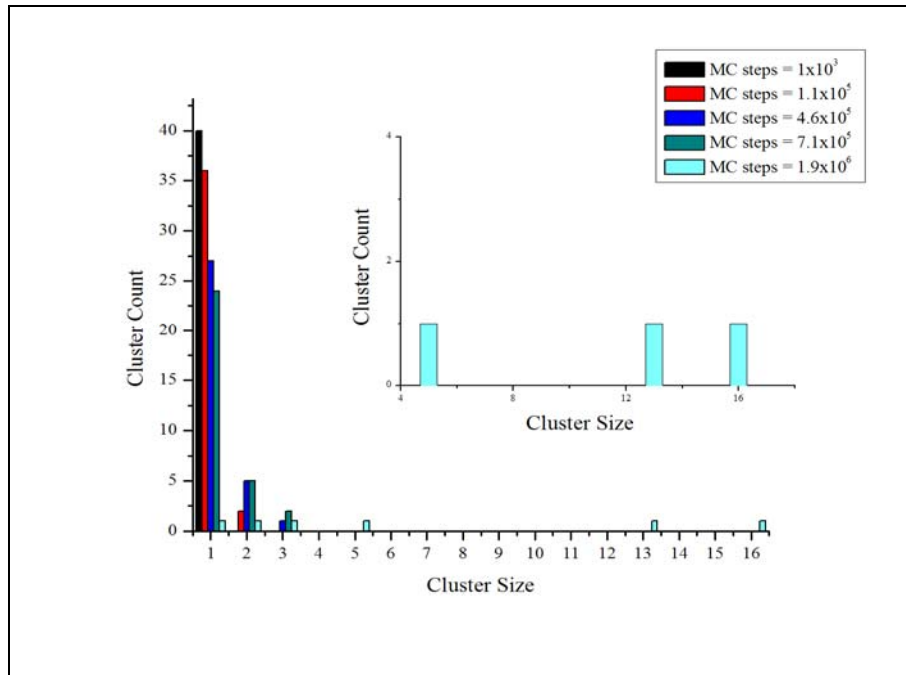


Fig. 4.4 Size distribution for Pb nanoclusters in bulk Al-Pb solid solution.

### 4.3.2 BICRYSTALLINE Al-Pb ALLOY

Illustrated in Figs. 4.6a and 4.6b are snapshots from the simulated bicrystal where one percent of the Al atoms are replaced with Pb atoms (Fig. 4.5) followed by a total of 2 million random displacements and atom identity swapping steps. The left panel (Fig. 4.6) illustrates the entire system, while the right panel illustrates close up views of the two grain boundaries. In the figures Al and Pb atoms are shown in blue and red respectively, and for clarity the Al atoms are made transparent. A majority of the Pb atoms have segregated to the grain boundaries and are well dispersed along the interfaces, with no significant clustering. This

result is consistent with the Z-contrast TEM image presented by Rajulapati *et al.* [1], which indicate Pb atoms along the grain boundaries in a nanocrystalline Al-Pb alloy.

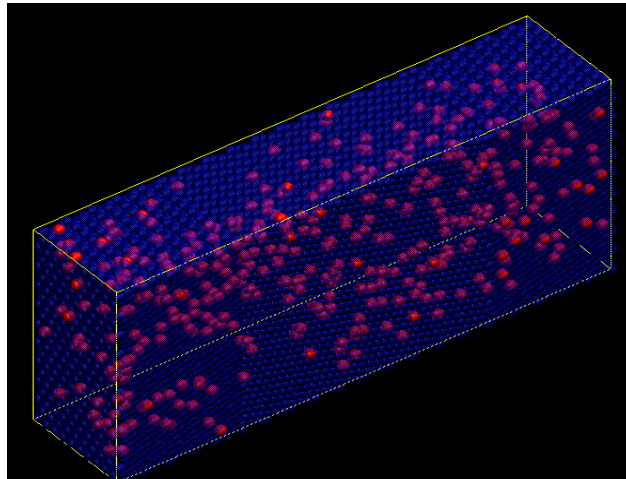


Fig 4.5 Initial configuration for an Al bicrystal, where one percent of the Al atoms are replaced with Pb atoms.

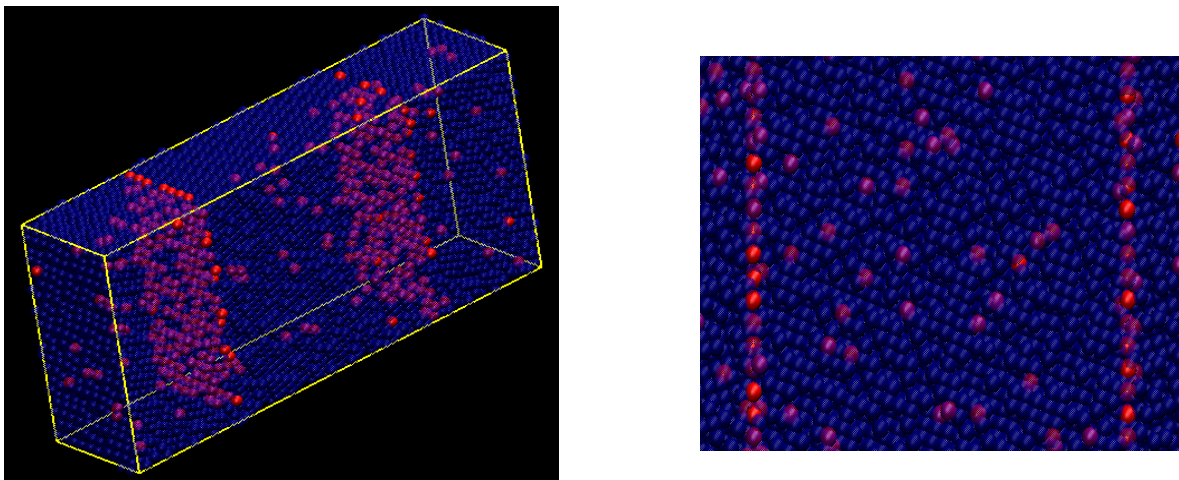


Fig. 4.6 Illustration of the final configuration after  $2 \times 10^6$  MC moves for the system with 1 atomic percent Pb impurities. Al and Pb atoms are shown in blue and red, respectively. (a) Entire system. (b) Close-up view.

To characterize the origin of the grain boundary segregation, the hydrostatic stress and segregation energy associated with each of the atomic sites listed in Fig. 4.1b was calculated (Table 4.1). The percent of each type of atomic site that is occupied by Pb at the end of the simulation is also given in Table 4.1. The segregation energy is taken as the difference in total energy for placing an impurity Pb atom at a bulk site relative to placing it in a grain boundary site. Pb atoms were found to segregate preferentially to site 1, followed by site 3, with no Pb atoms found at sites 2 or 4. This result is consistent with the segregation energies, as expected. In addition, there is a correlation between the stress state of the Al atoms in the pure structure and the probability of that site being occupied by Pb. Sites in the Al lattice under high tensile stress correspond to the most stable segregation energies, consistent with the large size of Pb atoms compared to Al.

Table 4.1 Atomic segregation energies and hydrostatic stresses for atoms around the  $\Sigma 5$  {210} Al grain boundary. The segregation energies and hydrostatic stresses are in units of eV/atom and GPa, respectively. -ve Tensile stress, +ve Compressive stress.

Atomic Position	Fraction Occupied	Segregation Energy	Hydrostatic Stress
1	0.68	1.16	-8.97
22'	0	0.28	4.49
33'	0.07	0.64	-3.20
44'	0	0.28	0.64

To further characterize cluster formation, an additional Monte Carlo simulation was carried out for a system where five percent of the Al atoms were replaced with Pb atoms. The final configurations at five atomic percent Pb substitution after 5.5 million moves is illustrated Fig. 4.7a. The initiation of clusters in the bulk as well as clusters that form out from the grain boundary is seen in the atomic configurations. Fig. 4.7b is a close up view of the two grain boundaries. These results from one and five atomic percent Pb substitution suggest dispersion of Pb impurities along the grain boundaries prior to cluster formation. This result is consistent both with the model proposed by Rajulapati *et al.* [1] to explain the decrease in hardness with increasing Pb content, as well as other reported images of Pb clusters at grain boundaries [2-3].

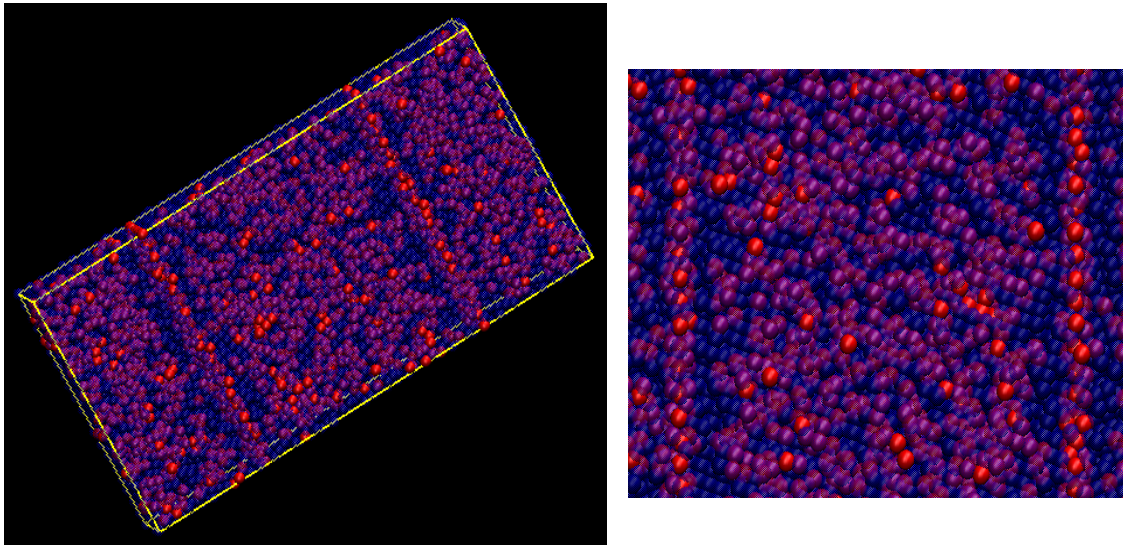


Fig. 4.7 Illustration of the final configuration after  $5.5 \times 10^6$  MC moves for the system with 5 atomic percent Pb impurities. Al and Pb atoms are shown in blue and red, respectively. (a) Entire system. (b) Close-up view.

### 4.3.3 NANOCRYSTALLINE Al-Pb ALLOY

To study Pb segregation in a nanostructured solid, an Al structure was created as described above in Section 4.2. The simulation was performed in a system box containing 39305 atoms. A total of 1% of the Al atoms were replaced with Pb atoms and a total of 2 million random displacements and atom identity swapping moves were then carried out. The resulting structure is illustrated in Fig. 4.8, where the Al atoms are transparent for clarity. As with the bicrystal, the Pb atoms segregate to the grain boundaries throughout the system. In addition, the Pb atoms tend to cluster around the triple junctions in the structure. Given in Fig. 4.9 is the cluster size distribution for segregated Pb atoms for different MC frames. From the figure an increase in Pb cluster size with time is evident.

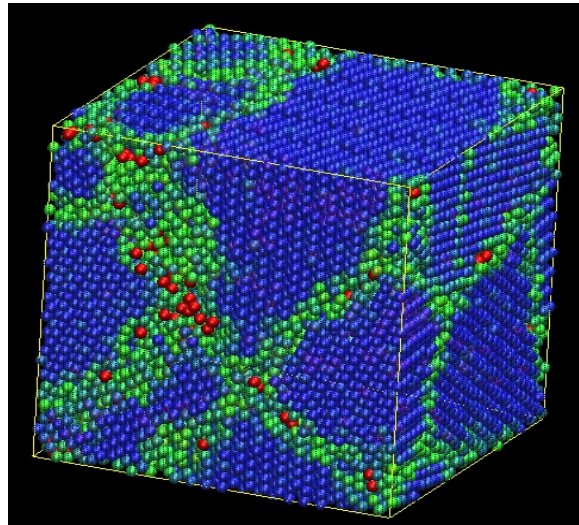


Fig. 4.8 Illustrations of the final configuration (after  $2 \times 10^6$  MC moves) for the nanocrystalline Al-Pb alloy. Al is shown in blue, and Pb and grain boundary atoms are shown in red and green respectively.

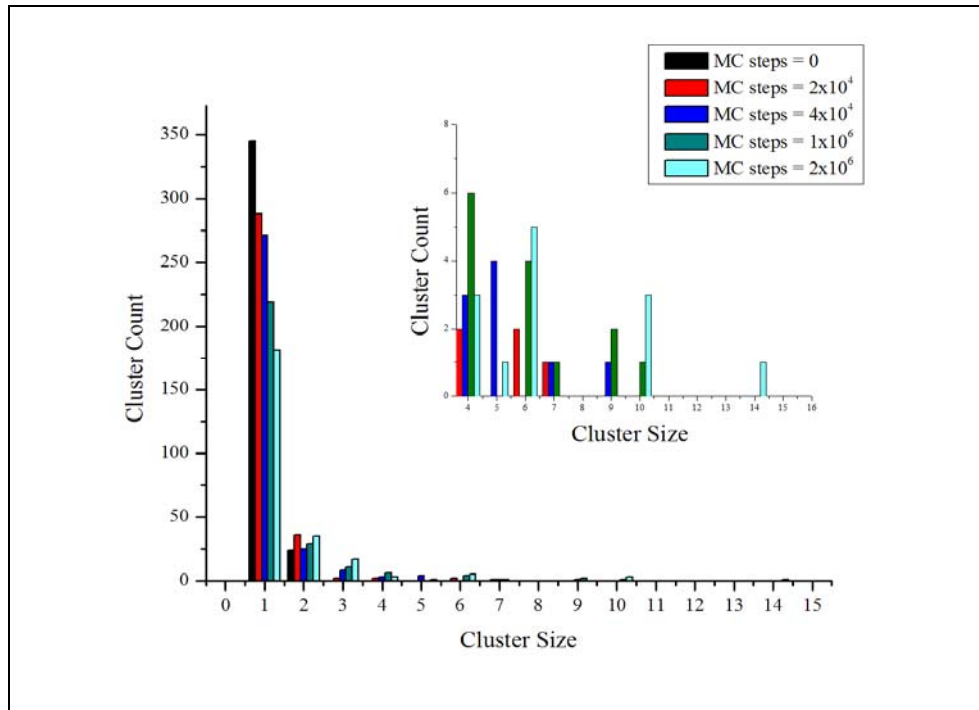


Fig. 4.9 Pb cluster distribution in nanocrystalline Al-Pb alloy.

#### 4.4 STABILIZATION ENERGIES

As discussed in Section 1.1.3.1, because Pb is immiscible in solid Al, Pb impurities could help thermodynamically stabilize nanostructured Al against grain growth [9-10]. To explore this possibility, enthalpies at 0K were calculated for several structures associated with the bicrystalline Al-Pb alloys using the MEAM potential. The results are summarized in Table 4.2. For consistency, all of the enthalpies are referenced to the cohesive energies given by the MEAM. The enthalpy values  $E^{\text{en}}$  are given by

$$E^{en} = E^{Al_{N_{Al}}Pb_{N_{Pb}}} - N^{Al} \times E_{coh}^{Al} - N^{Pb} \times E_{coh}^{Pb} \quad (1)$$

where  $N^{Al}$  and  $N^{Pb}$  are the number of Al and Pb atoms, respectively, in a given system.

$E^{Al_{N_{Al}}Pb_{N_{Pb}}}$  is the potential energy of the system given by the MEAM, and  $E_{coh}^{Al}$  and  $E_{coh}^{Pb}$  are the cohesive energies for the ideal Al and Pb lattices, respectively, also given by the MEAM.

The enthalpy associated with one Pb atom in an Al lattice is positive, which is consistent with the immiscibility of Pb in Al. Listed in Table 4.3 for the bicrystal are relative enthalpy values for several percentages of the sites with the most stable segregation energies filled (site 1 in Fig. 4.1b). The relative enthalpy values are calculated as:

$$\frac{\left(E_{GB(N^{Pb})}^{en} - E_{GB}^{en}\right)}{N^{Pb}} \quad (2)$$

where,  $E_{GB(N^{Pb})}^{en}$  is the enthalpy of the grain boundary with  $N^{Pb}$ , Pb atoms substituted for Al at the grain boundary, and  $E_{GB}^{en}$  is the enthalpy of the pure grain boundary. The enthalpy of pure bulk Al from Eq. (1) is zero; therefore the relative enthalpy of 1 Pb in bulk Al is equal to the enthalpy of the structure where 1 Pb was substituted for Al in the bulk.

Although the enthalpies are all positive with respect to the ideal bulk Al and Pb, the grain boundary (with Pb) has a lower relative enthalpy than that for the relative enthalpy of 1 Pb in

bulk Al, i.e. the ideal solid solution. Hence while the grain boundaries are not globally stable, they are metastable with respect to the thermodynamic limit of an infinitely dilute solution. This suggests that non-equilibrium processing such as ball milling could create a meta-stable structure in which dispersed Pb helps to stabilize the nanostructure against grain growth. This is a prediction that is left to experiment to verify.

Table 4.2 Enthalpies of several Al-Pb structures.

$$E_{coh}^{Al} \text{ (eV/atom)} = -3.349, E_{coh}^{Pb} \text{ (eV/atom)} = -2.04$$

System	N <sup>Al</sup>	N <sup>Pb</sup>	E <sup>en</sup> (eV)
One Pb in bulk Al	39999	1	1.622694
Pure Bicrystal	40000	0	251.595595
Bicrystal with one preferred site (at grain boundary) occupied by Pb	39999	1	251.654297
Bicrystal with half of the preferred sites (at grain boundary) occupied by Pb	39800	200	356.608290
Bicrystal with all of the preferred site (at grain boundary) occupied by Pb	39600	400	403.473092

Table 4.3 Relative enthalpies of several bicrystalline Al-Pb structures. Relative enthalpy of 1 Pb in bulk Al = 1.622 eV/atom.

Structure	Relative Enthalpy eV/atom
Grain Boundary with one preferred site occupied by Pb	0.059
Grain Boundary with half of the preferred sites occupied by Pb	0.525
Grain Boundary with all of the preferred sites occupied by Pb	0.379

## 4.5 EFFECT OF Pb ON MECHANICAL BEHAVIOR OF Al

### 4.5.1 INTRODUCTION

Based on several experimental studies the effect of Pb on the mechanical behavior of nanocrystalline Al is conflicting. In one case hardening was observed [11], while in the other there was a dramatic softening effect [12]. The reasons for these differences are not understood, but appear to be related to Pb segregation to grain boundaries, as observed by the latter investigators using Z-contrast high resolution transmission electron microscopy (HRTEM).

In an attempt to study the effect of Pb on the mechanical behavior of Al, in particular to investigate if the addition of Pb is increasing or decreasing the strength of Al, molecular dynamics simulations have been used to model uniaxial straining of Al bicrystal containing

two  $\Sigma 5 \{210\}$  tilt boundaries, with and without Pb substitution at the grain boundaries. The initial results from the simulations that support the findings of Rajulpati *et al.* [12] are presented. To better understand the underlying atomic mechanisms causing the softening, an extensive follow-up work is needed to fully understand the evolution of the interface structures during the deformation process.

#### **4.5.2 METHODOLOGY**

The Al bicrystal containing the  $\Sigma 5 \{210\}$  tilt interface was developed using GB studio. The  $\Sigma 5 \{210\}$  structure is a high symmetry grain boundary that has a high density of coincident sites across the interface plane. The system contains 80000 atoms and periodic boundary conditions were adopted in all three directions. The use of periodic boundary conditions in the z-direction introduces a second interface into the model. The box sizes in the x, y and z directions are 8.1 nm, 9.1 nm and 18.1 nm, respectively. To create alloys, a total of 1 and 8 atomic percent of Al atoms at the two grain boundaries were replaced by Pb atoms. For 1 atomic percent Pb substitution all of the coincident sites along the plane of atoms at the two grain boundaries were converted to Pb. For 8 atomic percent Pb substitution, along with the coincident sites other Al sites that were close to the two grain boundaries were converted to Pb. Molecular dynamics simulation to deform Al and Al-Pb bicrystal configurations using a Glue-type interatomic potential [13-14] were then carried out.

The interface models were initially equilibrated in an NPT ensemble to a pressure of 0 bar and a temperature of 300 K. Upon completion of the equilibration process, molecular dynamics simulations in uniaxial tension were used to deform the Al and Al-Pb interface models. For that the periodic cells were extended with a constant strain rate of  $1 \times 10^9 \text{ s}^{-1}$  along, the z direction, while the size of the other two periodic boundaries were controlled via the imbalance between the system stresses and the desired value. The goal was to keep the motion of the boundaries transverse to the loading direction stress free.

### **4.5.3 RESULTS AND DISCUSSION**

The stress-strain curves for pure, 1 atomic percent and 8 atomic percent Pb doped Al are shown in Fig. 4.10. From the figure it is apparent that addition of Pb to Al grain boundaries causes a softening of Al. The result supports the hypothesis that Pb segregation to Al grain boundaries causes a drop in hardness as observed by Rajulapati *et al.* [12]. The Young's modulus (E) as calculated from the curves for the pure Al and Al-Pb with 1 and 8 atomic percent Pb are 55 GPa, 50 GPa and 42 GPa respectively. (The E values are in the range of 42-55 GPa compared to the experimental value of  $E \sim 70$  GPa for polycrystalline Al). As the Pb content increases, the E values decrease. For the experimental results reported in [12], the hardness decreases by  $\sim 37\%$  for 28 nm grain size Al-Pb alloy with 1 atomic percent addition of Pb. The simulations do not account for the large strength decrease observed in these experiments, and they cannot capture the macroscopic size scales and low strain rates in the

latter, but they do indicate the onset of a softening effect as a result of Pb segregation to the grain boundaries.

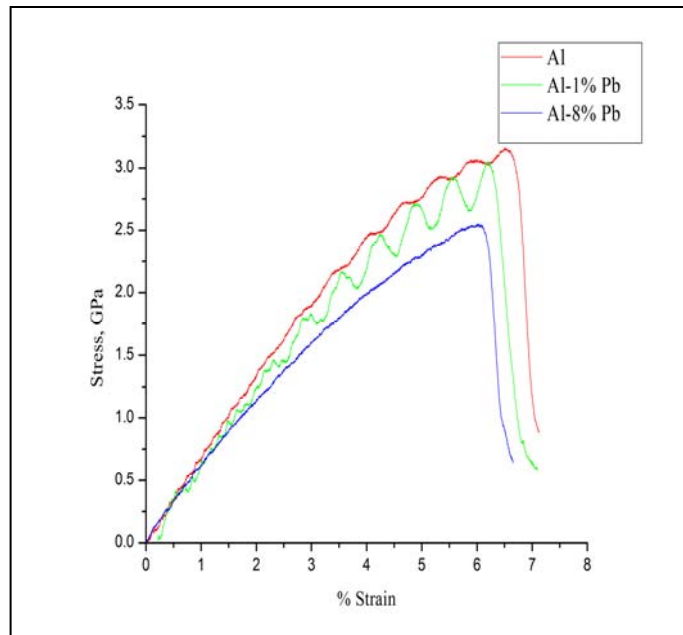


Fig. 4.10 Stress-strain curves for pure Al and Al-Pb alloys with 1 and 8 atomic percent Pb on Al grain boundaries.

Figs. 4.11-4.13, illustrate the uniaxial tensile deformation of the  $\Sigma 5 \{210\}$  interface model in pure and Pb doped (1 and 8 atomic percent Pb) aluminum at 300 K. The generation of stacking faults suggesting nucleation of partial dislocations from the grain boundaries is shown in these structures. In Figs. 4.11-4.13 the atoms are colored according to the centrosymmetry parameter [15], which is a scalar quantity designed to identify defects such

as interfaces and stacking faults. In all of the images in Figs. 4.11-4.13 atoms with a centrosymmetry parameter close to zero are removed to facilitate viewing of the defect structures.

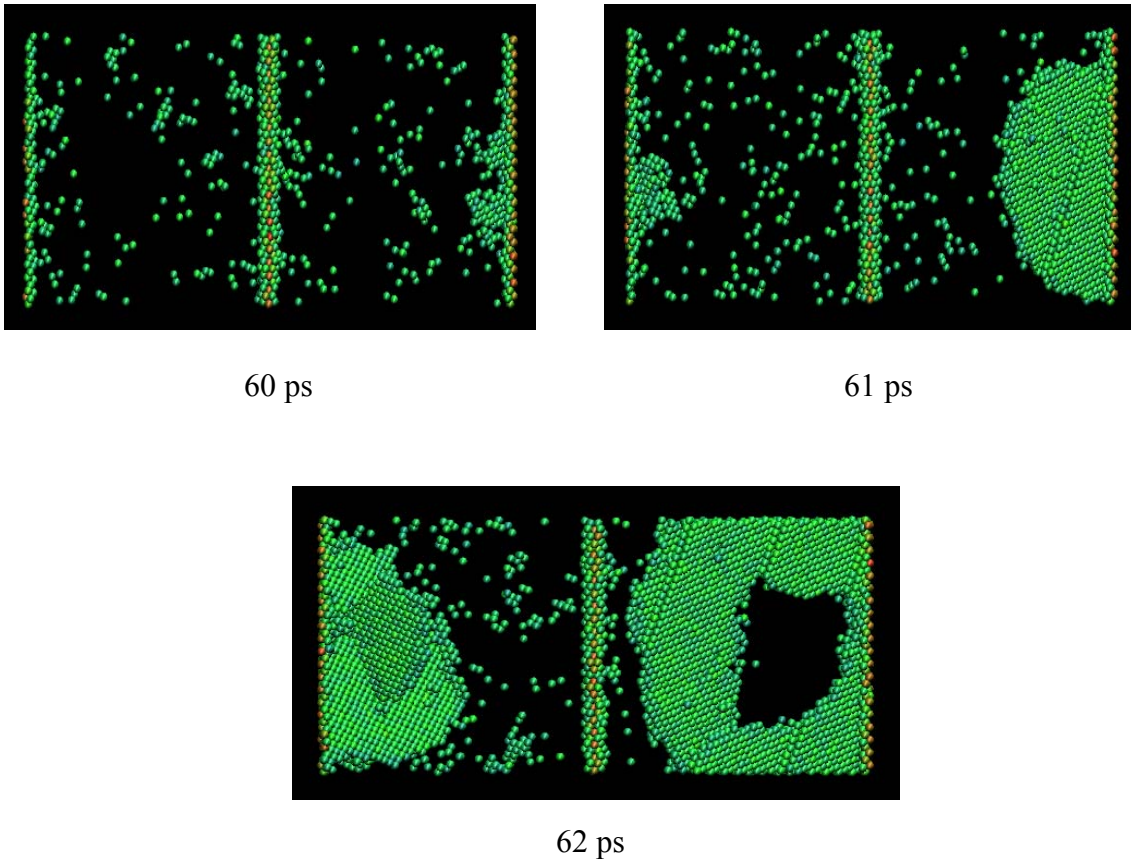
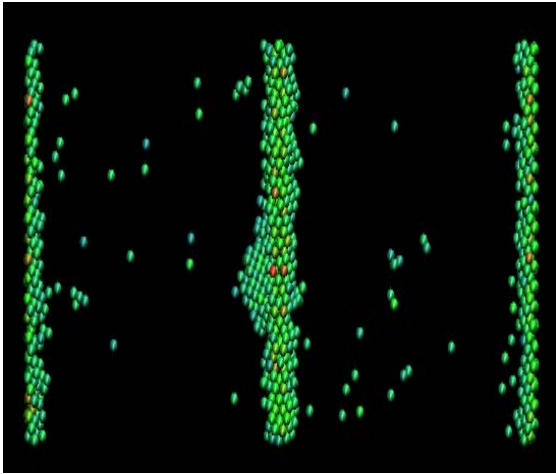
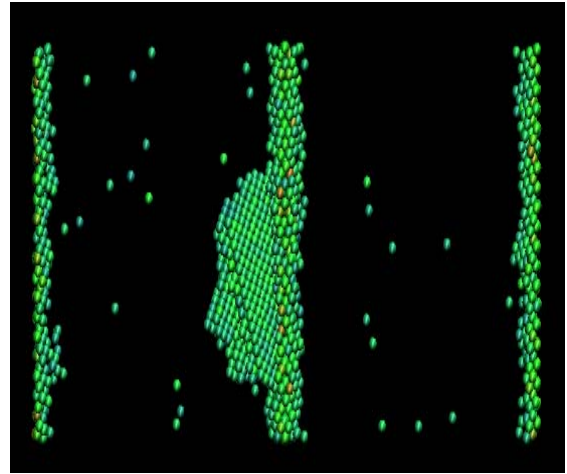


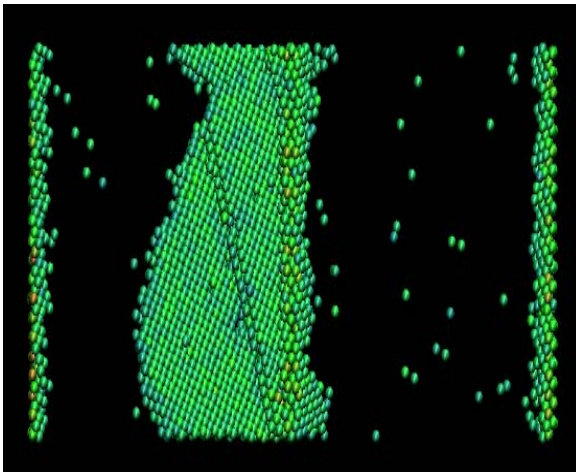
Fig. 4.11 Deformation structures for pure Al at 60, 61 and 62 ps.



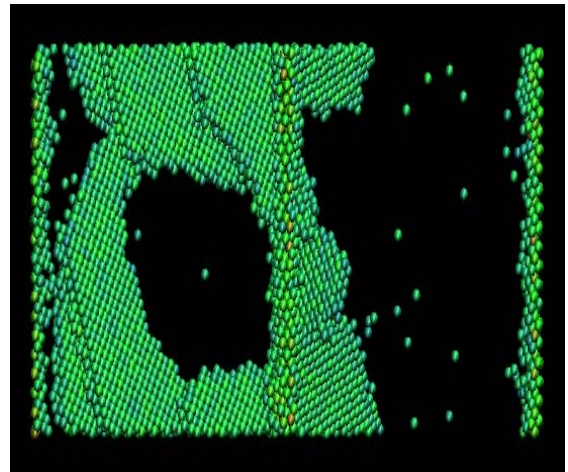
56 ps



57 ps

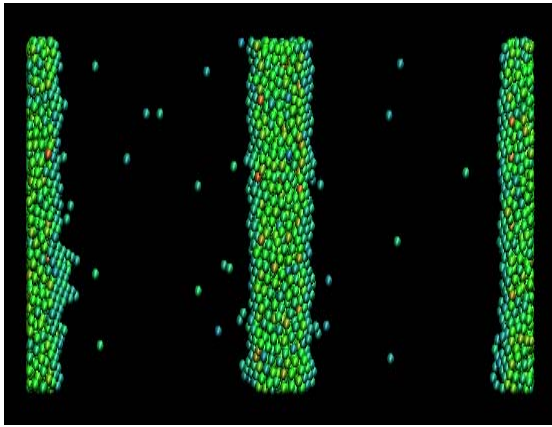


58 ps

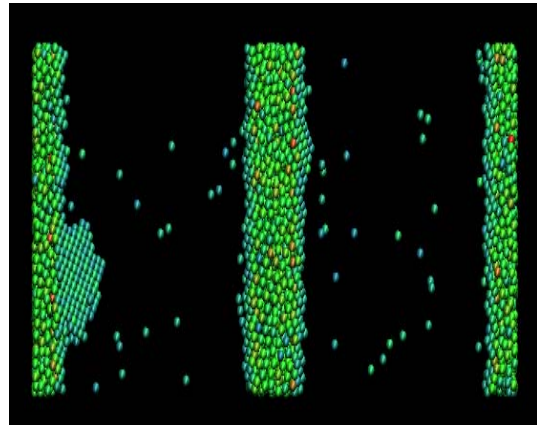


59 ps

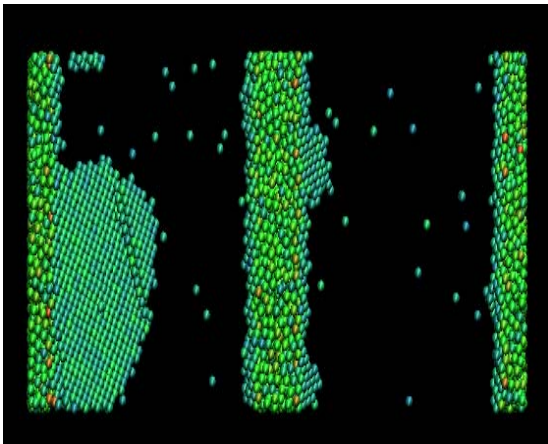
Fig. 4.12 Deformation structures for 1 atomic percent Pb doped Al at 56, 57, 58 and 59 ps.



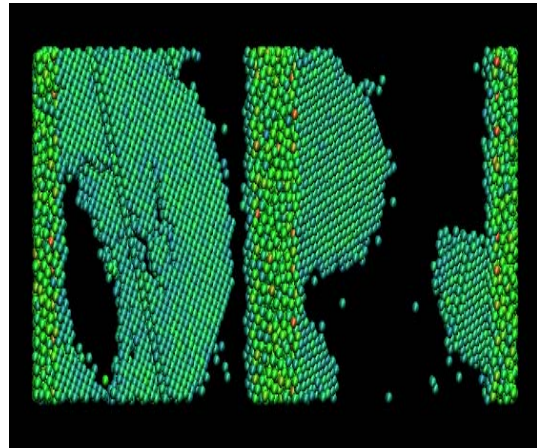
58 ps



59 ps



60 ps



61 ps

Fig. 4.13 Deformation structures for 8 atomic percent Pb doped Al at 58, 59, 60 and 61 ps.

The tensile stress required to nucleate the first partial dislocation at 300 K from the  $\Sigma 5$  {210} pure and Pb doped Al boundary is calculated as 3.0 Gpa (Pure Al), 2.8 Gpa (1 atomic percent Pb) and 2.5 Gpa (8 atomic percent Pb) respectively. In pure Al the first dislocation is nucleated at 60 ps. In Pb doped Al they are nucleated at 56 ps for 1 atomic percent doped Al and 58 ps for 8 atomic percent doped Al. The results show that compared to Al the addition of Pb facilitates the formation of dislocations at the grain boundaries for both the 1 atomic percent and 8 atomic percent Pb doping. But it suppresses generation of dislocations with an increase in the amount of Pb on the grain boundaries.

An increase in the overall thickness and disorder at the grain boundaries with Pb addition is also observed. Increasing disorder is seen in Figs. 4.12 and 4.13, where the grain boundaries appear thicker compared to the pure Al grain boundary structure in Fig. 4.11. The thickening and disordering of the grain boundaries is believed to be contributing to this softening.

## REFERENCES

1. K. V. Rajulapati, R. O. Scattergood, K. L. Murty, G. Duscher, C. C. Koch, *Scripta Mater.*, 55 (2006) 155.
2. E. Johnson, A. Johansen, U. Dahmen, S. Chen, T. Fujii, *Mater. Sci. Eng. A*, 304–306 (2001) 187.
3. E. Johnson, A. Johnson, S. Hinderberger, S. -Q. Xiao, U. Dahmen, *Interface Science*, 3 (1996) 279.

4. A. Okabe, B. Boots, K. Sugihara, S. N. Chiu. Spatial Tessellations: Concepts and Applications of Voronoi Diagrams – 2<sup>nd</sup> edition (2000).
5. N. Metropolis, A. W. Rosenbluth, M. N. Rosenbluth, A. H. Teller, E. Teller, J. Chem. Phys., 21 (1953) 1087.
6. Phase diagrams for binary alloys, edited by Hiroaki Okamoto (2000), ISBN 0871706822.
7. T. Massalski. Binary alloy phase diagrams, (1990) Materials Park, OH: ASM International.
8. Metals handbook - 8th edition, 8 (1973) 263, American Society for metals, Metals Park, Ohio.
9. J. Weissmüller, W. K. Krauss, T. Haubold, R. Birringer, H. Gleiter, Nanostruct. Mater. 1 (1992) 439.
10. J. Weissmüller, Nanostruct. Mater. 3 (1993) 261.
11. H. W. Sheng, F. Zhou, Z. Q. Hu, K. Lu, J. Mater. Res., 13 (1998) 308.
12. K. Rajulapati, R. O. Scattergood, K. L. Murty, G. Duscher, C. C. Koch, Scripta Mater., 55 (2006) 155.
13. F. Ercolessi, M. Parrinello, E. Tosatti, Philo. Mag., 58(1) (1988) 213.
14. A. Landa, P. Wynblatt, D. J. Siegel, J. B. Adams, O. N. Mryasov, X.-Y. Liu, Acta mater, 48 (2000) 1753.
15. C. L. Kelchner, S. J. Plimpton, Phys. Rev. B., 58 (1998) 11085.

## CHAPTER 5

### PREDICTION OF ENERGIES OF TWO HIGH SYMMETRY $\Sigma 5$ $\langle 100 \rangle$ TILT GRAIN BOUNDARIES IN Al-Pb ALLOYS USING ATOMISTIC MEAM AND FIRST PRINCIPLES DENSITY FUNCTIONAL CALCULATIONS

#### 5.1 INTRODUCTION

In this chapter the stabilizing effect of Pb impurities on the energies of Al grain boundaries, as a function of Pb content, using atomistic MEAM and first principles methods has been investigated. The grain boundary energies as a function of Pb content were investigated for two high symmetry -  $\Sigma 5$   $\{210\}$  and  $\Sigma 5$   $\{310\}$  Al tilt grain boundaries. Results from both of these methods show a reduction in grain boundary energy with an increase in Pb content.

Compared to a single crystal, the presence of grain boundaries contributes an excess energy to the Gibbs free energy of a polycrystal. This excess Gibbs free energy (G) can be expressed as a product of the specific grain boundary energy,  $E_{GB}$ , with the total area, A, of the grain boundaries. The reduction of the excess Gibbs free energy by a reduction in grain boundary area contributes to the grain growth of polycrystals. This reasoning assumes  $E_{GB}$  to be always a positive quantity. Nevertheless, if  $E_{GB}$  can be reduced to zero, G is no longer dependent on A. The interactions of the alloy atoms with the grain boundaries determine the

thermal stability of nanocrystalline alloys. One important aspect of this interaction is the reduction of the grain boundary specific energy by grain boundary segregation, which can be described by the Gibbs adsorption equation [1]

$$dE_{GB} = -\Gamma_{solute} d\mu_{solute} \quad (1)$$

where  $\Gamma_{solute}$  is the interfacial excess of solute atoms and  $\mu_{solute}$  is the chemical potential of the solute component. In Eq. (1) a positive  $\Gamma_{solute}$  will lower  $E_{GB}$ ; however, there is no indication for the possibility of  $E_{GB} < 0$ . This leads to speculation that a state of metastability could be achieved in nanocrystalline alloys with a certain solute concentration so that the total free energy of the nanocrystal is below that of the solid solution single crystal.

Weissmüller and co-workers [2–4] have suggested that it is possible for nano-crystalline metallic alloys to be metastable, i.e. no tendency for grain growth, if  $E_{GB}$  can be reduced to zero or negative values. Ignoring entropic effects, the variance of the  $E_{GB}$  with  $E_{seg}$  (heat of segregation) is given by

$$E_{GB} = E_{GB(0)} - \{X_{solute}\} E_{seg} \quad (2)$$

where  $E_{GB(0)}$  is the specific excess free energy of a pure solvent and  $\{X_{solute}\}$  is the specific dopant coverage on the grain boundary. If  $E_{GB} \leq 0$ , due to a large and positive  $E_{seg}$  and /or  $\{X_{solute}\}$ , the total Gibbs free energy of a nanocrystal would be equal to or below that of the single crystal solid solution and the driving force for grain growth is eliminated.

The experimental verification of the grain growth metastability theory was performed in the alloy systems of Pd-Zr [5] and Y-Fe [2] both of which have a high enthalpy of segregation and where grain growth was suppressed upon increasing the solute concentrations. Millett and co-workers, using MD simulations, studied the energy of a  $\Sigma 7$  symmetric tilt grain boundary in a Cu bicrystal by adding impurity atoms of various characteristics and concentrations to the grain boundary [6]. Although it was a parametric study, it helped provide insights into the types and concentrations of solute atoms capable of substantially reducing grain boundary energy.

As recently pointed out by Kirchheim [7], the precipitation of solute atoms can be an alternative to grain boundary segregation and in many cases is the thermodynamic equilibrium state. For nanocrystalline Ni-P alloys [8], rapid grain growth accompanies the precipitation of the  $Ni_3P$  phase because no longer do the P-atoms lower  $E_{GB}$ . Therefore, solute atoms must be kinetically hindered from forming precipitates in order for a metastable nano-crystalline alloy system with zero  $E_{GB}$  to exist.

Al-Pb is an immiscible system with a positive heat of segregation [9-11]. Therefore the Al-Pb is a potential candidate for such study. Our Monte Carlo simulations have predicted that Pb atoms segregate to the grain boundaries in a bicrystalline and a nanocrystalline structure (Chapter 4). The goal therefore is to explore if Pb impurities can sufficiently stabilize grain boundaries so that nanostructured Al can be stabilized against grain growth. We have investigated the effect of Pb impurities on the energies of grain boundaries in two bicrystalline structures containing  $\Sigma 5 \{210\}$  and  $\Sigma 5 \{310\}$  grain boundaries. Analyses of grain boundary energies for varying concentrations of Pb suggests that grain boundaries in Al can be thermodynamically stabilized by Pb impurities with respect to a dilute solid solution of Pb in Al. A newly developed MEAM interatomic potential was used for calculating grain boundary energies.

## 5.2 METHODOLOGY

Illustrated in Figs. 5.1 and 5.2 are the bicrystalline structures used in the MEAM calculations for the  $\Sigma 5 \{210\}$  and the  $\Sigma 5 \{310\}$  grain boundaries. The systems contain 40000 and 25344 atoms, respectively, and periodic boundary conditions were applied in all three directions. Due to the periodicity the structures contain two-grain boundaries perpendicular to the z direction. The box sizes, in the three directions (x, y and z), for the structures with  $\Sigma 5 \langle 100 \rangle \{210\}$  and  $\Sigma 5 \langle 100 \rangle \{310\}$  configurations are 4.05 nm, 9.05 nm, 18.11 nm and 3.24 nm, 10.245 nm, 12.807 nm, respectively. Schematics of atomic sites at the  $\Sigma 5 \{210\}$  and  $\Sigma 5 \{310\}$  tilt grain boundaries are also shown in Figs 5.1 and 5.2, where site 1 corresponds to a

coincident site. There are two atomic planes along the  $\langle 100 \rangle$  direction. The open and closed circles represent atoms distributed on the first and second  $\{100\}$  planes, respectively.

To create alloys the Al atoms at 12.5, 25, 50, 75 and 100 percentages of the coincident sites along the plane of atoms at the two grain boundaries were replaced with Pb atoms. For a consideration of the symmetry, the structures with grain boundaries were doped with the impurity atoms partitioned equally to the two grain boundary planes. In the structures the lattice sites correspond to an Al face-centered cubic lattice. Atomic positions are initially relaxed using a molecular dynamics energy minimization technique. To accommodate the large volume of Pb compared to Al, the volume of the computational cell was also adjusted at regular intervals in between atomic position relaxation steps.

The grain boundary energies for the undoped system were taken as the difference in the total energy of the structure containing two grain boundaries,  $E(AL_i)^{2GB}$ , and an equivalent structure for bulk Al,  $E(AL_i)^{Bulk}$ , divided by the total area ( $A_{GB} = 2 \times x \times y$ ) of the two grain boundaries.

$$\left( \frac{E(AL_i)^{2GB} - E(AL_i)^{Bulk}}{A_{GB}} \right) \quad (3)$$

Similarly the grain boundary energy for the Pb doped system was evaluated as,

$$\left( \frac{E(Al_i Pb_j)^{2GB} - E(Al_i Pb_j)^{Bulk}}{A_{GB}} \right) \quad (4)$$

where  $i, j$  are the number of Al and Pb atoms and  $E(Al_i Pb_j)^{2GB}$  and  $E(Al_i Pb_j)^{Bulk}$  are the total energies of the substitutional-impurity-doped structures of grain boundaries and bulk, respectively. The grain boundary energies,  $E_{GB}$ , for a number of structures, with varying percentages of the coincident sites occupied by Pb atoms were thus calculated.

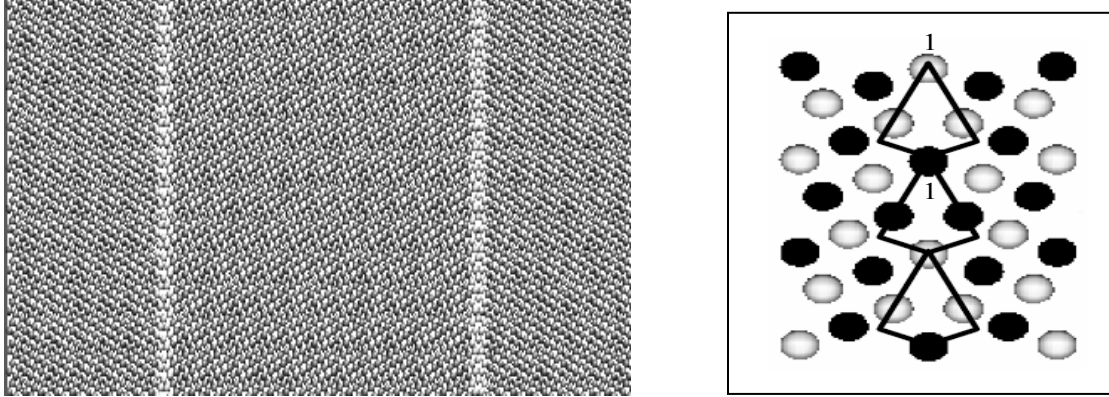


Fig. 5.1 (a) Illustration of an Al bicrystalline geometry containing two  $\Sigma 5 \langle 100 \rangle \{210\}$  tilt grain boundaries. Bulk and GB atoms are shown in silver and white, respectively. (b) Schematic of the  $\Sigma 5 \langle 100 \rangle \{210\}$  tilt grain boundaries. The open and closed circles represent atoms on the  $\{100\}$  and  $\{200\}$  planes, respectively.

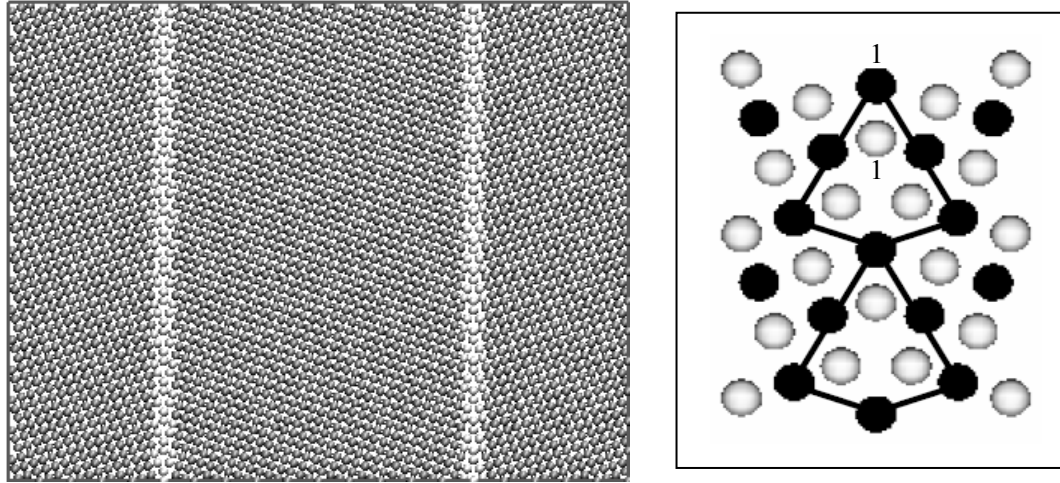


Fig. 5.2 (a) Illustration of an Al bicrystalline geometry containing two  $\Sigma 5 \langle 100 \rangle \{310\}$  tilt grain boundaries. Bulk and GB atoms are shown in silver and white, respectively. (b) Schematic of the  $\Sigma 5 \langle 100 \rangle \{310\}$  tilt grain boundaries. The open and closed circles represent atoms on the  $\{100\}$  and  $\{200\}$  planes, respectively.

### 5.3 MEAM RESULTS

The grain boundary energy,  $E_{GB}$ , as a function of the percentage of the coincident sites occupied by Pb atoms for the two grain boundaries -  $\Sigma 5 \{210\}$  and  $\Sigma 5 \{310\}$  are shown in Figs. 5.3 and 5.4 respectively.

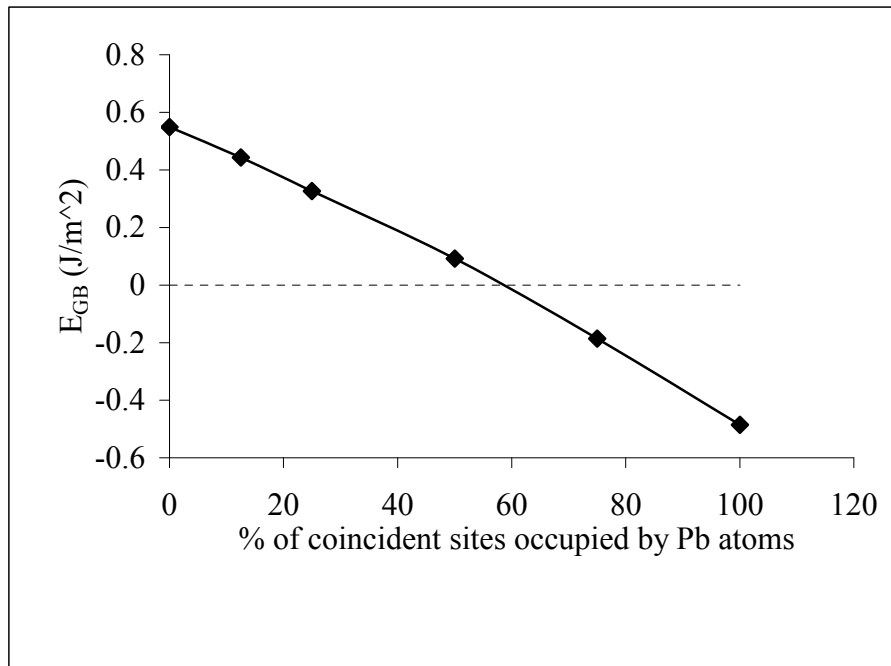


Fig. 5.3 Grain boundary energy as a function of the percentage of the coincident sites occupied by Pb atoms - ( $\Sigma 5 \{210\}$  grain boundary).

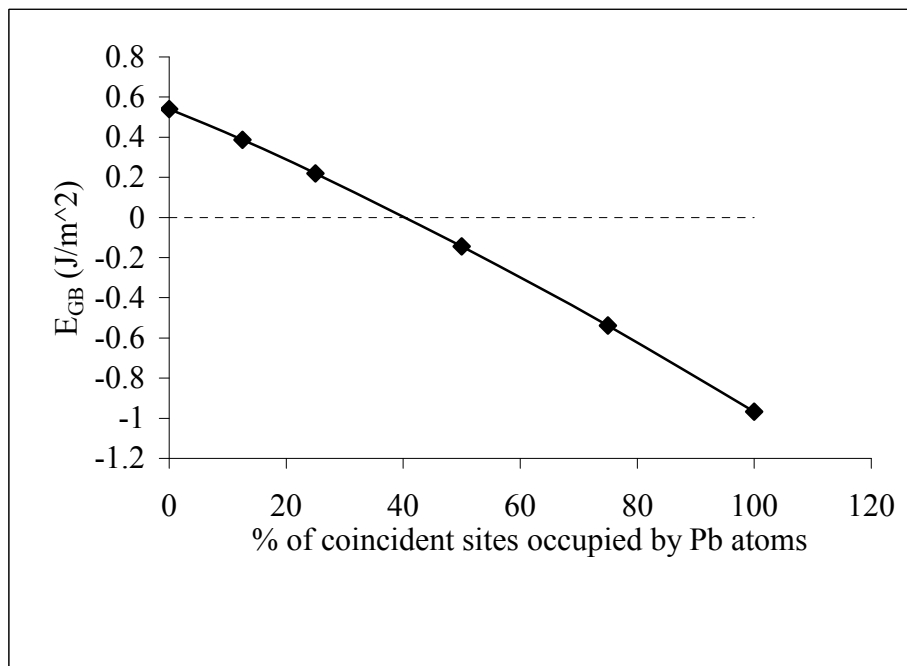


Fig. 5.4 Grain boundary energy as a function of the percentage of the coincident sites occupied by Pb atoms - ( $\Sigma 5 \{310\}$  grain boundary).

The calculations predict a reduction in the grain boundary energy with an increase in the number of Pb atoms on the grain boundary, with a negative energy with respect to a dilute solid solution predicted when more than 50 and 40 percent of the coincident sites were replaced by Pb atoms for the  $\Sigma 5 \{210\}$  and  $\Sigma 5 \{310\}$  grain boundaries, respectively. The creation of a metastable state decreases the grain boundary energy of the system to zero. In the Fig 5.3 and Fig. 5.4, the  $E_{GB}$  starts at the value corresponding to the energy of pure grain boundary structure i.e. structure with no Pb impurities. From the discussion presented in Section 5.1, the results obtained suggest that Pb impurities can indeed stabilize grains in Al against grain growth. The creation of a metastable state at predicted solute concentrations may help to stabilize Al structures against grain growth.

#### **5.4 FIRST PRINCIPLES RESULTS**

All material properties can be predicted using first principles calculations based solely on chemical composition i.e. if the number and type of species in a system being simulated are known. This paradigm contrasts with a semi-empirical approach like the MEAM used above where model parameters are adjusted to fit to some calculated properties of a calibrating system. The first principles calculations get around all such parameterization/model fitting problems and help make quantitatively accurate predictions. In Section 5.3 the energies of the two high symmetry  $\Sigma 5 \{210\}$  and  $\Sigma 5 \{310\}$  tilt grain boundaries as a function of Pb content using the MEAM potential were calculated. The energies of the same two grain boundaries, with and without Pb at the grain boundaries, as calculated using Density

Functional Theory are reported in this section. The calculated first principles energies confirm the stabilization of grain boundaries in Al due to Pb segregation with respect to an ideal solid solution as predicted by the MEAM calculations.

The Density Functional Theory [12-13] first principle calculations were carried out using the Vienna Ab-initio Simulation Package (VASP) [14-16]. It is a package for performing ab initio quantum mechanical molecular dynamics (MD) simulations using pseudopotentials and a plane wave basis set. The approach implemented in VASP is based on a finite-temperature local-density approximation (with the free energy as variational quantity) and an exact evaluation of the instantaneous electronic ground state at each MD-step using efficient matrix diagonalization schemes and an efficient Pulay mixing.

All calculations were carried out using Vanderbilt-type ultrasoft pseudopotentials [17-18] and the generalized gradient approximation (GGA) of Perdew and Wang [19]. A cut-off energy of 300 eV for the plane-wave basis was used in all the calculations. The Monkhorst-Pack method [20] was used to generate special K – points from a uniform mesh of 8x4x1 for the  $\Sigma 5 \{210\}$  grain boundary and 12x4x1 for the  $\Sigma 5 \{310\}$  grain boundaries respectively. The Methfessel-Paxton smearing method with 0.1-eV smearing width was used.

Illustrated in Fig. 5.5 are the supercell structures used in the DFT calculations with and without Pb for the  $\Sigma 5 \{210\}$  structure (top views) and the  $\Sigma 5 \{310\}$  structure (bottom views). The systems contain 160 and 156 atoms, respectively, and periodic boundary conditions were

applied in all three directions. Due to the periodicity the structures contain two-grain boundaries perpendicular to z direction. The supercell dimensions, in the three directions (x, y and z), for the structures with  $\Sigma 5 \langle 100 \rangle \{210\}$  and  $\Sigma 5 \langle 100 \rangle \{310\}$  configurations are  $4.05 \text{ \AA}$ ,  $18.1122 \text{ \AA}$ ,  $36.2242 \text{ \AA}$  and  $4.05 \text{ \AA}$ ,  $12.8072 \text{ \AA}$ ,  $51.229 \text{ \AA}$  respectively. To create an alloy the Al atoms at one half of the coincident sites along the plane of atoms at the two grain boundaries were replaced with Pb atoms. Prior modeling using the MEAM suggests that these are the most stable substitutional sites. For a consideration of the symmetry, the supercell with grain boundaries is doped with impurity atoms partitioned equally to the two grain boundaries planes. The MEAM calculations (for the values reported in Table 1) used supercells that are a factor of four and two larger in the x and y directions (compared to supercells used for DFT), respectively. The distance between the two grain boundaries is the same as that used for the DFT calculations.

For the DFT calculations all of the atoms are initially relaxed using a combination of conjugate gradient and quasi-Newton techniques to an energy tolerance of 1 meV/atom with the lattice constant kept fixed at the experimental value of 0.405nm. The energy is then further minimized with respect to the three cell dimensions. A minimization scheme as given in Section 5.2 is used for the MEAM calculations. The grain boundary energies for the undoped and Pb doped Al system is calculated using the same procedure as given for the MEAM calculations above in Section 5.2. The energies for the bulk system were calculated using the same cut-off and with equivalent k-point sampling as that for systems with grain boundaries. The x, y and z supercell dimensions for the bulk structures corresponding to  $\Sigma 5$

$\langle 100 \rangle \{210\}$  and  $\Sigma 5 \langle 100 \rangle \{310\}$  grain boundaries are  $4.05 \text{ \AA}$ ,  $16.2 \text{ \AA}$ ,  $40.5 \text{ \AA}$  and  $4.05 \text{ \AA}$ ,  $12.15 \text{ \AA}$ ,  $52.65 \text{ \AA}$  respectively.

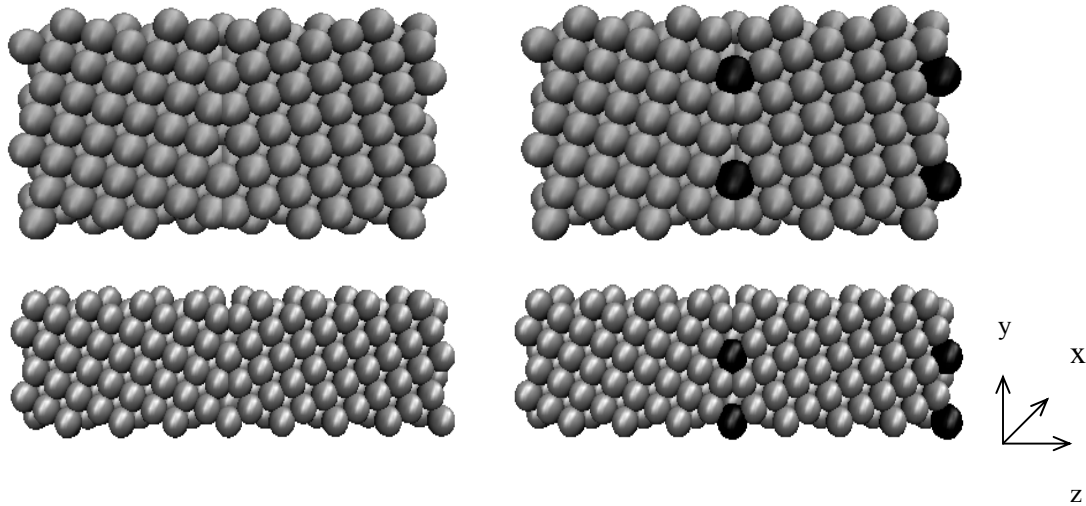


Fig. 5.5 Illustrations of the  $\Sigma 5 \{210\}$  structure (top views) and the  $\Sigma 5 \{310\}$  structure (bottom views) without (left views) and with Pb (right views). Al (Grey), Pb (Black).

Energies calculated for the  $\Sigma 5 \{210\}$  and the  $\Sigma 5 \{310\}$  tilt grain boundaries in the Al and Al-Pb system are given in Table 5.1. Included are energies given by the DFT, MEAM and where available other EAM models and experiment. The agreement between all of the models and experiment for Al is reasonably good, with our MEAM and DFT energies agreeing with experiment within about  $0.10 \text{ J/m}^2$  and  $0.15 \text{ J/m}^2$ , respectively. For the systems containing Pb, the MEAM and DFT results qualitatively match one another. Both predict a

significant lowering of the grain boundary energies with respect to a single crystal solid solution and of the two grain boundaries modeled both yield a smaller value at a tilt angle of 53.1°. The calculations confirm the predictions given by the MEAM calculations.

Table 5.1 Calculated grain boundary energies in J/m<sup>2</sup>. The EAM energies are taken from ref. [21] and the experimental energies are from ref. [22].

Structure	Angle	DFT	MEAM	EAM	Experiment
<b>Pure Al</b>					
$\Sigma 5 \{210\}$	36.9°	0.46	0.55	0.49	0.60
$\Sigma 5 \{310\}$	53.1°	0.42	0.52	0.46	0.58
<b>Al-Pb systems (50 % of Coincident sites occupied by Pb atoms)</b>					
$\Sigma 5 \{210\}$	36.9°	0.099	0.128	-	-
$\Sigma 5 \{310\}$	53.1°	-0.004	0.096	-	-

## REFERENCES

1. J. W. Gibbs, The collected works of J.W. Gibbs – 1 (1928) 55-354, Longmans, Green and Co., New York.
2. J. Weissmüller, W. K. Krauss, T. Haubold, R. Birringer, H. Gleiter, Nanostruct. Mater. 1 (1992) 439.
3. J. Weissmüller, Nanostruct. Mater. 3 (1993) 261.

4. J. Weissmüller, *J. Mater. Res.*, 9 (1994) 4.
5. C. E. Krill, R. Klein, S. Janes, R. Birringer, *Mater. Sci. Forum*, 179-181 (1995) 443.
6. P. C. Millett, R. P. Selvam, S. Bansal, A. Saxena, *Acta Mater.*, 53 (2005) 3671.
7. R. Kirchheim, *Acta. Met.*, 50 (2002) 413.
8. B. Farber, E. Cadel, A. Menand, G. Schmitz, R. Kirchheim, *Acta Mater.*, 48 (2000) 789.
9. Phase diagrams for binary alloys, edited by Hiroaki Okamoto (2000), ISBN 0871706822.
10. T. Massalski. Binary alloy phase diagrams, (1990) Materials Park, OH: ASM International.
11. Metals handbook - 8th edition, 8 (1973) 263, American Society for metals, Metals Park, Ohio.
12. P. Hohenberg, W. Kohn, *Phys. Rev.*, 136, (1964) B864.
13. W. Kohn, L. J. Sham, *Phys. Rev.*, 140 (1965) 1133.
14. G. Kresse, J. Hafner, *Phys. Rev. B*, 47 (1993) 558.
15. G. Kresse, J. Furthmüller, *Comput. Mat. Sci.*, 6 (1996) 15.
16. G. Kresse, J. Furthmüller, *Phys. Rev. B*, 54 (1996) 11169.
17. D. Vanderbilt, *Phys. Rev. B*, 41 (1990) 7892.
18. G. Kresse, J. Hafner, *J. Phys: Condens. Matt.*, 6 (1994) 8245.
19. Y. Wang, J. P. Perdew, *Phys. Rev. B*, 43 (1991) 8911.
20. H. J. Monkhorst, J. D. Pack, *Phys. Rev. B*, 13 (1976) 5188.
21. D.E. Spearot, PhD Thesis, Georgia Tech, (2005) - Atomistic Calculations of Nanoscale Interface Behavior in Fcc Metals.
22. G. Hasson, J.-Y. Boos, I. Herbeuval, M. Biscondi, C. Goux, *Surf. Sci.*, 31 (1972) 115.

## CHAPTER 6

# PREDICTION OF A MINIMUM Pb CLUSTER SIZE BELOW WHICH Pb PREFERS TO SEGREGATE TO Al GRAIN BOUNDARIES COMPARED TO FORMING CLUSTERS IN BULK Al

### 6.1 INTRODUCTION

Most of the experimental work on the Al-Pb binary alloys has been carried out to investigate the equilibrium shapes and melting behavior of nanosized Pb particles embedded in an Al matrix [1-6]. Because of its extremely low mutual solubility [7], Pb tends to form clusters in Al-Pb alloys, and these clusters have been widely used as an ideal model system for studying the behavior of pure nanoscale particles embedded in crystalline matrix. Johnson et al. [8] used Transmission Electron Microscopy to investigate the morphology of nanosized lead inclusions in Al formed by ion implantation. Their images revealed a distribution of nanometer-scale Pb inclusions starting with a diameter of about 1 nm throughout the implanted layer of the matrix, and also clusters spanning grain boundaries.

The structures formed by substitutional Pb impurities in an Al bicrystal containing  $\Sigma 5 \{210\}$  grain boundaries are studied in Section 4.3. Monte Carlo simulations were carried out for systems containing five and one atomic percent Pb atoms. Both simulations showed segregation of Pb impurities to the grain boundaries. In addition, the five atomic percent

simulations showed formation of Pb clusters both in the bulk and across the grain boundaries as observed experimentally [8]. The snapshots (Section 4.3.2) from the one atomic percent simulation showed segregation of a majority of Pb atoms to the grain boundaries that are well dispersed along the interface with no significant clustering. These results suggest dispersion of Pb impurities along the grain boundaries prior to cluster formation. Using a simple thermodynamic model, in this chapter we have tried to predict a cross over cluster size below which Pb prefers to segregate to the grain boundaries compared to forming clusters in the bulk.

## 6.2 METHODOLOGY

High resolution transmission electron microscopy (HRTEM) observations have revealed that at equilibrium nanosized Pb inclusions embedded in Al matrix adopt a cuboctahedral shape [9-10]. A cubical simulation cell as shown in Fig. 6.1a embedded with a cuboctahedral shaped Pb inclusion was therefore used for simulating an Al matrix. The cuboctahedral structure was built with its center coinciding with the geometric center of the Al matrix and in the experimentally observed cube-on-cube orientation with the matrix. Periodic boundary conditions were applied in all three directions. In the structures all the lattice sites correspond to an Al face-centered cubic lattice. We simulated lead particles of ten different sizes: Pb<sub>314</sub>, Pb<sub>405</sub>, Pb<sub>586</sub>, Pb<sub>1072</sub>, Pb<sub>1289</sub>, Pb<sub>2406</sub>, Pb<sub>2556</sub>, Pb<sub>2951</sub>, Pb<sub>4249</sub>, Pb<sub>6266</sub> (corresponding to a size from 1.6 nm to 4.9 nm). The subscript identifies the number of Pb atoms in the particles. Structures with 586, 1289, 2406 and 6266 number of Pb atoms correspond to particles with a magic

number of atoms (i.e., nanoparticles containing complete shells of atoms) and correspond to sizes of 2.1, 2.8, 3.5, 4.9 nm, respectively. When viewed along the  $\langle 110 \rangle$  axes, cuboctahedrons appear with two pairs of opposite  $\{111\}$  facets and one pair of opposite  $\{100\}$  facets placed edge-on (Fig. 6.1b). This orientation is ideal for the observation of the size and shape of the Pb inclusion. The distance between opposite pairs of  $\{111\}$  facets, as shown by dotted line in the figure, was used for defining the cluster sizes.

Interatomic interactions in the Al-Pb system were described using the modified embedded atom method potential with parameters fit to the results of density functional calculations. Atomic positions in the built configurations were initially relaxed using a molecular dynamics energy minimization technique. To accommodate the large size of Pb compared to Al, the volume of the computational cell was adjusted at regular intervals in between atomic position relaxation steps. Finally the configurations were relaxed using a conjugate gradient minimization technique. All of the above equilibration procedures were carried out at 0K.

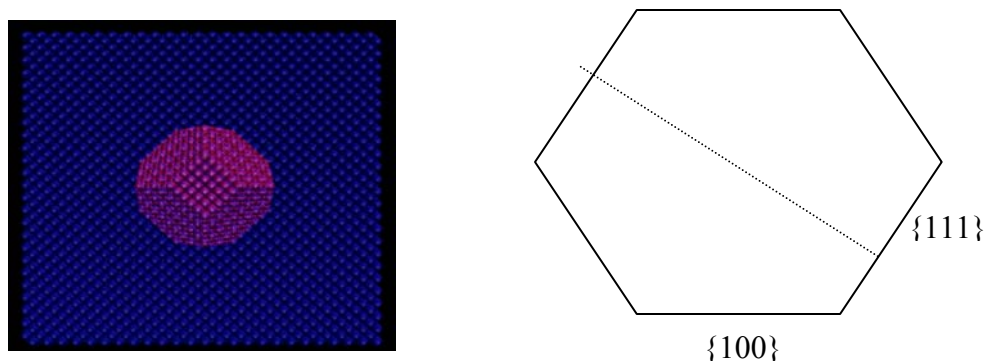


Fig. 6.1 (a) A simulation cell, showing a cuboctahedral shape Pb cluster (red) embedded in Al matrix (blue). (b) Schematic of cuboctahedral shape viewed along a  $\langle 110 \rangle$  direction.

To obtain a cross-over cluster size, the total energy of a grain boundary cell with an embedded Pb cluster (in a cuboctahedral configuration) in aluminum matrix was compared with the total energy of a grain boundary cell with Pb atoms substituted for Al at the grain boundary. A schematic of such a model is illustrated in Fig. 6.2, where the two systems are designated as system A and system B respectively.

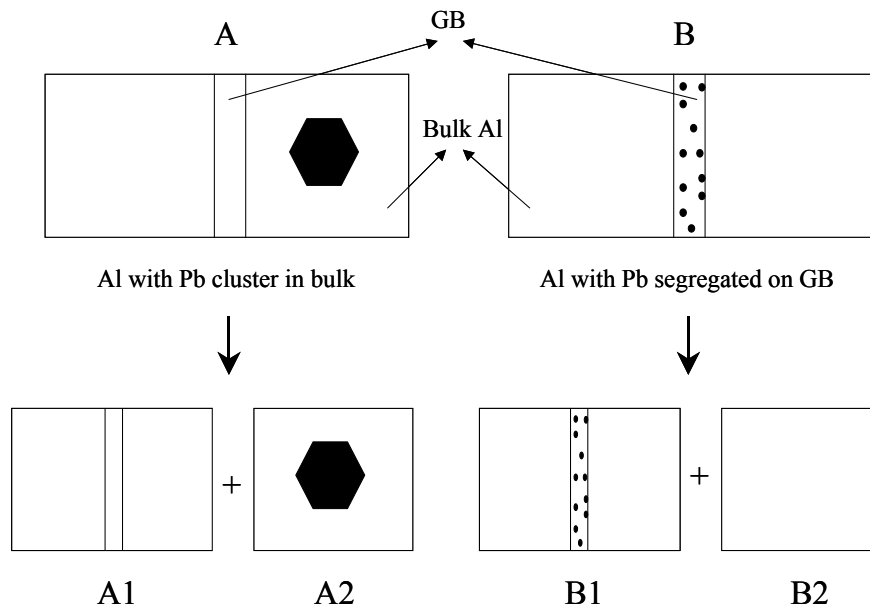


Fig. 6.2 Illustration of thermodynamic energy model.

The total energy difference between the two systems is then written as

$$\Delta E_{Tot} = E_a - E_b \quad (1)$$

where  $E_a$  and  $E_b$  are the total energies of the systems A and B, respectively. If system A has a higher energy than system B,  $\Delta E_{Tot}$  is greater than zero and Pb tends to stay in the grain boundary compared to forming a cluster in the Al matrix. The systems A and B were further subdivided into systems A1, A2 and B1, B2 respectively, which are shown in Fig. 6.2.

Equation (1) was further expressed as

$$\begin{aligned}\Delta E_{Tot} &= \left( E_{cluster(Pb)}^{Al} + E_{GB}^{Al} \right) - \left( E_{GB(Pb)}^{Al} + E_{bulk}^{Al} \right) \\ &= \left( E_{cluster(Pb)}^{Al} - E_{bulk}^{Al} \right) - \left( E_{GB(Pb)}^{Al} - E_{GB}^{Al} \right)\end{aligned}\quad (2)$$

The energies referred to in equation (2) are as follows:  $E_{cluster(Pb)}^{Al}$ , the total energy of a bulk Al cell embedded with a cuboctahedral shape Pb cluster (A2);  $E_{bulk}^{Al}$ , the total energy of the same bulk Al cell but with no embedded Pb atoms (B2);  $E_{GB(Pb)}^{Al}$ , the total energy of a grain boundary cell with lead atoms substituted for aluminum at the grain boundary (B1);  $E_{GB}^{Al}$ , is total energy of the same grain boundary cell with no Pb atoms at the grain boundary (A1). The total energy difference as given by equation (2) is therefore equivalent to the energy change in forming a Pb cluster in the bulk aluminum compared to Pb being segregated to the grain boundary.

When converted to energy per Pb atom, Eq. (2) becomes

$$\Delta E = \left( \frac{E_{cluster(nPb)}^{Al} - E_{bulk}^{Al}}{nPb} \right) - \left( \frac{E_{GB(mPb)}^{Al} - E_{GB}^{Al}}{mPb} \right) \quad (3)$$

where,  $nPb$  and  $mPb$  refer to the number of Pb atoms contained in a cuboctahedral shape Pb cluster and Pb atoms that were substituted for aluminum at the grain boundary.

Denoting  $(E_{cluster(nPb)}^{Al} - E_{bulk}^{Al})$  and  $\left( \frac{E_{GB(mPb)}^{Al} - E_{GB}^{Al}}{mPb} \right)$  by  $E_1$  and  $E_2$  respectively, the energy

difference per Pb atom,  $\Delta E$  from Eq. (3) can finally be written as

$$\Delta E = \left( \frac{E_1 - nPb \times E_2}{nPb} \right) \quad (4)$$

For calculating  $E_{GB(mPb)}^{Al}$ , a  $\Sigma 5 \{210\}$  Al tilt GB was chosen. A schematic of atomic sites at the  $\Sigma 5 \{210\}$  Al tilt GB is shown in Fig. 6.3. The viewing direction is along the  $\langle 100 \rangle$  crystallographic direction (X-axis) and atom positions are projected into the Y-Z plane for clarity. There are two atomic planes along the  $\langle 100 \rangle$  direction. The silver and black circles represent atoms distributed on the first and second  $\{100\}$  planes, respectively. Figs. 6.4a,

6.5a and 6.6a show three Pb doped reference structures that were used for calculating the energy term,  $E_{GB(mPb)}^{Al}$ . Figs. 6.4b, 6.5b and 6.6b show an enlarged view of the Pb doped grain boundary of the three respective reference structures, where Al and Pb atoms are shown in silver and black. All of the three reference structures contain 5120 total atoms.

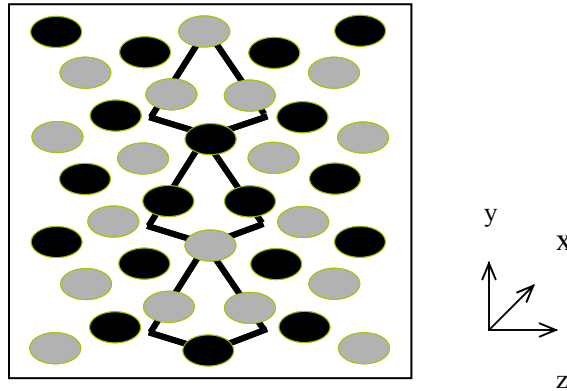


Fig. 6.3 Schematic of a  $\Sigma 5$   $\langle 100 \rangle$   $\{210\}$  undoped Al tilt boundary. The silver and black represent atoms on the  $\{100\}$  and  $\{200\}$  planes, respectively.

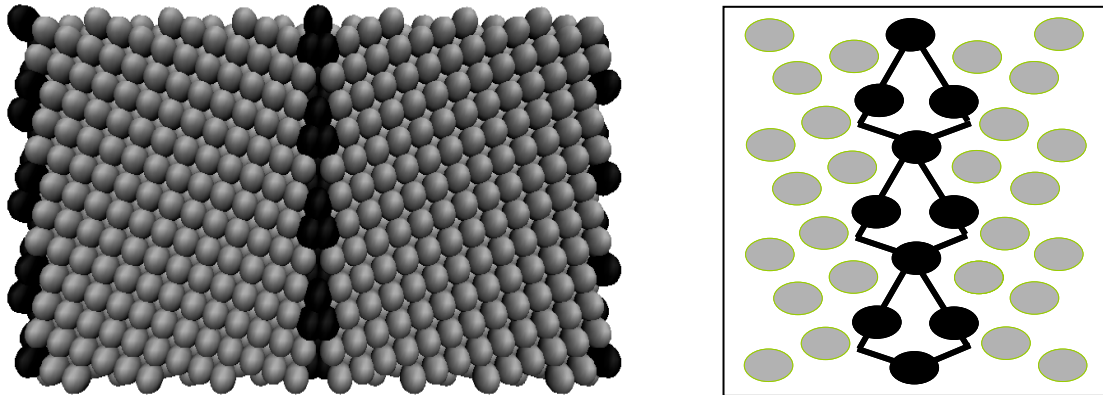


Fig. 6.4 (a) Bicrystalline reference configuration number 1, that contains two Pb doped  $\Sigma 5$   $\langle 100 \rangle$   $\{210\}$  Al tilt boundaries. (b) Schematic of reference configuration number 1. Al and Pb atoms are shown in silver and black respectively.

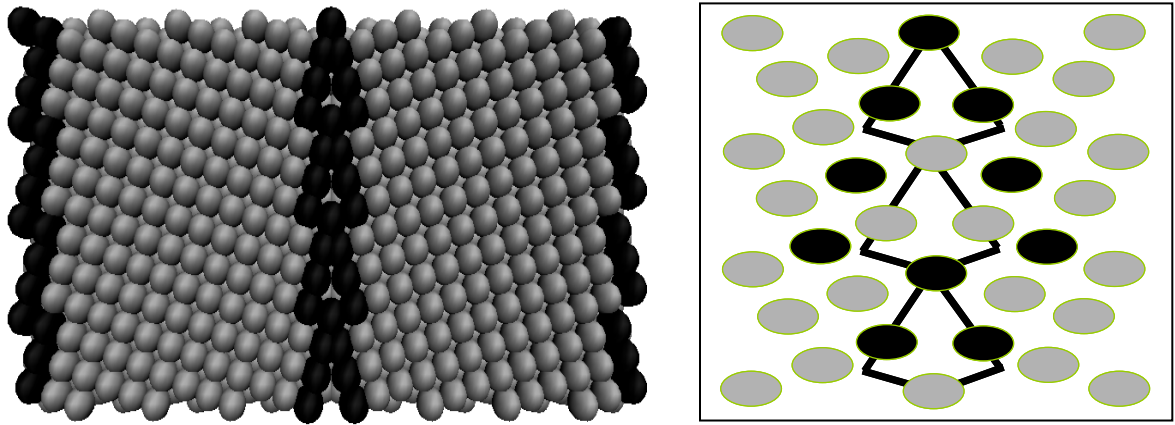


Fig. 6.5 (a) Bicrystalline reference configuration number 2, that contains two Pb doped  $\Sigma 5$   $\langle 100 \rangle$   $\{210\}$  Al tilt boundaries. (b) Schematic of reference configuration number 2. Al and Pb atoms are shown in silver and black respectively.

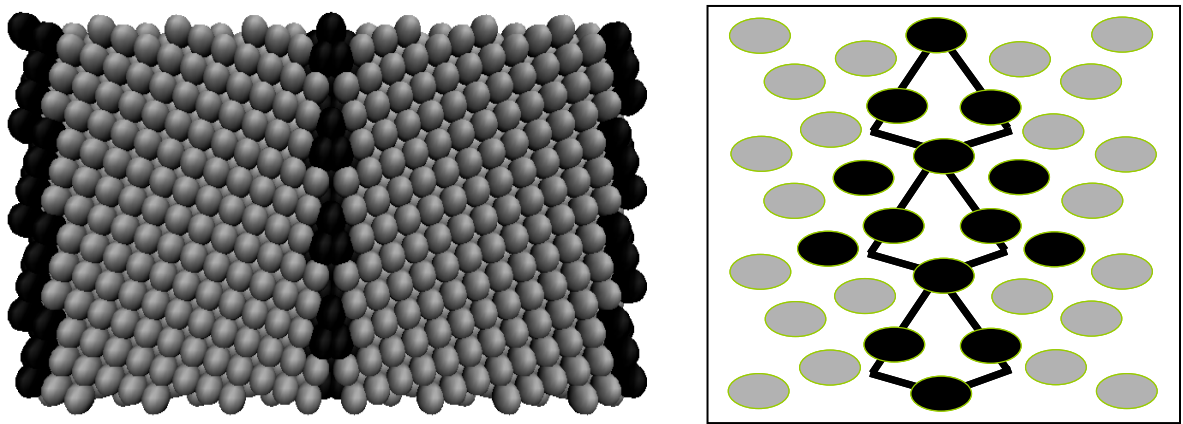


Fig. 6.6 (a) Bicrystalline reference configuration number 3, that contains two Pb doped  $\Sigma 5$   $\langle 100 \rangle$   $\{210\}$  Al tilt boundaries. (b) Schematic of reference configuration number 3. Al and Pb atoms are shown in silver and black respectively.

### 6.3 RESULTS AND DISCUSSION

The details regarding calculations of the energy terms  $E_1$ ,  $E_2$  and  $\Delta E$  are given in Tables 6.1, 6.2 and 6.3 respectively. A scatter plot showing the variation of  $E_2$  with  $mPb$  for the three reference structures is shown in Fig. 6.7. The energy increase per Pb atom  $E_2$  in placing  $mPb$  Pb atoms at the Al grain boundary for the three reference configurations is designated by a square, a triangle and a diamond symbol in the figure. The  $E_2$  for placing  $mPb$  Pb atoms at the Al grain boundary in the reference configuration 2 is larger than that for placing it in either configuration 1 or 3, both of which are more closely packed by Pb at the grain boundaries compared to that of reference configuration 2. The variation of  $E_1$ , the energy increase in placing a cuboctahedral shape Pb cluster in bulk Al, with  $nPb$  (number of Pb atoms in cuboctahedral) is shown in Fig. 6.8. The figure shows an increase in  $E_1$  values with an increase in the number of Pb atoms that constitute the cuboctahedral shaped Pb clusters.

Table 6.1 Details showing calculations of energy term  $E_2$  (In Eq. (4) above).

Reference structures	Total # of atoms	$mPb$	$E_{GB(mPb)}^{Al}$	$E_{GB}^{Al}$	$X = E_{GB(mPb)}^{Al} - E_{GB}^{Al}$	$E_2 = \left( \frac{X}{mPb} \right)$
Structure 1 (Fig 6.4)	5120	384	-16448.52	-17070.31	621.79	1.62
Structure 2 (Fig 6.5)	5120	448	-16200.03	-17070.31	870.28	1.94
Structure 3 (Fig 6.6)	5120	640	-16027.21	-17070.31	1043.10	1.63

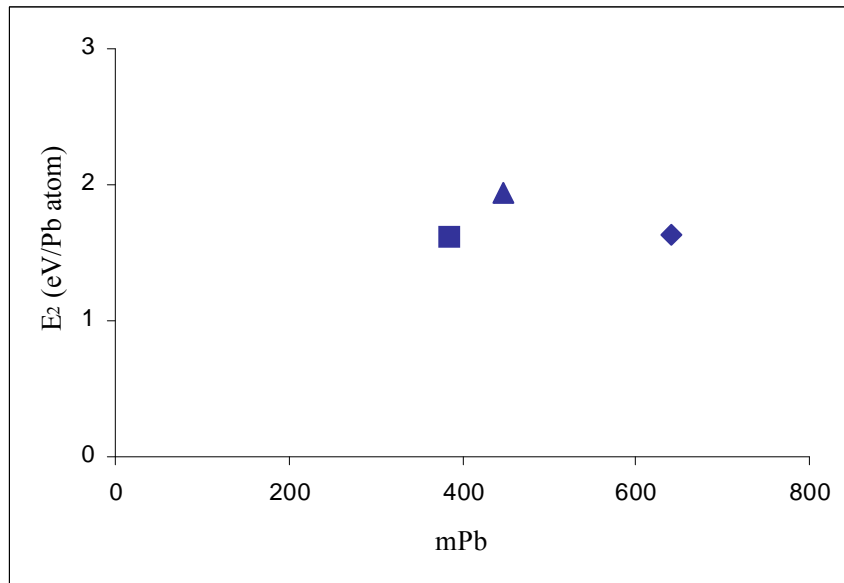


Fig. 6.7 Variation of  $E_2$  with  $mPb$  for the three reference structures.

Table 6.2 Details showing calculations of energy term  $E_1$  (In Eq. (4) above). MN refers to magic numbers of Pb atoms.

Total no of atoms	$nPb$	$E_{cluster(nPb)}^{Al}$	$E_{bulk}^{Al}$	$E_1 = E_{cluster(nPb)}^{Al} - E_{bulk}^{Al}$
40000	1	-133986.54	-133989.48	2.94
78732	314	-263023.49	-263730.31	706.82
40000	405	-133173.63	-133989.48	815.85
40000	586 (MN)	-132293.11	-133989.48	1696.37
78732	1072	-260155.77	-263730.31	3574.54
40000	1289 (MN)	-131608.67	-133989.48	2380.81
40000	2406 (MN)	-129941.15	-133989.48	4048.33
78732	2556	-259020.02	-263730.31	4710.29
40000	2951	-129185.32	-133989.48	4804.16
78732	4249	-256570.33	-263730.31	7159.98
78732	6266 (MN)	-253484.51	-263730.31	10245.80

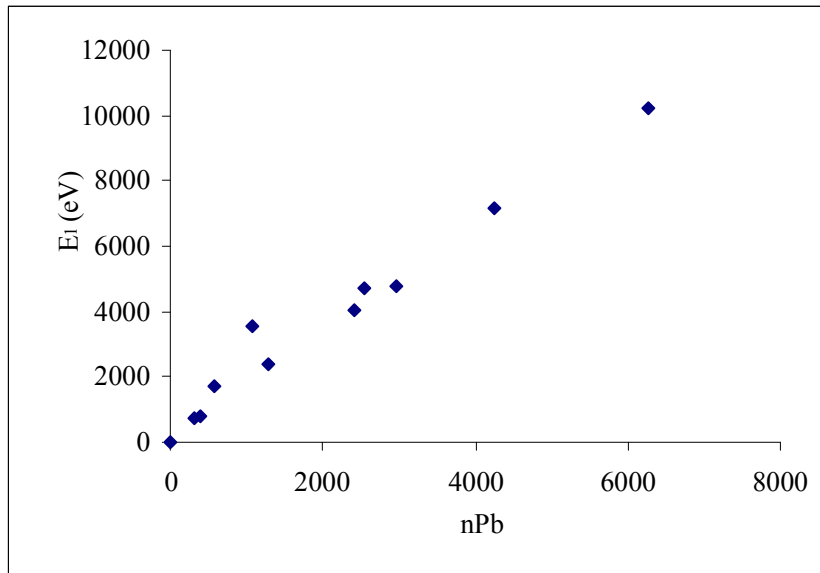


Fig. 6.8 Variation of  $E_1$  with  $nPb$  for cuboctahedral shape Pb clusters.

Table 6.3 Details showing calculations of energy term  $\Delta E$  (In Eq. (4) above). MN refers to magic numbers of Pb atoms.

No. of Pb atoms in cubooctahedral $nPb$	$E_1 = (E_{cluster(nPb)}^{Al} - E_{bulk}^{Al})$	$E_2 = \left( \frac{E_{GB(mPb)}^{Al} - E_{GB}^{Al}}{mPb} \right)$			$\Delta E = \left( \frac{E_1 - nPb \times E_2}{nPb} \right)$		
		Ref 1	Ref 2	Ref 3	Ref 1	Ref 2	Ref 3
1	2.942	1.62	1.94	1.63	1.327	1.004	1.315
314	706.829	1.62	1.94	1.63	0.636	0.313	0.624
405	815.852	1.62	1.94	1.63	0.399	0.076	0.387
586 (MN)	1696.371	1.62	1.94	1.63	1.279	0.957	1.268
1072	3574.547	1.62	1.94	1.63	1.719	1.396	1.707
1289 (MN)	2380.811	1.62	1.94	1.63	0.232	-0.091	0.220
2406 (MN)	4048.336	1.62	1.94	1.63	0.068	-0.255	0.055
2556	4710.299	1.62	1.94	1.63	0.228	-0.095	0.216
2951	4804.167	1.62	1.94	1.63	0.013	-0.310	0.001
4249	7159.981	1.62	1.94	1.63	0.070	-0.253	0.058
6266 (MN)	10245.804	1.62	1.94	1.63	0.020	-0.302	0.008

The difference in energy per Pb atom  $\Delta E$  vs.  $nPb$  with respect to the three reference structures is plotted in Figs. 6.9, 6.10 and 6.11, respectively. Fig. 6.9 shows that this Pb substitution (For reference structure number 1) is always preferred over the formation of Pb clusters (with size <6000). Very similar trend is also observed for grain boundary Pb substitution for reference structure number 3 (Fig. 6.11). However, Fig. 6.10 shows that clusters larger than a size of 2.8 nm are more stable in the bulk matrix. Therefore, reference structure number 2 is not preferred for Pb segregation. Figs. 6.9-6.11 indicate that there exist special configurations for lead atoms to occupy at the grain boundary. Pb atoms in the solid

solution would like to segregate to these special configurations at the grain boundary. Clusters can also be formed when those preferred grain boundary configurations are not accessible. In this case, there may exist a critical cluster size (smallest cluster) above which clusters can be found in the Al matrix.

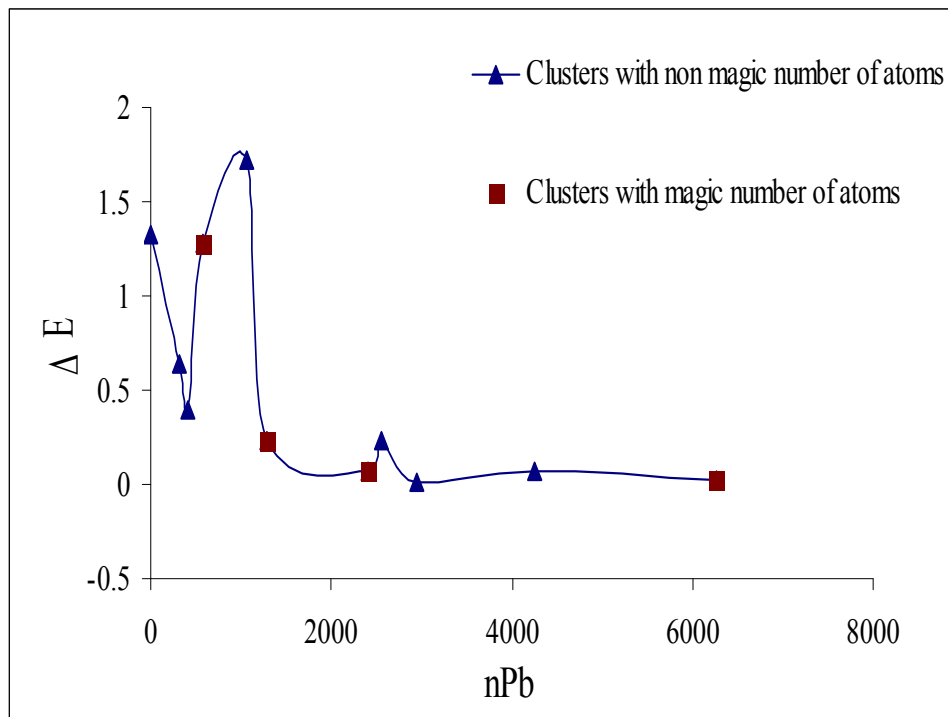


Fig. 6.9  $\Delta E$  (eV/Pb atom) vs.  $n_{Pb}$  with respect to reference structure number 1.

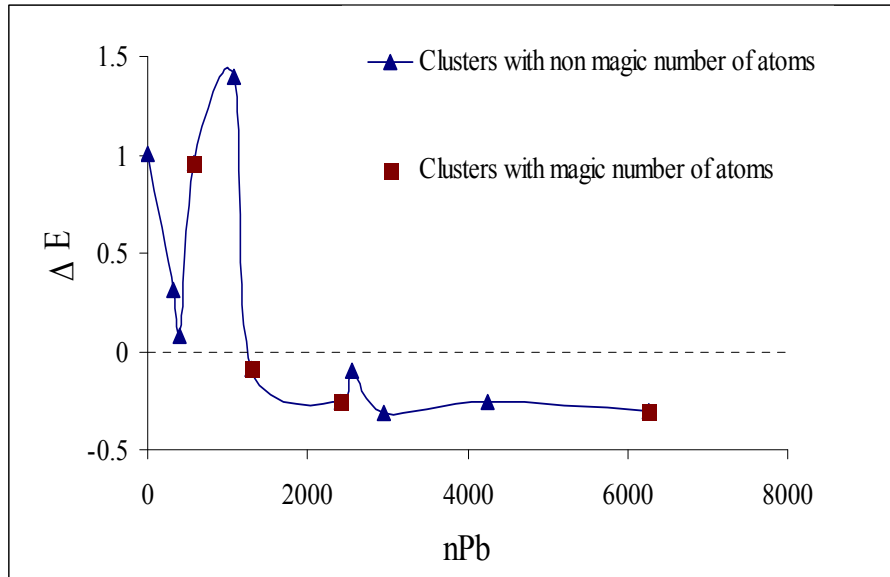


Fig. 6.10  $\Delta E$  (eV/Pb atom) vs.  $n_{Pb}$  with respect to reference structure number 2.

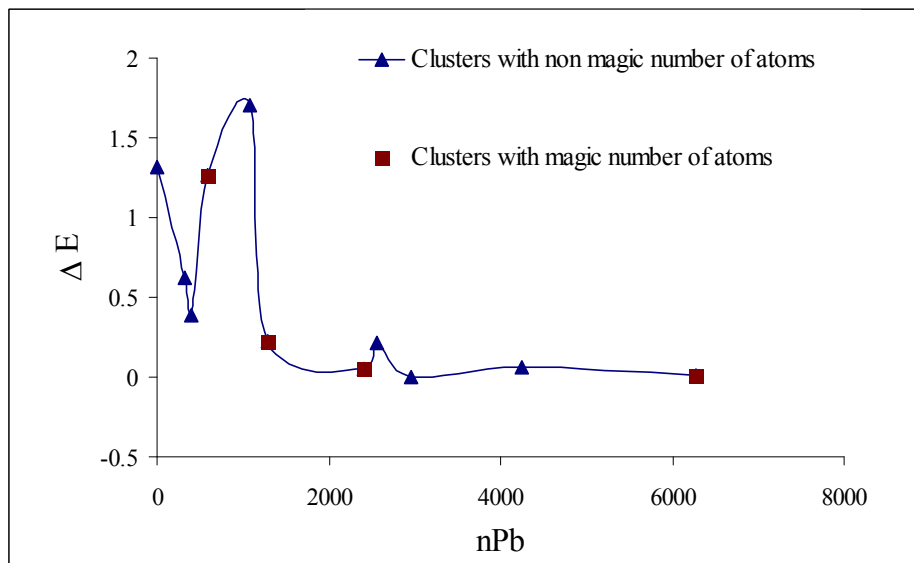


Fig. 6.11  $\Delta E$  (eV/Pb atom) vs.  $n_{Pb}$  with respect to reference structure number 3.

## REFERENCES

1. U. Dahmen, S. -Q. Xiao, S. Paciornik, E. Johnson, A. Johansen, *Phys. Rev. Lett.*, 78 (1997) 471.
2. E. Johnson, A. Johansen, U. Dahmen, S. Chen, T. Fujii, *Mater. Sci. Eng. A*, 304–306 (2001) 187.
3. R. Goswami, K. Chattopadhyay, *Acta Metall. Mater.*, 43 (1995) 2837.
4. K. I. Moore, K. Chattopadhyay, B. Cantor, *Proc. Roy. Soc. A*, 414 (1987) 499.
5. K. I. Moore, D. L. Zhang, B. Cantor, *Acta Metall. Mater.*, 38 (1990) 1327.
6. H. H. Andersen, E. Johnson, *Nucl. Instr. Meth. B*, 106 (1995) 480.
7. T. Massalski, *Binary alloy phase diagrams*, (1990) Materials Park, OH: ASM International.
8. E. Johnson, A. Johnson, S. Hinderberger, S. -Q. Xiao, U. Dahmen, *Interface Science*, 3 (1996) 279.
9. S. -Q. Xiao, E. Johnson, S. Hinderberger, A. Johansen, K. K. Bourdelle, U. Dahmen, *J. Microscopy*, 180 (1995) 61.
10. L. Grabaek, J. Bohr, H. H. Andersen, A. Johansen, E. Johnson, L. Sarholt-Kristansen, I.K. Robinson, *Phys. Rev. B.*, 45 (1992) 2628.

## CHAPTER 7

### PREDICTION OF ENERGIES OF $\langle 100 \rangle$ TILT GRAIN BOUNDARIES IN Al-Pb ALLOYS USING THE DISCLINATION STRUCTURAL UNITS MODEL

#### 7.1 INTRODUCTION

As discussed in Chapters 4 and 5, atomistic simulations were used to investigate the structures and energies of Pb impurities in an aluminum bicrystal containing two complementary  $\Sigma 5 \langle 100 \rangle \{210\}$  tilt grain boundaries. Interatomic interactions in the Al-Pb alloy system were described using a modified embedded atom method (MEAM) potential with parameters fit to the results of density functional theory (DFT) calculations on two hypothetical Al-Pb binary alloys. These simulations, and subsequent calculations of the energies of Pb clusters in an Al matrix with the same potential function, predict a preference for the segregation of Pb atoms to grain boundaries compared to the formation of embedded Pb clusters with diameters less than about 2.8 nm. This preference for grain boundary segregation is consistent with experimental z-contrast transmission electron micrographs of Al-Pb nanoalloys that indicate Pb dispersed on grain boundaries [1]. According to Weissmüller and others [2-7], the segregation of impurities with limited solubilities to grain boundaries can reduce the grain boundary energy and therefore help to stabilize the nanostructures against grain growth. A reduction of grain boundary energy with an increase in the number of Pb atoms on the grain boundary was predicted by our calculations, with a negative

energy with respect to a dilute solid solution predicted when more than 50 percent of the coincident sites are replaced by Pb atoms. This result suggests that Pb impurities can stabilize grains in Al against grain growth. The DFT energies also confirmed the stabilization of grain boundaries in Al due to Pb segregation with respect to the dilute solid solution as predicted by the MEAM. To further explore the boundary stabilization caused by segregated Pb atoms over the entire tilt angle, we report in this chapter the results of the application of a multiscale disclination structural units model (DSUM) [8-11] for calculating energies of Al tilt grain boundaries over a complete range of misorientation angles with and without Pb atoms at the grain boundaries.

To date, several models have been proposed to describe the structures and energies of grain boundaries at arbitrary angles. Using atomistic simulations Sutton and Vitek [12-14] showed that grain boundaries in FCC metals may be viewed as a linear combination of ‘structural units.’ Similarly, a disclination description of grain boundaries was developed by Shih and Li in the 1970s [15-16]. More recently a disclination-structural unit model (DSUM) that combines the structural units model with the disclination based description of grain boundaries for predicting energies of intermediate boundaries has been developed [8-11].

The approach used for calculating energies of Al tilt grain boundaries over a complete range of misorientation angle has combined energies for a few key structures (delimiting or preferred boundaries) that were calculated using the MEAM, with the disclination structural units model. The reliability of the DSUM was evaluated by calculating energies of a number

of intermediate grain boundaries atomistically, using both the MEAM and a Glue-type interatomic potential, and comparing these to predictions from the DSUM. The DSUM predicted a strong dependence of the grain stabilization energy on tilt angle.

## 7.2 METHODOLOGY

The central idea behind the DSUM [8-11] is to construct properties of arbitrary grain boundaries from a few related key structures called preferred or delimiting grain boundaries [12]. The structural units model describes an arbitrary tilt interface as consisting of a combination of structural units, taken in certain proportion and sequence from high-symmetry (low  $\Sigma$ ) grain boundaries at special angles, that bound the angle of interest of the grain boundary [10]. For example, in Fig. 7.1, an Al  $\langle 100 \rangle$  symmetrical tilt boundary with a misorientation angle  $\theta$ , is shown to be modeled as consisting of a linear combination of structural units B and C from two preferred boundaries with misorientation angles  $\theta_1$  and  $\theta_2$ , respectively. The angles  $\theta_1$  and  $\theta_2$  delimit the angle of interest  $\theta$  of the grain boundary presented. The junctions where different types of structural units meet are represented as partial disclinations of strength  $\pm w = (\theta_1 - \theta_2)$ , and an intermediate (or arbitrary) grain boundary can therefore be represented in the form of a wall of disclination dipoles (DDWs) with the following expression for the grain boundary energy [10]

$$E_{\text{Tot}} = \frac{m d_1 e_1 + n d_2 e_2}{h} + E_{\text{elastic}} + \alpha \frac{G a_o^2 w^2 n}{2 \pi^3 (1 - \nu) h} \quad (1)$$

$$E_{\text{elastic}} = \frac{Gw^2h}{32\pi^3(1-\nu)} \left( n f(\lambda n) + \sum_{i=1}^{n-1} \sum_{j=i+1}^n [f(\tilde{y}_j - \tilde{y}_i + \lambda) - 2f(\tilde{y}_j - \tilde{y}_i) + f(\tilde{y}_j - \tilde{y}_i - \lambda)] \right) \quad (2)$$

The first term in Eq. (1) is a weighted sum of the energy of the individual structural units, and the second and third term represents the elastic energy of the DDW and the energy of the disclination cores, respectively. The quantities  $d_1$  and  $d_2$  are the arm lengths, and  $m$  and  $n$  are the numbers of the first and second types of structural units that constitute one period  $h = (md_1 + nd_2)$  of the intermediate boundary. The quantities  $a_0$ ,  $G$ , and  $\nu$  are the lattice parameter, shear modulus and Poisson's ratio of bulk Al, respectively, and  $\alpha$  is a parameter that sets the disclination core energy contribution over a range of intermediate angles. The quantities  $\tilde{y}_i = \pi y_i / h$  and  $\lambda = \pi d_2 / h$  where  $y_i$  are the coordinates of disclination dipoles, and the function  $f(t)$  is given by [16]

$$f(t) = -16 \int_0^t (t - \nu) \ln[2 \times \sin(\nu)] d\nu \quad (3)$$

For the delimiting grain boundaries, the disclination strength  $w=0$ , and therefore the energy of these structures can be used to determine values for the  $e_n$ 's in Eq. (1). The quantity  $\alpha$  is taken as one for all the calculations presented here.

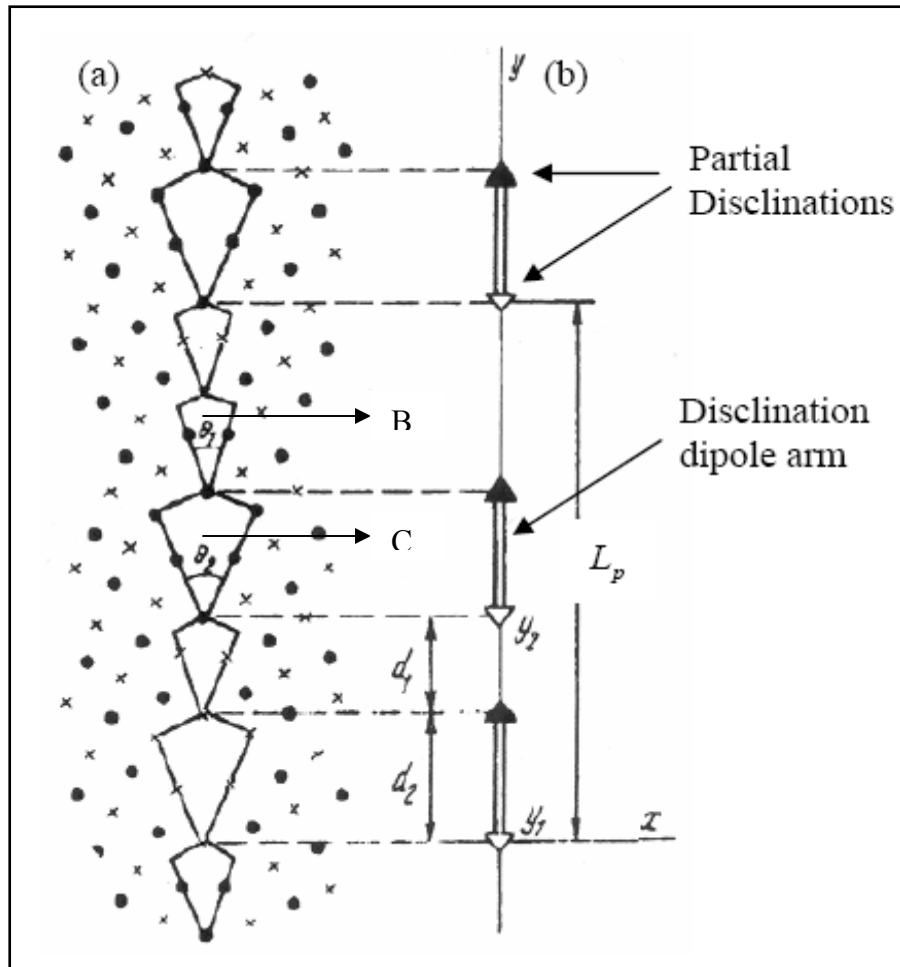


Fig. 7.1 Disclination structural unit model representation of a grain boundary consisting of B and C structural units [9].

According to the DSUM model the dependence of the energy of tilt boundaries on misorientation angle can be determined if the geometric parameters and energies of all preferred boundaries with a given tilt axis are known. For the  $\langle 100 \rangle$  misorientation axis,

Wang *et al.* [17] found that the  $\Sigma 1 \{110\}$  (perfect lattice),  $\Sigma 5 \{210\}$ ,  $\Sigma 5 \{310\}$  and the  $\Sigma 1 \{100\}$  (perfect lattice) are the preferred interfaces. The structural units associated with each of these boundaries are denoted by symbols A, B, C and D, respectively. The angles of  $0^\circ$ ,  $36.9^\circ$ ,  $53.1^\circ$  and  $90^\circ$  misorientations that correspond to these structures were taken as the preferred boundaries, and these angles therefore delimit the intermediate angles. Geometric parameters of the preferred boundaries and the values used for the elastic constant are given in Table 7.1.

Table 7.1 Geometric parameters of the preferred boundaries and the elastic constants used in the calculations.

$\Sigma$ (Plane)	Angle (deg)	Period vector	Elastic Constants	
1 {110}	0	$\frac{1}{2}[1,-1,0]$	Shear	Poisson's
5 {210}	36.87	$\frac{1}{2}[1,-2,0]$	Modulus (G)	ratio ( $\nu$ )
5 {310}	53.13	$\frac{1}{2}[1,-3,0]$		
1 {100}	90	$\frac{1}{2}[010]$	2.65x10 <sup>4</sup>	0.347
			Mpa	

The energies for the delimiting grain boundaries in the Al and Al-Pb systems were calculated using both the MEAM and the glue interatomic potential. To create the alloy the Al atoms at one half of the coincident sites along the plane of atoms at the grain boundaries were

replaced with Pb atoms. Prior modeling using the MEAM suggests that these are the most stable substitutional sites. The grain boundary energy for the Pb doped system was taken as the difference between the total potential energy of the system with grain boundaries containing the Pb atoms and the potential energy of an ideal bulk solid solution containing the same number of Al and Pb atoms, divided by the total area of the two grain boundaries. In a similar way, the grain boundary energy for pure Al was calculated by taking the difference between the total energy of a structure containing two grain boundaries and an equivalent structure for bulk Al, divided by the total area of the two grain boundaries.

The energies calculated for the undoped and the Pb doped delimiting structures were then substituted into the DSUM model (Eqn's. 1 and 2). The grain boundary energies for the undoped and the Pb doped  $\langle 100 \rangle$  Al tilt boundaries over the complete range of misorientation angles were thus determined. The predictions given by the MEAM+DSUM and the GLUE+DSUM models are plotted in Figs. 7.2 and 7.3 of Section 7.3.

For the verification of the above results energies for a number of chosen intermediate grain boundaries (as mentioned in Table 7.2) were calculated atomistically using the MEAM and the Glue interatomic potentials. The chosen intermediate boundaries along with the preferred boundaries are listed in Table 7.2, where the misorientation axis, the misorientation angle, the SUM notation and the boundary planes for the respective grain boundaries are listed. The vertical 'bars' in the SUM notation denote one period of the interface structure and the 'dot'

signifies that the structural unit has shifted from the {100} lattice plane to the neighboring {200} plane. Sutton and Vitek [12-14] define this type of structure as being ‘centered’.

Table 7.2 List of intermediate interfaces studied for <100> tilt Al boundaries [17].

Axis	Angle	SUM Notation	Sigma	GB Plane
<100>	0	A	1	{110}
<100>	12.68	AAAB.AAAB	41	{540}
<100>	16.26	AAB.AAB	25	{430}
<100>	22.62	AB.AB	13	{320}
<100>	30.51	ABBB.ABBB	65	{740}
<100>	36.87	B.B	5	{210}
<100>	42.08	BBBC.BBBC	97	{940}
<100>	46.40	BC.BC	29	{520}
<100>	48.89	BCC.BCC	73	{830}
<100>	53.13	C	5	{310}
<100>	58.11	CCD.CCD	53	{720}
<100>	61.93	CD.CD	17	{410}
<100>	90	D	1	{100}

### 7.3 RESULTS AND DISCUSSION

The grain boundary energies, with and without substitutional Pb impurities, over a complete range of misorientation angles as predicted by the MEAM+DSUM are plotted in Fig. 7.2. By MEAM+DSUM we mean that the energies from the MEAM calculations for a few key structures (delimiting grain boundaries) that are shown by squares in Fig. 7.2, were input into the disclination structural-units model (Eqn’s 1 and 2), for calculating the energies of the

intermediate boundaries in the entire misorientation range. The energies for the intermediate boundaries are represented by triangles for pure Al and stars for Al-Pb system in Fig. 7.2. From the figure a satisfactory agreement of the energies of pure Al with experimental data [18] is evident. The energies for the Pb doped grain boundaries as calculated using the full atomistic MEAM model are indicated by circles in Fig. 7.2. The agreement between the atomistic calculations using the MEAM potential and the multiscale DSUM is excellent, where the maximum energy difference between the two methods is less than  $0.08 \text{ J/m}^2$ .

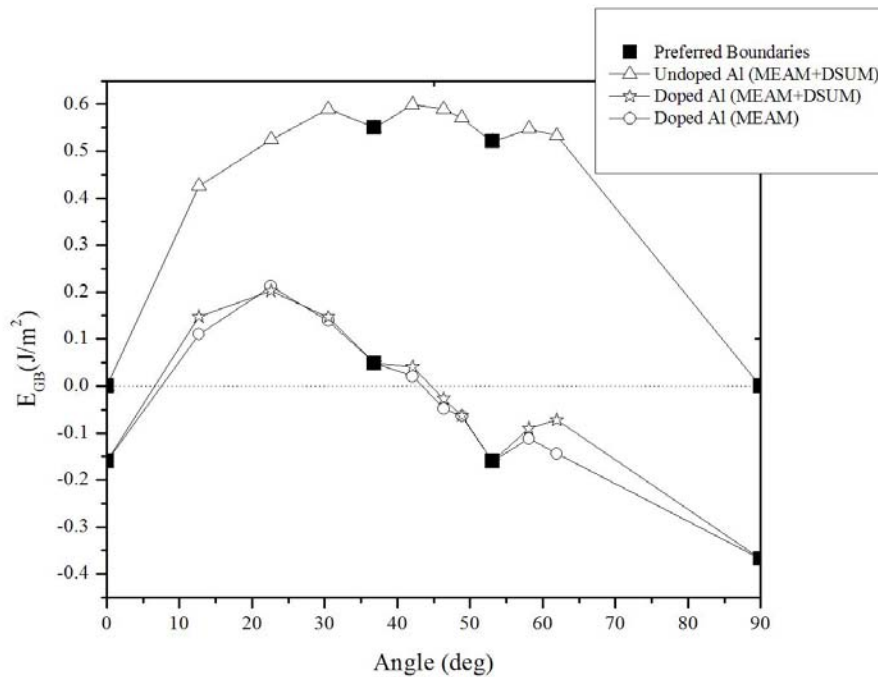


Fig. 7.2 Dependence of grain boundary energy on angle for  $\langle 100 \rangle$  symmetrical tilt-grain boundaries in Pb doped Al as calculated using atomistic MEAM and multiscale MEAM+DSUM model.

For the Pb doped grain boundaries, similar calculations as those using the MEAM were also made using the GLUE potential. The grain boundary energies as predicted by the GLUE+DSUM model and also by full atomistic calculations using the GLUE potential are shown in Fig. 7.3. Again, the agreement between the atomistic calculations using the GLUE potential (circles) and the multiscale GLUE+DSUM (stars) is excellent, where the maximum energy difference between the two methods is less than  $0.06 \text{ J/m}^2$ . These results are encouraging, especially considering that the DSUM has not previously been applied to alloys. In particular, the Al atoms in sites within the pure system where substitution by Pb is favored are under hydrostatic tension. Because the Pb atoms are larger than the Al atoms, substitution by Pb at these sites reduces the stress along the grain boundary, e.g. the segregation of Pb to the Al grain boundaries is driven by stress relief. The elastic term Eq. (2) contains only information about the elastic properties of the surrounding Al lattice, and it does not take into account the reduction in the stress dipoles along the grain boundary from the incorporation of Pb. However, for the delimiting grain boundaries  $w$  is zero, and therefore the stress reduction is incorporated into the weighted energy of the individual structural units. Our results suggest that this is sufficient to capture the intermediate grain boundary energies for the alloy.

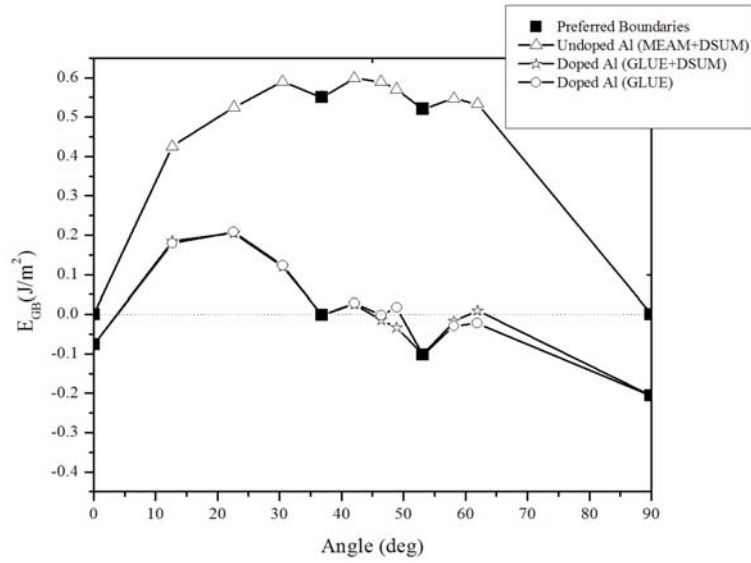


Fig. 7.3 Dependence of grain boundary energy on angle for <100> symmetrical tilt-grain boundaries in Pb doped Al as calculated using atomistic GLUE and multiscale GLUE+DSUM model.

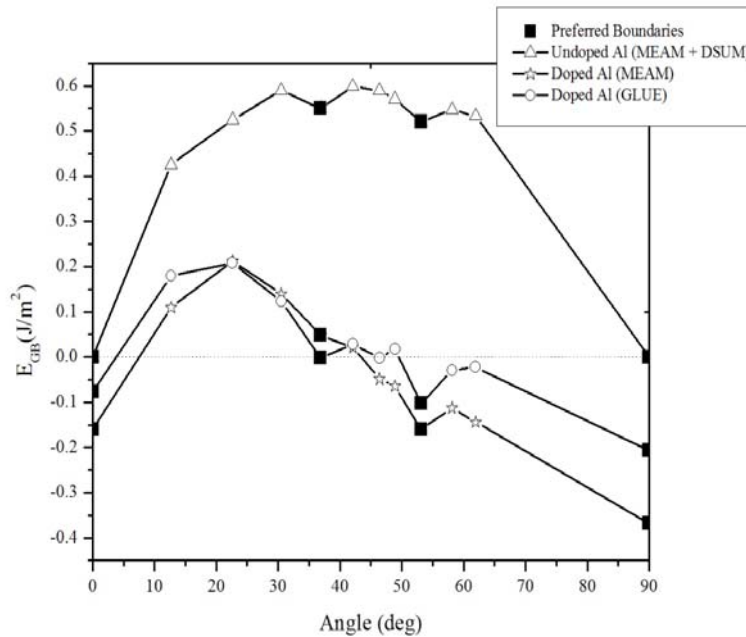


Fig. 7.4 Dependence of grain boundary energy on angle for <100> symmetrical tilt-grain boundaries in Pb doped Al as calculated using atomistic MEAM and GLUE potentials.

Fig. 7.4 shows a comparison of the grain boundary energies for the Pb doped Al as calculated atomistically using the MEAM and the GLUE interatomic potentials. The energies match one another within about  $0.16 \text{ J/m}^2$ . The plot indicates that the stabilization energy is strongly dependent on the tilt angle. The predictions given by the MEAM+DSUM and the GLUE+DSUM for the intermediate grain boundary at  $22.6^\circ$ , containing Pb, along with matching the full atomistic MEAM and GLUE results also match the DFT results reasonably well (see Table 7.3). The DFT calculations for this intermediate grain boundary were carried out using the same procedure as given for the  $\Sigma 5 \{210\}$  and the  $\Sigma 5 \{310\}$  tilt grain boundaries in Section 5.4. A uniform K-point mesh of  $8 \times 4 \times 1$  and a plane wave cut-off of 300 eV were used for the calculation.

For the systems containing Pb, all of the above models suggest a significant lowering of the grain boundary energies when compared to the grain boundary energies for pure Al. The results also suggest that a multiscale approach using DSUM can yield grain boundary stabilization as a function of tilt angle.

Table 7.3 Calculated energies ( $\text{J/m}^2$ ) for an intermediate grain boundary in the Al and Al-Pb system. The experimental energies are from ref. [18].

Structure	Angle	MEAM	MEAM+DSUM	DFT	DFT+DSUM	GLUE	GLUE+DSUM	Experiment
Pure Al								
$\Sigma 13 \{320\}$	$22.6^\circ$	0.48	0.52	-	0.47	-	-	0.54
Al-Pb systems								
$\Sigma 13 \{320\}$	$22.6^\circ$	0.212	0.203	0.220	-	0.208	0.2051	-

## REFERENCES

1. K. V. Rajulapati, R. O. Scattergood, K. L. Murty, G. Duscher and C. C. Koch, *Scripta Mater.*, 55 (2006) 155
2. J. Weissmüller, *Nanostruct. Mater.*, 3 (1993) 261.
3. J. Weissmüller, W. K. Krauss, T. Haubold, R. Birringer, H. Gleiter, *Nanostruct. Mater.*, 1 (1992) 439.
4. J. Weissmüller, *J. Mater. Res.*, 9 (1994) 4.
5. R. Kirchheim, *Acta Met.*, 50 (2002) 413.
6. F. Liu, R. Kirchheim, *J. Crystal Growth*, 264 (2004) 385.
7. F. Liu, R. Kirchheim, *Scripta. Mater.*, 51 (2004) 521.
8. V. Y. Gertsman, A. A. Nazarov, A. E. Romanov, R. Z. Valiev, V. I. Vladimirov, *Philo. Mag. A*, 59 (1989) 1113.
9. R. Z. Valiyev, V. I. Vladimirov, V. Y. Gertsman, A. A. Nazarov, A.Y. Romanov, *Physics of Metals and Metallography*, 69 (1990) 30.
10. A. A. Nazarov, O. A. Shenderova, D. W. Brenner, *Mater. Sci. Eng. A*, 281 (2000) 148.
11. D. V. Bachurin, R. T. Murzaev, A. A. Nazarov, *Fizika Metallov i Metallovedenie*, 96 (2003) 11.
12. A. P. Sutton, V. Vitek, *Philosophical Transactions of the Royal Society of London A*, 309 (1983a) 1.
13. A. P. Sutton, V. Vitek, *Philosophical Transactions of the Royal Society of London A*, 309 (1983b) 37.

14. A. P. Sutton, V. Vitek, *Philosophical Transactions of the Royal Society of London A*, 309 (1983c) 55.
15. J.C.M. Li, *Surf. Sci.*, 31 (1972) 12.
16. K.K. Shih, J.C.M. Li, *Surf. Sci.*, 50 (1975) 109.
17. G. J. Wang, A. P. Sutton, V. Vitek, *Acta Metallurgica*, 32 (1984) 1093.
18. G. Hasson, J.-Y. Boos, I. Herbeuval, M. Biscondi, C. Goux, *Surf. Sci.*, 31 (1972) 115.

## CHAPTER 8

### SUMMARY AND SUGGESTIONS FOR THE FUTURE WORK

#### 8.1 SUMMARY

Most of the experimental work on the Al-Pb binary alloy system has been carried out to investigate the equilibrium shapes and melting behavior of nanosized Pb clusters embedded in an Al matrix [1-7]. In this dissertation in addition to the cluster formation, the energetic and segregation of Pb impurities towards Al grain boundaries and its influence on thermal stability and mechanical behavior, using Monte Carlo, molecular dynamics and first principles methods have been investigated. Also reported is the application of a multiscale disclination structural unit model (DSUM) [8-11] for calculating energies of Al tilt boundaries over a complete range of misorientation angles, with and without Pb substitution on the grain boundaries.

The analytic calculations and Monte Carlo simulations were used to characterize the energy of substitutional Pb defects and its segregation and cluster formation in bulk Al, and in an Al bicrystal and a three-dimensional Al nanocrystallite. The simulations, which used a modified-embedded atom method potential fit to first principles results, predict clustering of Pb within an ideal bulk Al lattice, in agreement with prior experiments [2,7]. In the case of the bicrystal and nanocrystalline structure, the simulations predict segregation of Pb

impurities towards Al grain boundaries prior to cluster formation depending on the Pb content and the number of grain boundaries. In addition, for the nanocrystalline structure the Pb impurities also segregate toward triple junctions. Analysis of the local stress shows that the Pb atoms tend to initially segregate to lattice sites along the grain boundary (in the bicrystalline structure containing  $\Sigma 5$  {210} grain boundary) that would otherwise be under hydrostatic tension, consistent with a larger effective size of Pb atoms compared to Al. After these sites are filled, the simulations predict the formation of individual Pb clusters across the grain boundaries. Hence the simulations support the conclusions of Rajulapati *et al.* and other reported images of Pb clusters on the grain boundaries.

These simulations, and subsequent calculations of the energies of a cuboctahedral shaped Pb cluster embedded in an Al matrix with the same potential function, predict a preference for the segregation of Pb atoms to grain boundaries compared to its forming clusters in bulk Al, with diameters less than about 2.8 nm. Results also indicate that there exists special configurations for lead atoms to occupy at the grain boundaries and Pb atoms in the solid solution first tend to segregate to these special configurations. Pb clusters are formed when those preferred grain boundary configurations become inaccessible. In that case, there may exist a critical cluster size (smallest cluster) above which Pb clusters can be found in the Al matrix.

Al-Pb is an immiscible alloy and therefore a potential candidate for segregation induced thermal stabilization. The calculated relative enthalpies for various substitutional Pb defects

suggest that Pb impurities can help stabilize Al structures against grain growth. The relative enthalpy associated with one Pb atom in an Al lattice is positive, which is consistent with the immiscibility of Pb in Al. The relative enthalpy values for several percentages of the grain boundary sites with most stable segregation energies as filled with Pb suggests that although the enthalpies are all positive with respect to the ideal bulk Al and Pb, the grain boundary has a lower relative enthalpy than that for isolated Pb atoms, e.g. the ideal solid solution. Hence while the grain boundaries are not globally stable, they are metastable with respect to the thermodynamic limit of an infinitely dilute solid solution.

The segregation of impurities with limited solubility to grain boundaries has been shown to reduce the specific grain boundary energy to zero or negative values [12-14]. In an immiscible alloy like Al-Pb a state of metastability (i.e. a specific grain boundary energy of zero) with a certain solute concentration on the grain boundary could be achieved. Our Monte Carlo simulations predict that Pb atoms segregate to grain boundaries in a bicrystalline structure. The grain boundary energy as a function of Pb content was investigated for two high symmetry  $\Sigma 5 \{210\}$  and  $\Sigma 5 \{310\}$  Al tilt boundaries. To create alloys the Al atoms at 12.5, 25, 50, 75 and 100 percentage of the coincident sites along the plane of atoms at the two grain boundaries were replaced with Pb atoms. The calculations, using the MEAM potential, predict a reduction of grain boundary energy with an increase in the number of Pb atoms on the grain boundary. A negative energy with respect to the ideal solution was predicted when more than 50 and 40 percent of the coincident sites are replaced by Pb atoms for the  $\Sigma 5 \{210\}$  and  $\Sigma 5 \{310\}$  grain boundaries respectively. The creation of a

metastable state at predicted solute concentrations may help to stabilize Al structures against grain growth. The calculated DFT energies for the two grain boundaries also confirmed the stabilization of grain boundaries in Al due to Pb segregation with respect to an ideal solid solution as predicted by the MEAM.

To further explore the boundary stabilization caused by segregated Pb atoms over the entire tilt angle, a dependence of the energies of <100> symmetrical Al tilt boundaries, with and without Pb substitution, on misorientation angles using a multiscale disclination-structural unit model (DSUM) has been investigated. The disclination-structural unit model (DSUM) combines a structural unit model [15-17] with a disclination [18-19] based description of grain boundaries. For calculating the grain-boundary energies over the entire misorientation range, our method combined energies from the atomistic MEAM/GLUE calculations for a few key structures (delimiting grain boundaries) with the disclination structural-units model. The method combining MEAM with DSUM and GLUE with DSUM has been called the MEAM+DSUM and the GLUE+DSUM method respectively. The reliability of the DSUM was evaluated by calculating energies of a number of intermediate grain boundaries atomistically, using both the MEAM and the GLUE interatomic potential, and comparing these to predictions from the DSUM.

The agreement between grain boundary energy calculations using multiscale DSUM (i.e. MEAM+DSUM and GLUE+DSUM) models and the atomistic calculations (using MEAM and GLUE potentials) is reasonably good, with our MEAM+DSUM results agreeing with

atomistic MEAM calculation and GLUE+DSUM results agreeing with atomistic GLUE calculation within about  $0.08 \text{ J/m}^2$  and  $0.06 \text{ J/m}^2$  respectively. The predictions given by the MEAM+DSUM and the GLUE+DSUM for the intermediate grain boundary at  $22.6^\circ$ , containing Pb, along with matching the full atomistic MEAM and GLUE result also matches the DFT result reasonably well. The DSUM predicts a strong dependence of the grain stabilization energy on tilt angle for Al-Pb alloys.

Based on several experimental studies [20-21] the effects of Pb on the mechanical behavior of nanocrystalline Al are uncertain. In one case hardening was observed [20], while in the other there was a dramatic softening effect [21]. The reasons for these differences are not understood, but appear to be related to Pb segregation to grain boundaries, as observed by latter investigators using Z-contrast high resolution transmission electron microscopy (HRTEM).

To better understand the effect of Pb on the mechanical behavior of Al, particularly its strength, we used molecular dynamics simulations (in tension) to study the deformation of grain boundaries in bicrystalline aluminum and aluminum-lead alloys. Our preliminary results support the findings of Rajulpati *et al.* [21] that Pb segregation to Al grain boundaries causes a drop in hardness. Our modeling showed an increase in the overall thickness and disorder at the grain boundaries with Pb addition. We believe that this contributes to the softening observed experimentally. To better understand the underlying atomic mechanisms

causing the softening, an extensive follow-up work is needed to fully understand the evolution of the interface structures during the deformation process.

## **8.2 SUGGESTIONS FOR THE FUTURE WORK**

(1) Other metal-metal alloys such as Cu-Pb and Al-Bi with a miscibility gap can be studied to look for segregation patterns and segregation induced thermal stability.

(2) Its evident from our simulation results above that by changing system thermodynamics a metastable state by Pb segregation can be created, which possesses potential to thermally stabilize Al nanostructures against grain growth. In order to characterize temperature dependent grain growth behavior and mechanisms, the result motivates future work to focus on simulating Pb segregated Al nanostructures to different temperature regimes. MD simulations by Haslam *et al.* [22] revealed that in nanocrystalline materials (Pd) in addition to the conventional mechanism of grain growth by curvature-driven GB-migration, grain rotations play an equally important role. By eliminating the GB between neighboring grains, such rotations lead to grain coalescence and the consequent formation of highly elongated grains. So it will be instructive to investigate the mechanisms and the impediment to grain growth caused by the Pb during annealing of Al nanosamples at higher temperatures.

(3) This work is the first to apply multiscale disclination structural unit model (DSUM) to alloys. We investigated a dependence of the energies of [100] symmetric Al tilt boundaries,

with and without Pb substitution, on misorientation angles using DSUM. To further establish the validity of this model for alloys future work can focus on calculating grain boundary energy vs. misorientation curves for more complex tilt and twist boundaries.

(4) To study the effects of Pb on the mechanical behavior of Al, molecular dynamics simulations in uniaxial tension were used to deform an Al bicrystal containing two  $\Sigma 5 \{210\}$  tilt boundaries, with and without Pb substitution on the grain boundaries. The preliminary results from the simulations supporting the findings of Rajulpati *et al.* [21] are presented in Section 4.5.3. In order to better understand the underlying atomic mechanisms that cause softening of Al due to Pb segregation, an extensive follow-up work is needed to fully understand the evolution of the interface structures during the deformation process. Moreover, the microstructures in reality are more complex where the effect of grain orientation and grain size become important. The future work can also focus on studying Pb induced deformation in 3-d nanocrystalline Al structures where the effect of grain orientation and grain size on deformation can be easily studied.

## REFERENCES

1. U. Dahmen, S. -Q. Xiao, S. Paciornik, E. Johnson, A. Johansen, *Phys. Rev. Lett.*, 78 (1997) 471.
2. E. Johnson, A. Johansen, U. Dahmen, S. Chen, T. Fujii, *Mater. Sci. Eng. A*, 304–306 (2001) 187.

3. R. Goswami, K. Chattopadhyay, *Acta Metall. Mater.*, 43 (1995) 2837.
4. K. I. Moore, K. Chattopadhyay, B. Cantor, *Proc. Roy. Soc. A*, 414 (1987) 499.
5. K. I. Moore, D. L. Zhang, B. Cantor, *Acta Metall. Mater.*, 38 (1990) 1327.
6. H. H. Andersen, E. Johnson, *Nucl. Instr. Meth. B*, 106 (1995) 480.
7. E. Johnson, A. Johnson, S. Hinderberger, S. -Q. Xiao, U. Dahmen, *Interface Science*, 3 (1996) 279.
8. V. Y. Gertsman, A. A. Nazarov, A. E. Romanov, R. Z. Valiev, V. I. Vladimirov, *Philo. Mag. A*, 59 (1989) 1113.
9. R. Z. Valiyev, V. I. Vladimirov, V.Y. Gertsman, A. A. Nazarov, A. Y. Romanov, *Physics of Metals and Metallography*, 69 (1990) 30.
10. A. A. Nazarov, O. A. Shenderova, D. W. Brenner, *Mater. Sci. Eng. A*, 281 (2000) 148.
11. D. V. Bachurin, R. T. Murzaev, A. A. Nazarov, *Fizika Metallov i Metallovedenie*, 96 (2003) 11.
12. J. Weissmüller, *Nanostruct. Mater.*, 3 (1993) 261.
13. J. Weissmüller, W. K. Krauss, T. Haubold, R. Birringer, H. Gleiter, *Nanostruct. Mater.*, 1 (1992) 439.
14. J. Weissmüller, *J. Mater. Res.*, 9 (1994) 4.
15. A. P. Sutton, V. Vitek, *Philosophical Transactions of the Royal Society of London A*, 309 (1983a) 1.
16. A. P. Sutton, V. Vitek, *Philosophical Transactions of the Royal Society of London A*, 309 (1983b) 37.

17. A. P. Sutton, V. Vitek, *Philosophical Transactions of the Royal Society of London A*, 309 (1983c) 55.
18. J. C. M. Li, *Surf. Sci.*, 31 (1972) 12.
19. K. K. Shih, J. C. M. Li, *Surf. Sci.*, 50 (1975) 109.
20. H. W. Sheng, F. Zhou, Z. Q. Hu, K. Lu, *J. Mater. Res.*, 13 (1998) 308.
21. K. Rajulapati, R. O. Scattergood, K. L. Murty, G. Duscher, C. C. Koch, *Scripta Mater.*, 55 (2006) 155.
22. A. J. Haslam, S. R. Phillpot, D. Wolf, D. Moldovan, H. Gleiter, *Mater. Sci. Eng. A*, 318 (2001) 293.